School of Electrical and Computer Engineering
Chalmers University of Technology
Göteborg, Sweden

Technical Report No. 265

# Thermal modelling of small cage induction motors

by

**Gunnar Kylander**

Submitted to the School of Electrical and Computer Engineering
Chalmers University of Technology
in partial fulfilment of the requirements
for the degree of
Doctor of Philosophy

Department of Electrical Machines and Power Electronics

February 1995

ISBN 91-7197-061-4
(Tryckeri)
Göteborg, 1995

# Abstract

The loadability of electric machines is above all determined by temperature limits. In this work, thermal network models, suitable for totally enclosed fan-cooled (TEFC) induction motors, are used to predict the machine temperatures.

Two specific models are suggested: one with 107 nodes, which primarily is intended as a design tool, and one with 7 nodes, for increased simplicity. The steady-state solution method is valid in a broad speed-range and for variable load. Time-dependent solutions are obtained as a function of four input variables: frequency, stator voltage, torque, and ambient temperature.

The thermal resistance calculation is emphasized in the work. For the purpose of identifying unknown thermal resistances, some identification techniques are suggested, that use measured steady-state temperatures as boundary conditions. Empirical formulas are suggested for heat transfer coefficients of various parts of the machine. The stator windings are modelled using a rectangular geometry with a surrounding equivalent air pocket. A discussion about the optimum number of nodes in a thermal network and a sensitivity analysis are included in the study. Experimental investigations are performed on a 4 kW and a 15 kW induction motor. The resistive losses are calculated using the equivalent circuit of the induction machine. The stator core losses are calculated by a two-dimensional, time-stepping finite element method. Friction and windage losses as well as additional losses are measured. Comparisons between measured and calculated temperatures show that good agreement can be expected if the heat transfer coefficient between the frame and the ambient and the additional losses are known.

**Keywords**:

thermal network, thermal model, induction motor, TEFC, losses, identification

# Preface

The work involved in this study was carried out at the Department of Electrical Machines and Power Electronics, Chalmers University of Technology, as a part of the wind energy project.

I would like to express my deep gratitude to Professor Jorma Luomi for the interest he has shown for this work and for important discussions and advice. I also wish to thank Associate Professor Jonny Hylander for his encouragement and support. Colleagues and staff-members who have helped me during the work should not be forgotten.

The financial support granted by NUTEK, the Swedish National Board for Industrial and Technical Development, is gratefully acknowledged.

# CONTENTS

LIST OF SYMBOLS 7

1 INTRODUCTION 11

2 MEASUREMENTS 13
- 2.1 Test motors 13
- 2.2 Measurement of electrical and mechanical quantities 15
- 2.3 Temperature measurements 16
- 2.4 Measurement errors 19

3 LOSS MODELLING 20
- 3.1 Losses in induction machines 20
  - 3.1.1 Resistive losses 21
  - 3.1.2 Fundamental core losses 22
  - 3.1.3 Friction and windage losses 23
  - 3.1.4 No-load stray losses and additional losses 24
- 3.2 Current and slip calculation 26
  - 3.2.1 Equivalent circuit 26
  - 3.2.2 Equivalent circuit for harmonics 30
- 3.3 Losses of the test motors 32
- 3.4 Treatment of core losses and additional losses 36

4 THERMAL NETWORKS 39
- 4.1 Heat transfer basics 39
- 4.2 Thermal network theory 42
- 4.3 Node configurations 44
- 4.4 A thermal model for TEFC induction motors 46
- 4.5 Identification of thermal resistances 48

5 MODELS OF THE MACHINE PARTS 49
- 5.1 Rotor 49
  - 5.1.1 Internal modelling 49
  - 5.1.2 Thermal resistance of the air gap 50
  - 5.1.3 Heat transfer from the end rings 53
- 5.2 Shaft 58
- 5.3 Stator winding 59

5.3.1 Coil sides 59
5.3.2 End windings 65
5.4 Stator core 69
5.5 Frame 71
5.5.1 Thermal resistance in the axial direction 71
5.5.2 Heat transfer to the ambient 71
5.5.3 Thermal contact resistance between the frame and the stator yoke 77
5.6 End shields 79
5.7 Bearings 82

6 STEADY-STATE RESULTS 84
6.1 Optimum size of thermal networks 84
6.2 Sensitivity analysis 86
6.3 Comparison of calculated and measured data 87
6.3.1 4 kW motor 87
6.3.2 15 kW motor 89
6.4 A small thermal model with simple implementation 92

7 TIME-DEPENDENT PROBLEMS 96
7.1 Thermal capacity 98
7.2 Numerical integration methods 99
7.3 Simulations 100
7.4 Wind energy applications 103

8 CONCLUSIONS 104

REFERENCES 107

APPENDICES 111
Appendix A Data of the test motors 111
Appendix B Material data 113

# List of symbols

| | |
|---|---|
| $A$ | area [m$^2$] |
| $A_\mathrm{b}$ | cross-sectional area of a rotor bar [m$^2$] |
| $A_\mathrm{Cu}$ | copper area in a stator slot [m$^2$] |
| $A_\mathrm{f}$ | cross-sectional area of the fins [m$^2$] |
| $A_\mathrm{r}$ | cross-sectional area of a rotor end ring [m$^2$] |
| $B_\mathrm{max}$ | maximum value of the flux density [T] |
| $b$ | thickness or width [m] |
| $C$, $C_\mathrm{th}$ | thermal capacity [J/K] |
| $c$ | heat capacitivity [J/kg·K] |
| $d$ | diameter or thickness [m] |
| $d_\mathrm{a}$ | air pocket thickness [m] |
| $d_\mathrm{b}$ | average bearing diameter [m] |
| $d_\mathrm{h}$ | hydraulic diameter [m] |
| $d_\mathrm{i}$ | slot insulation thickness [m] |
| $F_\mathrm{g}$ | geometry factor |
| $f$ | frequency [Hz] |
| $Gr$ | Grashof number |
| $g$ | acceleration of gravity [m/s$^2$] |
| $h$ | height [m], time-step [s] |
| $I_0$ | no load current [A] |
| $I_\mathrm{s}$ | stator current [A] |
| $I_\mathrm{sa}$ | active component of the stator current [A] |
| $I_\mathrm{r}$ | rotor current [A] |
| $k_\mathrm{Ft}$ | eddy current loss factor |
| $k_\mathrm{Hy}$ | hysteresis loss factor |
| $k_\mathrm{L}$ | skin effect factor for the inductance |
| $k_\mathrm{R}$ | skin effect factor for the resistance |
| $L, \ell$ | length [m] |
| $L_\mathrm{m}$ | magnetizing inductance [H] |
| $\ell_\mathrm{av}$ | average conductor length of half a turn [m] |
| $\ell_\mathrm{b}$ | length of a rotor bar [m] |
| $\ell_\mathrm{c}$ | stator core length [m] |
| $\ell_\mathrm{ov}$ | average conductor length of the winding overhangs [m] |
| $\ell_\mathrm{r}$ | length of a rotor end ring segment [m] |
| $m$ | mass [kg] |
| $Nu$, $Nu_d$ | Nusselt number |

| | |
|---|---|
| $P$ | power [W] |
| $P_{\mathrm{bar}}$ | losses in the rotor bars [W] |
| $P_{\mathrm{Cus}}$ | resistive losses in the stator winding [W] |
| $P_{\mathrm{Cur}}$ | resistive losses in the rotor winding [W] |
| $P_{\mathrm{d}}$ | nodal losses [W] |
| $P_{\mathrm{Fes}}$ | stator core losses due to the main flux [W] |
| $P_{\mathrm{f}}$ | losses due to friction and windage [W] |
| $P_{\mathrm{ring}}$ | losses in the rotor end rings [W] |
| $P_{\mathrm{sk}}$ | losses due to the skew leakage flux [W] |
| $P_{\mathrm{st}}$ | combined additional and no-load stray losses [W] |
| $P_{\mathrm{str}}$ | combined additional and no-load stray losses in the rotor [W] |
| $P_{\mathrm{t}}$ | losses in the stator teeth [W] |
| $P_{\mathrm{tot}}$ | total machine losses [W] |
| $P_{\mathrm{y}}$ | losses in the stator yoke [W] |
| $P_0$ | total flux-dependent losses at no load [W] |
| $Pr$ | Prandtl number |
| $p$ | number of pole pairs |
| $Q$ | loss density [W/m$^3$] |
| $Q_{\mathrm{r}}$ | rotor slot number |
| $Q_{\mathrm{s}}$ | stator slot number |
| $q$ | heat flux [W/m$^2$] |
| $R$, $R_{\mathrm{th}}$ | thermal resistance [K/W] |
| $Re$, $Re_d$ | Reynolds number |
| $R_{\mathrm{m}}$ | iron loss resistance [Ω] |
| $R_{\mathrm{s}}$ | stator resistance [Ω] |
| $R_{\mathrm{r}}$ | rotor resistance [Ω] |
| $r$ | radius [m] |
| $r_\delta$ | average radius of the air gap [m] |
| $s$ | slip |
| $T$ | temperature [°C], torque [Nm] |
| $(Ta)_{\mathrm{m}}$ | modified Taylor number |
| $T_{\mathrm{av}}$ | average temperature [°C] |
| $T_{\mathrm{max}}$ | maximum temperature [°C] |
| $T_{\mathrm{w}}$ | surface temperature [°C], [K] |
| $T_{\mathrm{s}}$ | shaft torque [Nm] |
| $T_\infty$ | reference temperature [°C], [K], free stream temperature [°C] |
| $\Delta T$ | temperature drop over the air gap [K] |
| $t$ | time [s] |

| | |
|---|---|
| $U_\mathrm{m}$ | voltage corresponding to air-gap flux [V] |
| $U_\mathrm{s}$ | phase voltage [V] |
| $u$ | air velocity [m/s] |
| $u_\mathrm{f}$ | fan peripheral speed [m/s] |
| $u_\mathrm{r}$ | rotor peripheral speed [m/s] |
| $X_\mathrm{m}$ | magnetizing reactance [Ω] |
| $X_{\mathrm{s}\lambda}$ | leakage reactance of the stator [Ω] |
| $X_{\mathrm{r}\lambda}$ | leakage reactance of the rotor [Ω] |
| $x$, $y$, $z$ | space coordinates [m] |

| | |
|---|---|
| $\mathbf{C}$ | thermal capacitance matrix |
| $\mathbf{G}$ | thermal conductance matrix |
| $\mathbf{P}$ | loss vector |
| $\mathbf{T}$ | temperature vector |
| $\mathbf{\Theta}$ | temperature rise vector |

| | |
|---|---|
| $\alpha$ | heat transfer coefficient [W/m$^2$K] |
| $\alpha_\mathrm{de}$ | heat transfer coefficient of the drive side end shield [W/m$^2$K] |
| $\alpha_\mathrm{fe}$ | heat transfer coefficient of the fan side end shield [W/m$^2$K] |
| $\beta$ | volume coefficient of expansion [1/K] |
| $\mathit{\Delta}$ | sheet thickness [m] |
| $\delta$ | air gap, taking thermal expansion into account [m] |
| $\delta_\mathrm{e}$ | equivalent air gap, taking Carter factors into account [m] |
| $\delta_\mathrm{R}$ | skin depth [m] |
| $\delta_0$ | air gap without thermal expansion [m] |
| $\varepsilon$ | emissivity |
| $\theta$ | temperature rise [K] |
| $\theta_\mathrm{f}$ | temperature rise of the frame [K] |
| $\kappa_\mathrm{Fe}$ | thermal expansion coefficient of iron [1/K] |
| $\lambda$ | thermal conductivity [W/m·K] |
| $\lambda_\mathrm{a}$ | thermal conductivity of air [W/m·K] |
| $\lambda_\mathrm{f}$ | thermal conductivity of a fluid [W/m·K] |
| $\lambda_\mathrm{i}$ | thermal conductivity of the slot insulation [W/m·K] |
| $\lambda_\mathrm{imp}$ | thermal conductivity of the slot impregnation [W/m·K] |
| $\lambda_\mathrm{s}$ | thermal conductivity of the slot material [W/m·K] |
| $\lambda_x$, $\lambda_y$, $\lambda_z$ | thermal conductivity in different spatial directions [W/m·K] |
| $\mu$ | dynamic viscosity [kg/m·s] |
| $\mu_0$ | permeability of free space [Vs/Am] |

| | |
|---|---|
| $\nu$ | kinematic viscosity [$m^2/s$] |
| $\rho$ | density [$kg/m^3$] |
| $\rho_e$ | resistivity [Ωm] |
| $\sigma$ | Stefan-Boltzmann's constant [$W/m^2K^4$], relative skew |
| $\omega$ | angular speed [rad/s] |
| $\xi$ | height to skin depth ratio |

# 1 Introduction

The main limiting factor for how much an electric machine can continuously be loaded, is usually the temperature. Exceeding the thermal limits results in various undesired phenomena: The oxidation process in insulation materials is accelerated, which eventually leads to loss of dielectrical property. Bearing lubricants may deteriorate or the viscosity may become too high, resulting in reduced oil film thickness. Other problems are mechanical stresses and changes in geometry caused by thermal expansion of the machine elements.

Because of these problems, the temperatures in electric machines must be kept below certain limits. In order to predict the machine temperatures, thermal models are employed, that can be used to improve the machine design or to determine the loadability during different operating conditions. If the thermal model is used in the design process, it must properly represent the effects of design modifications, thus allowing a systematic procedure of optimization. This means in general that a fairly complex model is necessary. If the thermal model is used for determining the loadability of an existing machine, a simpler model can be used. The most important difficulties lie in the loss calculation, the determination of the heat transfer from the frame to the ambient, and in the modelling of the stator windings and the bearings. An example of a possible application of the thermal model is in the control of wind turbine generators. If the generator is operated at the thermal limit rather than at the rated power limit, it can convert more wind energy to electrical energy and thus generate more profit. A thermal model can also be used to determine allowable short-time overloads.

The most frequently used thermal models are lumped parameter models [1,2] and numerical methods like the finite element method [3,4]. A lumped parameter model, often referred to as a thermal network model, gives the average and, for some assumptions, maximum temperatures of the elements within the machine. Its advantages lie in its simple mathematical form and easy implementation. By the finite element method, heat conduction problems can be solved more accurately than by a thermal network. The finite element method is particularly well suited for solving transient or steady-state problems with large temperature gradients within individual machine parts, e.g. high-inertia starts, unbalanced operation or thermal asymmetries caused by ventilation failure in large machines. A drawback of the finite element method is that three-dimensional and time-dependent problems are demanding both in software development and hardware requirements. For normal operation of small machines the finite element method is less suited, because the temperature gradients within distinct machine parts are small, which makes the lumped-parameter approach more natural.

The present work deals with lumped parameter models. The goal is to design a suitable thermal model that can be used as a tool for constructing cage induction motors and to describe all related problems and aspects of implementation. In particular the following problems are to be investigated:

- method and level of discretization of the machine
- identification of unknown thermal resistances

Many earlier publications [1,2,5,6,7,8] propose a relatively small number of elements in the thermal model. However, in this work, the machine is discretized by a significantly larger number of elements, which gives more information about the axial temperature distribution in the machine. Much of the earlier work [2,6,7,8] also suffers from the lack of a detailed study of the thermal resistances, which makes it difficult to apply the suggested models on arbitrary machines. The present work focuses more on the analysis of the thermal resistances and gives fairly straightforward rules for their calculation. The work concentrates on totally enclosed fan-cooled (TEFC) induction motors and much of the findings is based on experimental results from a 4 kW and a 15 kW induction motor.

# 2 Measurements

## 2.1 Test motors

The test machines are standard cage induction motors. The first machine is an ABB MBT180L with a rated power, current and speed of 15 kW, 32 A and 970 rpm, respectively. The second machine is an ABB MBT112M with a rated power, current and speed of 4 kW, 9 A and 1435 rpm, respectively. The rated voltage is 380 V and the rated frequency 50 Hz for both machines. The cross-section of the slot geometries is shown in Figs 1–2. The machines are shown in Figs 3–4. Geometrical data and winding data of the machines are given in Appendix A together with the parameters of the equivalent circuit.

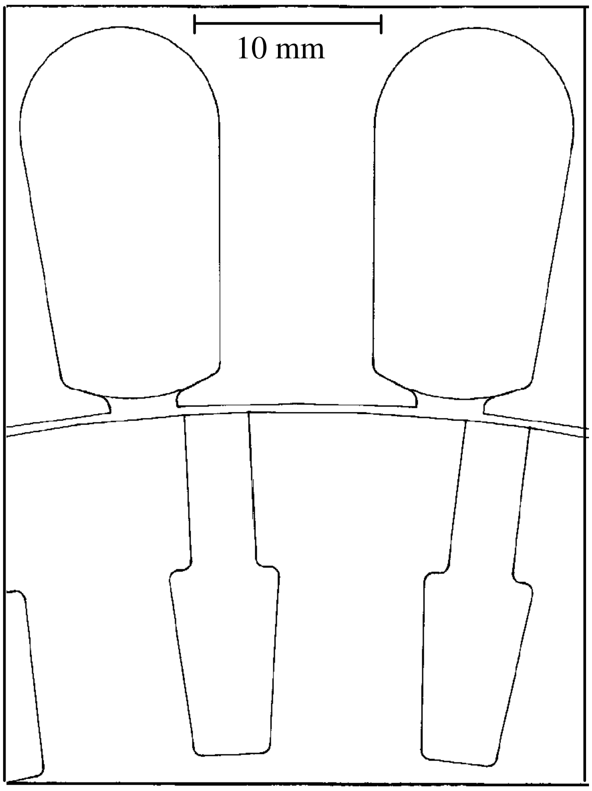

*Figure 1. Slot geometry of the 15 kW machine.*

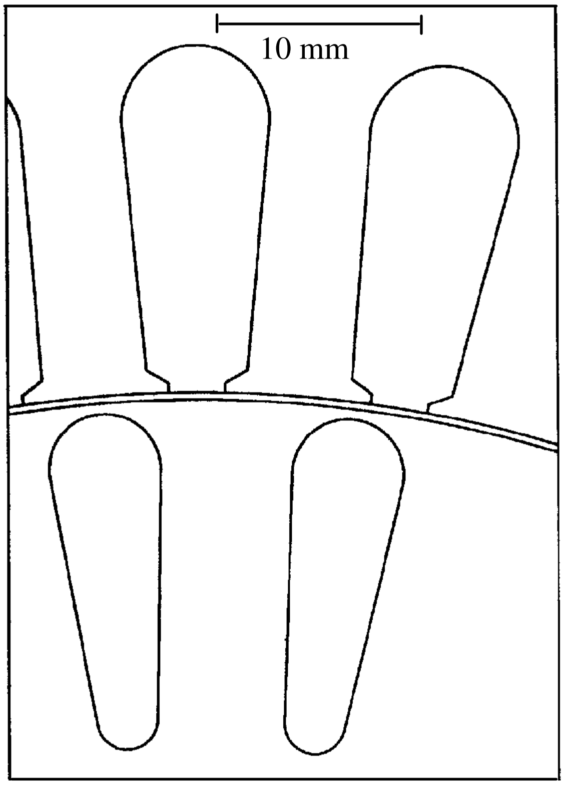

*Figure 2. Slot geometry of the 4 kW machine.*

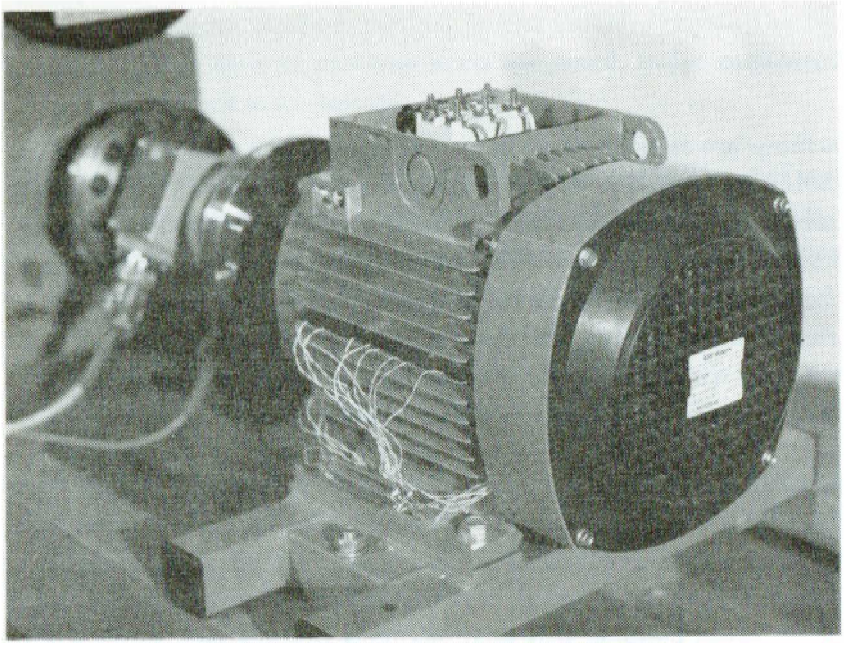

*Figure 3. The 4 kW test motor.*

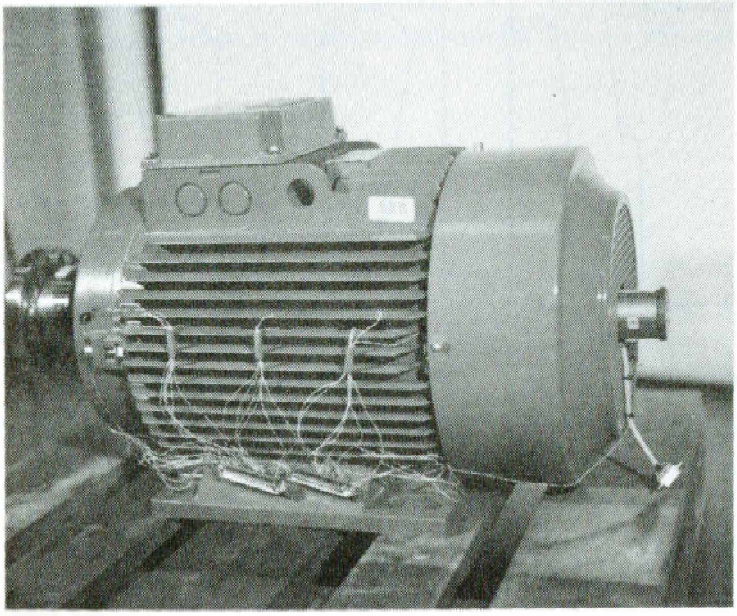

*Figure 4. The 15 kW test motor.*

## 2.2 Measurement of electrical and mechanical quantities

About 30 experiments were carried out for each test machine. Most of them were tests with constant load and frequency at a sinusoidal stator voltage. The machine was loaded until thermal equilibrium was reached, and then temperatures, torque, current, voltage, electrical power and speed were measured. Locked-rotor tests and tests with injected DC current in the stator windings were made at standstill. A few tests with transient temperature measurements and varying load were also performed. Thermal equilibrium was reached after approximately 4 hours for the larger machine and 2 hours for the smaller machine (depending on the speed). The voltage source was a synchronous generator, whose speed and excitation were controlled (see Fig. 5). Frequencies between 10 and 90 Hz were used. The test machines were star-connected, operated as motors and were loaded by converter-controlled DC machines.

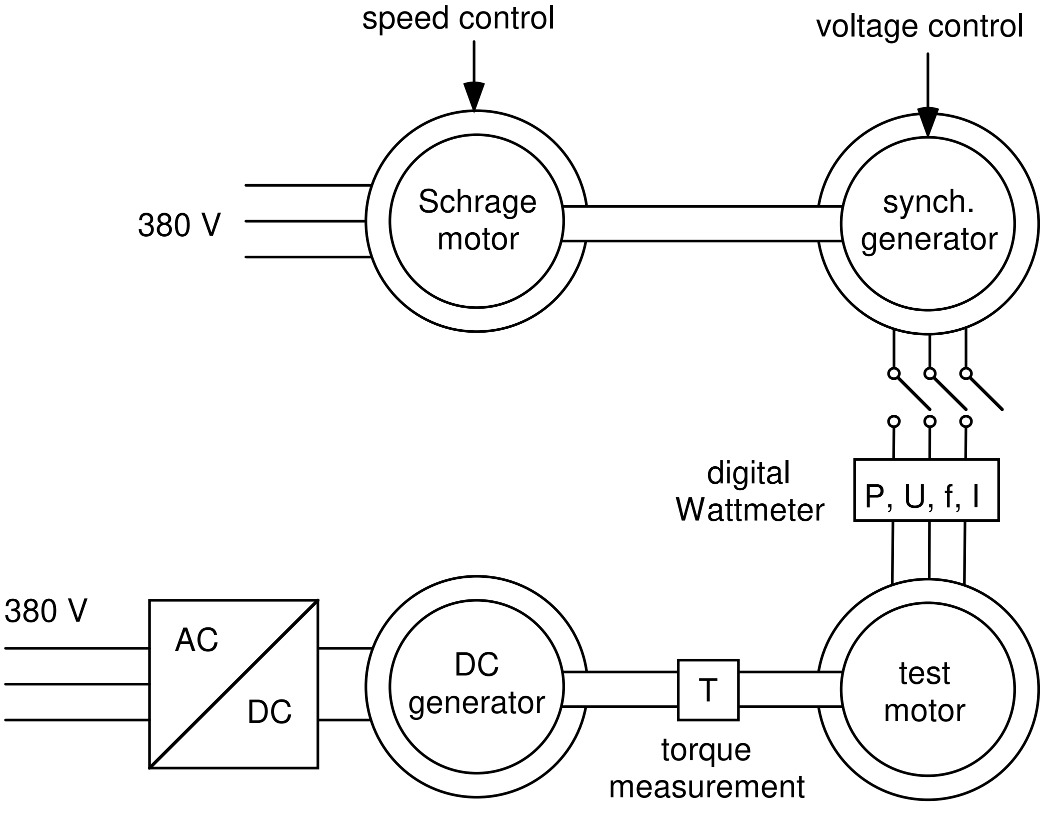
speed control
voltage control
380 V
Schrage motor
synch. generator
digital Wattmeter
P, U, f, I
380 V
AC
DC
DC generator
T
torque measurement
test motor

*Figure 5. Experimental setup.*

## 2.3 Temperature measurements

The location of the temperature sensors is shown in Figs 6 and 7. T-type thermocouples were used for the stator. The rotor temperatures were measured with platinum rtds (resistance thermometer devices). Insulated, twisted copper-wires were used as lead-ins. The wires were led through a drilled hole in the shaft and connected to a slip ring device on the fan side.

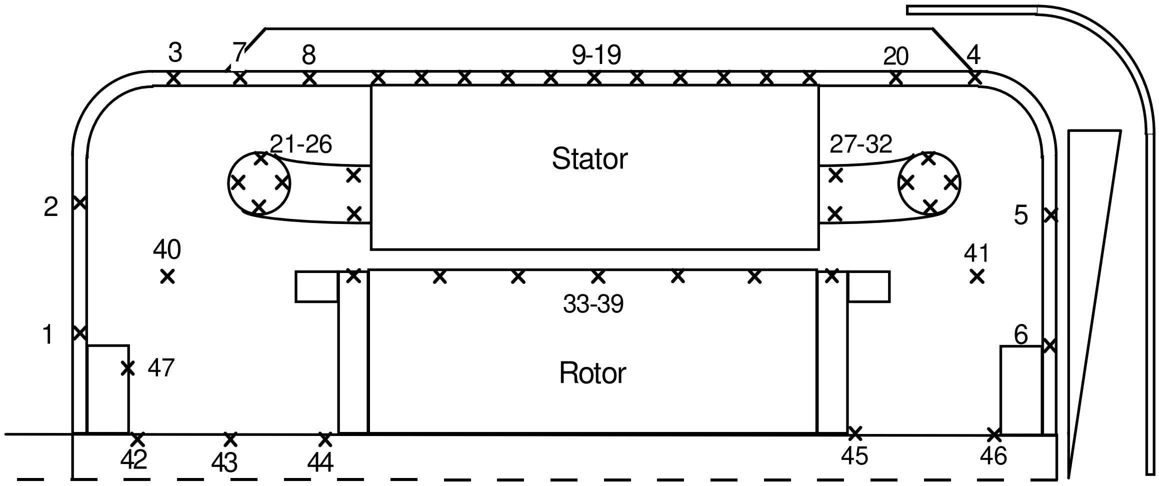
3
7
8
9-19
20
4
Stator
21-26
27-32
2
5
40
41
33-39
1
6
47
Rotor
42
43
44
45
46

*Figure 6. Location of the temperature sensors of the 15 kW machine. End shields: 1–6, Frame: 7–20, Stator end windings: 21–32, Rotor bars: 33–39, Internal air: 40–41, Shaft: 42–46, Bearing: 47.*

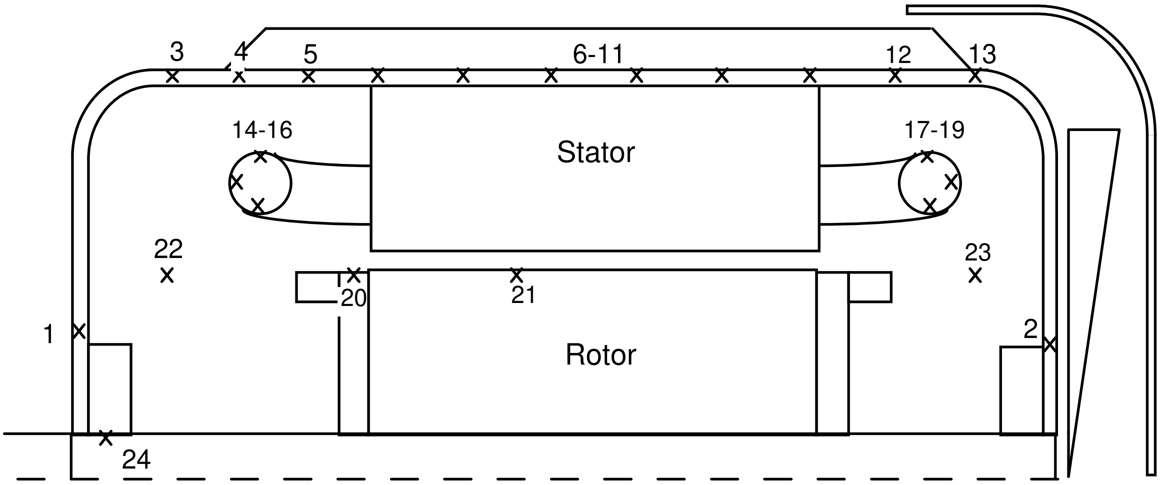
3
4
5
6-11
12
13
14-16
Stator
17-19
22
23
20
21
1
2
Rotor
24

*Figure 7. Location of the temperature sensors of the 4 kW machine. End shields: 1–3, Frame: 4–13, Stator end windings: 14–19, Rotor bars: 20–21, Internal air: 22–23, Shaft: 24.*

In the 15 kW rotor, 11 rtds were attached equally spaced along the shaft and rotor surface. A 3 mm deep slot was milled in a rotor bar for the sensors and their lead-in wires. The joints between the rtds and the lead-ins were insulated with Araldite. The sensors that were attached to the shaft were put down in small grooves made by a hack saw. On the 4 kW rotor, only three rtds were used, and they were measured without slip-ring device, by first stopping the rotor, measuring during some time, and then extrapolating the data points linearly back to the switch-off moment. No problems were encountered except that some of the rtds stopped working, probably because the soldering loosened.

The frame temperatures were primarily measured by T-type thermocouples having an uninsulated diameter of 0.2 mm and a teflon insulation of 0.15 mm thickness. An infra-red camera was also used, that was useful for determining the temperature differences along the frame, but could not be used to determine the absolute temperature, since the emissivity of the surface must then be exactly known. Because of this, the infrared camera was mainly used to check the readings of the thermocouples and to visualize the temperature distribution of the frame. The thermocouples were inserted and glued into small drilled holes, so that their positions were well defined. Despite the fact that thermally conducting glue (Electrolube TBS20S) was used, the cooling air in fact cooled down the thermocouples several degrees below the real temperature of the frame. To eliminate this problem, a length of about 2 cm of the thermocouple wires were covered by insulation tape along the bottom of the cooling channel.

Stator winding temperatures were measured by the resistance method and by thermocouples attached to the end windings. In the 15 kW machine, six thermocouples were placed on the fan side end windings and another six thermocouples were placed at the corresponding positions on the drive side end windings. In the 4 kW machine, three thermocouples were placed at the fan side and three at the drive side. To get a good thermal contact, the thermocouples were inserted into natural cavities in the end windings and bonded by Araldite.

The resistance method was used in the following way: After switch-off, a constant DC current was injected between two phases, and the voltage was measured by a computer during five minutes. The time between switch-off and the first measurement was measured manually, and the resistance of the stator windings at switch-off was obtained by linear extrapolation.

The average temperature of the stator windings was calculated from the relation

$$R = R_0 \frac{235\ ^\circ\mathrm{C} + T}{235\ ^\circ\mathrm{C} + T_0} \tag{1}$$

where $R$ is the resistance at temperature $T$ and $R_0$ is measured at $T_0$ = 20°C.

The temperature of the internal air was measured by rtds on the fan side and the drive side. The temperature of the drive side bearing of the 15 kW machine was measured by a thermocouple applied on a sealing plate. Naturally, the temperature of the ambient air was also measured. Figure 8 shows the different types of temperature sensors that were used.

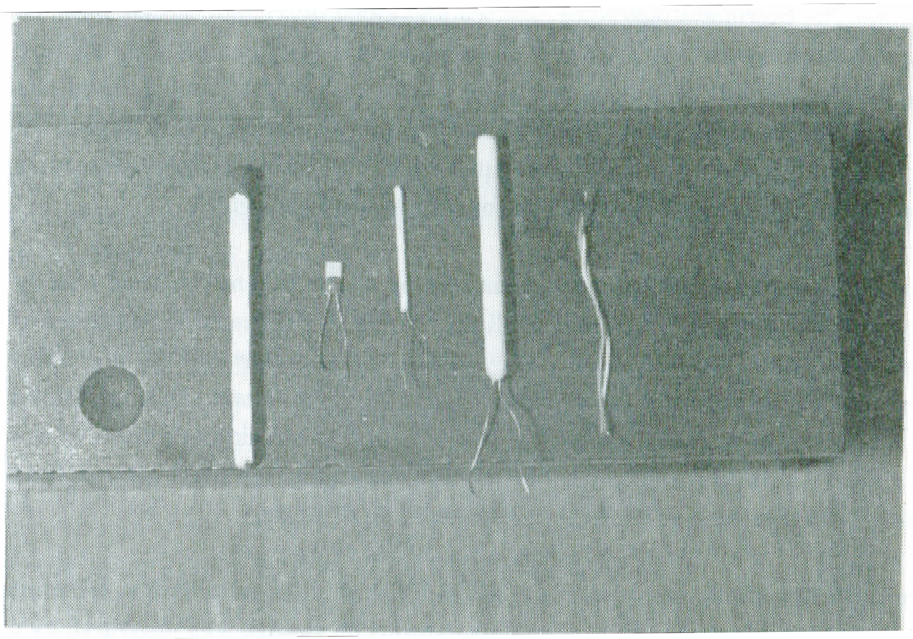

*Figure 8. Temperature sensors from the left: three 100 Ω rtds, of which the second to the left was mostly used. To the right there is a T-type thermocouple.*

## 2.4 Measurement errors

The specified tolerance of the thermocouples is 1.1 K in the relevant temperature range. All thermocouples were connected to a switch box by an adapter and compensation wire. The adapter was fastened to the machine base, enabling movement of the machine without having to bring along the box and the compensation wire. The temperature inside the switch box was measured by a calibrated rtd, whose accuracy is significantly better than that of a thermocouple. The thermoelectric voltages were measured with a resolution of 0.01 mV and an accuracy of 0.02 mV in the relevant temperature range, which corresponds to a maximum error of 0.6 K. All thermocouples and compensation wires were cut from the same reel of thread, which should lead to small individual variations. The rtds follow DIN 43760, class B, which means that the tolerance increases linearly with temperature; 0.3 K at 0°C and 0.8 K at 100°C. An error of 0.2 K can be added to this as a result of the ohm-meter error and the thermal drift of the lead-in resistance. The resulting maximum errors are 1.7 K for the thermocouples and 1.3 K for the rtds, and do not include the effects of imperfect thermal contact to the measurement object.

The main source of error when using the resistance method is probably that the purity of the copper is not exactly known. The resistance of a copper wire is partly due to the copper and partly due to impurities. The resistivity of copper is a linear function of temperature, but the resistivity due to impurity is constant [9]. Commercial copper wires are specified for a minimum of 97 % of the conductivity of pure copper. With exactly 97 % conductivity Eq. (1) is correct, but with, say, 100 % conductivity the number 235 becomes 228 in Eq. (1). This means that the resistance method would overestimate the temperature rise of a pure copper sample by 2.5 %, assuming negligible error in the resistance measurement. Thus, an error of 0–2.5 % can be expected for 97–100 % of the conductivity of pure copper. The error caused by the resistance measurement in itself is estimated to max. 3 %.

The two HBM T30FN torque measurement devices use strain gauges. Without going through the details, the accuracy is approximated to 1 % [10]. The Yokogawa 2533 wattmeter is digital and its accuracy is in the order of 0.2 %. The speed measurement accuracy is in the order of 0.1 %. The resulting accuracy of the total loss measurement then becomes approximately 8 % at an efficiency of 84 %, which is the measured rated efficiency of both test motors.

# 3 Loss modelling

## 3.1 Losses in induction machines

The losses in induction machines are defined in the IEC standard 34-2 [11], which also suggests how loss measurements can be performed. A distinction is normally made between no-load losses, that mainly depend on the voltage, and load losses, that are current-dependent. If the supply voltage is sinusoidal, the losses usually only have to be calculated for one frequency. For a variable-speed drive fed by a convertor, there are the additional problems of frequency dependence and harmonic losses.

### No-load losses

The following losses can be expected at no load with sinusoidal supply:

(a) core losses in the stator teeth and yoke, due to the main flux
(b) no-load stray losses
(c) losses due to friction and windage

The term *no-load stray losses* is here used for losses that are due to space harmonics and consequently are not of fundamental frequency. These are tooth pulsation losses, surface losses, losses due to interbar currents and circulating currents in the rotor [12,13,14,15,16,17,18,19]. Apart from the terms (a) to (c), there are of course also some resistive losses due to the no-load current.

### Load losses

The load losses at sinusoidal supply voltage are:

(a) resistive losses in the stator winding
(b) resistive losses in the rotor winding
(c) additional losses due to leakage flux and mmf space harmonics

The additional losses consist of similar components as the no-load stray losses. End losses and losses due to the skew leakage flux are also part of the additional losses.

### Losses at non-sinusoidal supply voltage

The dominating harmonic losses are

a) resistive losses in the stator and rotor windings caused by the harmonic currents and by skin effect
b) core losses and surface losses caused by the harmonic flux

It is often assumed that the harmonic losses are of the no-load type, but according to Nee [20], the harmonic losses increase with the load. This effect is due to saturation of the harmonic leakage flux path, which decreases the leakage reactance and thus increases the harmonic currents.

### 3.1.1 Resistive losses

The fundamental resistive losses of the stator and rotor are given by

$$P_{\mathrm{Cus}} = 3 R_{\mathrm{s}} I_{\mathrm{s}}^2 \tag{2}$$

$$P_{\mathrm{Cur}} = 3 R_{\mathrm{r}} I_{\mathrm{r}}^2 \tag{3}$$

where $R$ and $I$ are the resistance and current per phase, respectively, and the indices s and r stand for the stator and rotor, respectively. For the small wire diameter used in the stator windings of smaller TEFC motors, the skin effect of the stator windings can be neglected when the supply voltage is sinusoidal. Correction for the resistance change with temperature for copper can be made by Eq. (1).

Concerning the resistive losses in the rotor, it is assumed that the skin effect can be neglected for the fundamental rotor current. Correction for the resistance change with temperature for aluminium can be made by

$$R = R_0 \frac{245\,^\circ\mathrm{C} + T}{245\,^\circ\mathrm{C} + T_0} \tag{4}$$

To separate the losses of the end rings from the losses of the bars, the following ratio of bar losses to ring losses can be used

$$\frac{P_{\mathrm{bar}}}{P_{\mathrm{ring}}} = 2\sin^2\left(\frac{\pi p}{Q_{\mathrm{r}}}\right)\frac{\ell_{\mathrm{b}} A_{\mathrm{r}}}{A_{\mathrm{b}}\ell_{\mathrm{r}}} \tag{5}$$

where $p$ is the number of pole pairs, $Q_{\mathrm{r}}$ is the number of rotor slots, $A_{\mathrm{b}}$ and $\ell_{\mathrm{b}}$ are the area and length of a rotor bar, respectively. $A_{\mathrm{r}}$ and $\ell_{\mathrm{r}}$ are the area and length of a ring segment (i.e. between two bars), respectively.

### 3.1.2 Fundamental core losses

The core losses consist of hysteresis losses and eddy current losses. The hysteresis losses are proportional to the frequency and proportional to $B_{\max}^{1.6-2.4}$ (depending on saturation) where $B_{\max}$ is the peak flux density. In practice, hysteresis losses are commonly assumed to be proportional to $B_{\max}^2$ . The eddy current losses are proportional to the square of both the frequency and $B_{\max}$. Thus the core losses per mass unit are

$$Q = (k_{\mathrm{Hy}} f + k_{\mathrm{Ft}} f^2) B_{\max}^2 \tag{6}$$

where $k_{\mathrm{Hy}}$ and $k_{\mathrm{Ft}}$ are the loss factors of the material, and $f$ is the frequency. The eddy current loss factor is according to Richter [21]

$$k_{\mathrm{Ft}} = \frac{(4.44\,\Delta)^2}{12\,\rho\rho_{\mathrm{e}}} \tag{7}$$

where $\rho_{\mathrm{e}}$ is the resistivity, $\rho$ the density and $\Delta$ the lamination sheet thickness. The sum of the eddy current losses and hysteresis losses is usually available from Epstein tests at 50 or 60 Hz. However, the real losses of a stator core can be 50–100 % larger than the calculated ones. The losses are increased due to harmonics of the field variation and due to manufacturing (e.g. punching of the sheets). Temperature also effects the losses.

### 3.1.3 Friction and windage losses

The friction losses are located in the bearings and in the bearing sealings. The losses due to the sealings may in fact be larger than the actual bearing losses. The bearing friction torque consists of a constant part, that depends on the bearing forces, and a hydrodynamical part, which is strongly temperature-dependent and speed-dependent. The hydrodynamical part is usually dominant over the constant part. The bearing friction torque can be calculated using a method described by SKF [22]. The windage losses are mainly due to the fan. The windage losses are proportional to the cube of the speed, and do not lead to heating of the machine, since the energy is used to accelerate the cooling air. There are also some losses due to air gap friction, but these are small compared to the fan losses.

The total friction and windage losses can be measured by running the machine at no load at very low voltages. This is done by plotting the input power against the square of the voltage, and then extrapolating to zero voltage. The intersection corresponds to the total friction and windage losses. If a test is performed with the fan removed, the friction losses can be separated from the windage losses. If also the bearing sealings are removed, the bearing losses can be separated from the sealing losses. Figures 9 and 10 show the windage and friction losses of the two test machines separated in this way. Even though the machine was practically cold during this test, it was necessary to wait about 1 hour before the bearing losses had become stabilized.

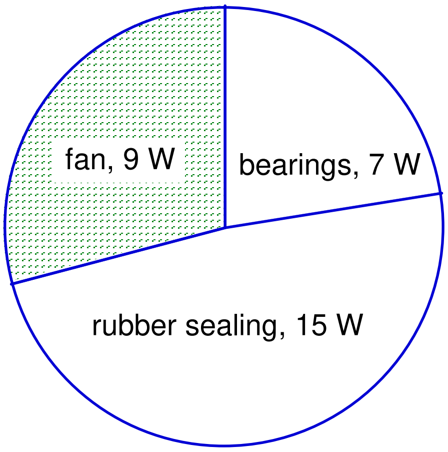

*Figure 9. Friction and windage losses, 4 kW-machine, rated speed.*

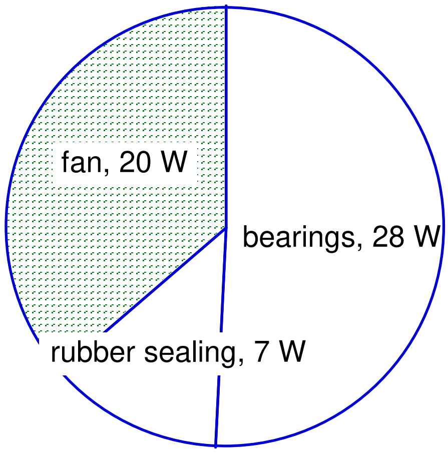

*Figure 10. Friction and windage losses, 15 kW-machine, rated speed.*

### 3.1.4 No-load stray losses and additional losses

The slots in induction machines cause permeance waves, that produce no-load stray losses in both the stator and the rotor. The nonsinusoidal mmf distribution in the air gap and the saturation of the magnetic circuit further add to the space harmonics. Some of the no-load stray losses are caused by eddy currents in the rotor teeth. These losses are usually divided into surface losses and tooth pulsation losses, where the surface losses are treated separately because they only appear in a thin surface layer, while the pulsation losses penetrate deeper. The penetration depth of the pulsations depends on the design of the rotor cage. Since each rotor tooth is surrounded by short-circuited rotor bars, circulating currents will occur which limit the penetration depth of the permeance waves. The surface losses are influenced by the finish of the rotor surface.

The magnitude and nature of the stray losses depend on if the rotor bars are skewed or not. Rotors with non-skewed bars were discussed by Alger [12, 13], who suggests some empirical relations. The non-skewed problem was also analysed by Arkkio [14,15], who used time-stepping finite element analysis to calculate the losses, both at load and no-load. Skewed bars were treated by Cristofides [16]. In rotors with non-skewed bars the losses due to circulating currents are relatively larger and the tooth eddy current losses smaller than with skewed bars.

When the bars are skewed and uninsulated, there are also resistive losses caused by interbar currents. The losses due to interbar currents can be large, and depend among other things on the contact resistance between the bars and the rotor core. The losses are described by Odok [18] and Cristofides and Adkins [19], who performed measurements on 5 kW induction motors with different rotors. The interbar currents decrease with ageing, since layers of oxide are formed at the interface between the bars and the core.

Additional losses are the total load losses minus the fundamental resistive losses. They are basically of the same kind as the no-load stray losses, but much increased due to the mmf-waves occurring at load. A part of the additional losses is also the end losses, which depend on axial leakage flux that penetrates the rotor and stator ends and to a certain extent the end shields and the frame. The end losses are influenced by the distance between the end windings and other conducting machine details. According to Alger et al. [12], the losses are 0.3 times the apparent power in that part of the end winding reactance that is due to flux penetrating the stator core axially. Applying this rule for the test motors results in rather small end losses. A rotor-removed test for the 15 kW motor also implied that the end losses are small for induction machines of the same size as the test motors [10].

Another component of the additional losses, that also increases the core losses at the ends, is caused by skew. If the rotor bars are skewed, there is a phase displacement of the fundamental mmf-waves of the stator and rotor at the two ends of the core. This causes a certain increase in the peak flux at the ends, which explains the extra losses, which according to [12] are given by

$$P_{\mathrm{sk}} = \frac{\pi^2 P_0}{12}\left(\frac{2p\sigma I_{\mathrm{sa}}}{Q_{\mathrm{s}} I_0}\right)^2 \tag{8}$$

where $\sigma$ is the ratio of skew to one stator slot pitch (normally 1), $I_{\mathrm{sa}}$ is the active part of the stator current, $I_0$ is the no-load current and $P_0$ is the no-load core losses.

## 3.2 Current and slip calculation

In order to calculate the resistive losses, the stator and rotor currents are needed. The currents are primarily functions of the torque, frequency and voltage. The slip is needed to calculate the speed of the machine, which influences some of the parameters of the thermal model.

### 3.2.1 Equivalent circuit

A specific induction machine can be represented by the equivalent circuit shown in Fig. 11. The equivalent circuit is only used for the fundamental voltage component. If the supplying voltage is nonsinusoidal, the harmonic currents and losses can be calculated using equivalent circuits for harmonics.

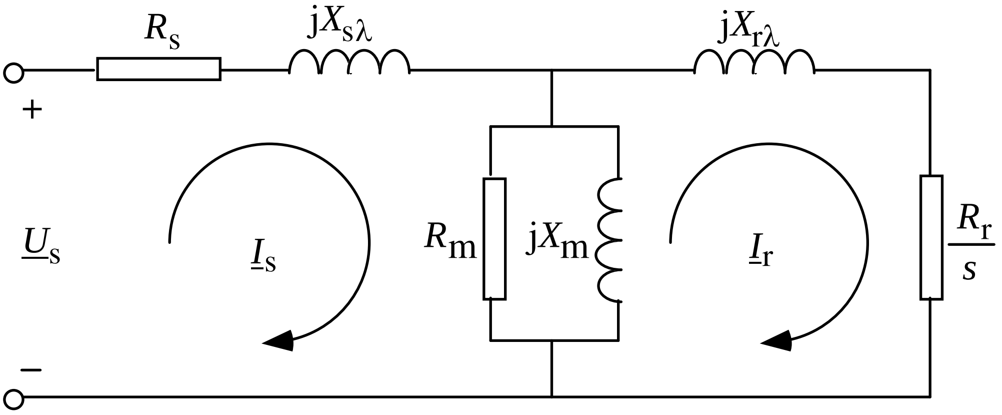

*Figure 11. The equivalent circuit of the induction machine.*

$R_s$ and $R_r$ are the stator and rotor resistances per phase. $X_{s\lambda}$ and $X_{r\lambda}$ are the stator and rotor leakage reactances per phase. $X_m$ is the magnetizing reactance, $U_s$ is the phase voltage, $s$ is the slip and $R_m$ is a resistance used to model the stator core losses. The two currents can be solved from an equation system consisting of two complex equations. Usually $R_m$>>$X_m$, which leads to

$$\begin{bmatrix} \underline{U}_s \\ 0 \end{bmatrix} = \begin{bmatrix} R_s + \frac{X_m^2}{R_m} + j\left(X_m + X_{s\lambda}\right) & -\left(\frac{X_m^2}{R_m} + jX_m\right) \\ -\left(\frac{X_m^2}{R_m} + jX_m\right) & \frac{R_r}{s} + \frac{X_m^2}{R_m} + j\left(X_m + X_{r\lambda}\right) \end{bmatrix} \begin{bmatrix} \underline{I}_s \\ \underline{I}_r \end{bmatrix} \quad (9)$$

The parameters are not constant. $R_s$, $R_r$ and $X_m$ are temperature-dependent ($X_m$ because the air gap changes with temperature). All reactances and also $R_m$ are frequency-dependent. $X_m$ is also flux-dependent, due to saturation. The equation system can not be solved in one step; a few iterations must first be passed through. This is because the slip is not known from the beginning and, consequently, an initial value must first be assumed. Usually, the additional losses are neglected and the no-load core losses are modelled by $R_m$. However, if there is a large portion of additional losses or no-load stray losses, this will cause errors when computing the currents. Basically, the additional losses and the no-load stray losses act as a brake upon the rotor [23] and should consequently be treated as an extra load. For the shaft torque $T_s$, we then have

$$T_s = \frac{3pR_r I_r^2}{2\pi f s} \pm \frac{(P_f + P_{st})}{\omega} \tag{10}$$

where the plus sign is valid if $s$ is negative. $P_{st}$ is the combined additional losses and no-load stray losses, and $P_f$ is the friction losses.

The flux dependence of $X_m$ is only worth considering if the machine is operated on a non-constant flux basis or as a generator. To calculate $X_m$, no-load tests were performed at different voltages at 50 Hz, see Fig. 12.

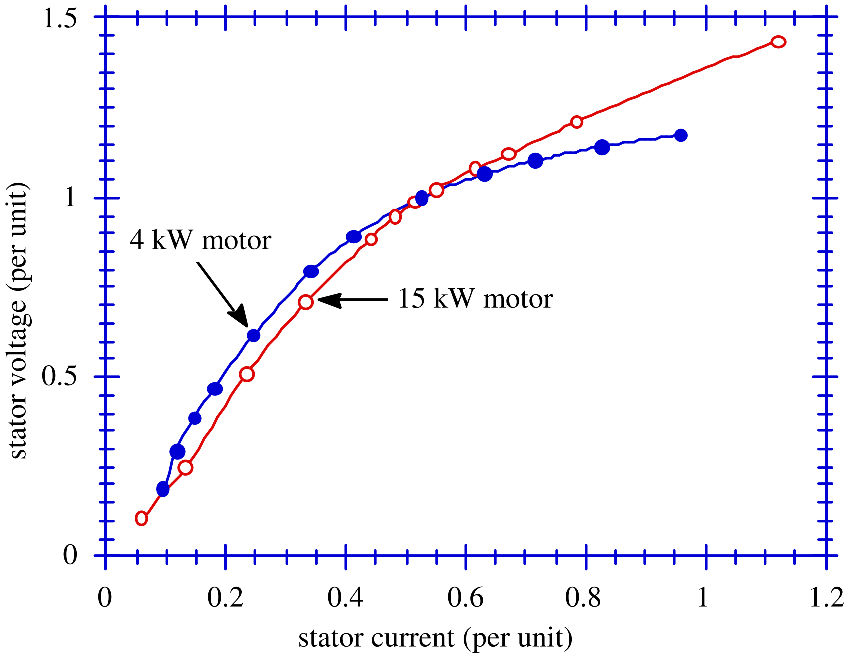

*Figure 12. No-load curves for the test machines at 50 Hz.*

The no-load test is performed with a cold machine for different values of the emf $U_\mathrm{m}$ induced by the fundamental air-gap flux. A function $X_\mathrm{m}=\mathrm{g}(U_\mathrm{m})$, which is valid for 50 Hz, can be constructed from the data points. To calculate $X_\mathrm{m}$ for other frequencies and to include the temperature dependence the following formula is used

$$X_\mathrm{m} = \mathrm{g}\left( U_\mathrm{m} \frac{f_0}{f} \right) \frac{f}{f_0} k_\delta \tag{11}$$

where $f_0$=50 Hz and the factor $k_\delta$ accounts for air gap shrinkage, caused by thermal expansion of the rotor, and is calculated by

$$k_\delta = \frac{\delta_\mathrm{e}}{\delta_\mathrm{e} - \kappa_\mathrm{Fe} r_\delta \Delta T} \tag{12}$$

where $\delta_\mathrm{e}$ is the equivalent air gap of a cold machine, $\kappa_\mathrm{Fe}$ is the thermal expansion coefficient of iron, $r_\delta$ is the average radius of the air gap, $\Delta T$ is the temperature drop over the air gap.

In Fig. 13, a flow chart is shown of a program that solves Eq. (9) and calculates the losses of the machine. To get a fast solution, the new value of the slip should be properly chosen for each iteration. A fast convergence is obtained by using

$$s_k = s_{k-1} + c \frac{f_0 T_\mathrm{err}}{f} \tag{13}$$

where $T_\mathrm{err}$ is the error in the torque calculation. The constant $c$ is specific for the machine and should be chosen as the ratio of the rated slip to the rated torque. Equation (13) gives convergence for generator operation as well as for motor operation and for operation near the synchronous speed.

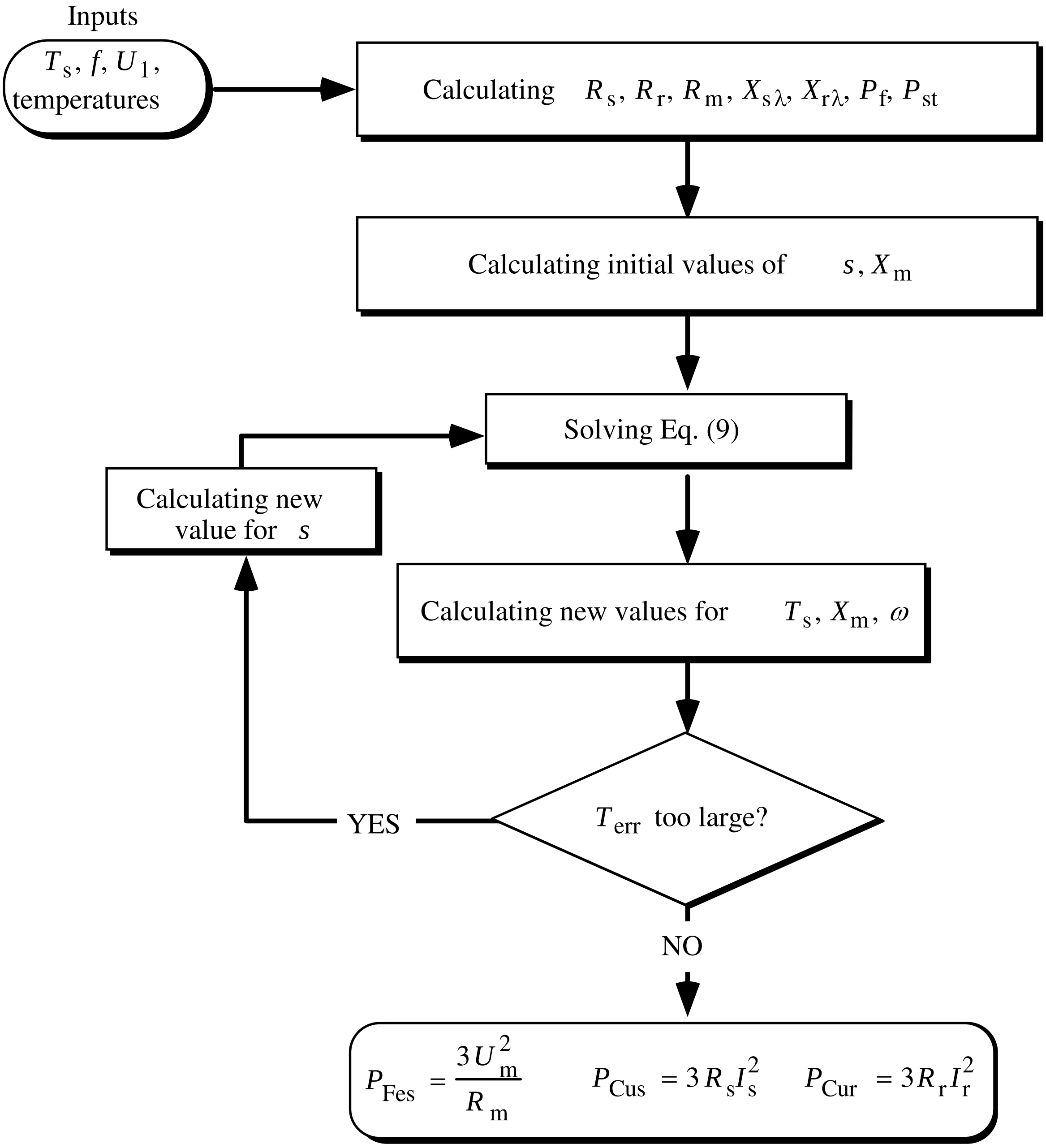
Inputs
$T_s$, $f$, $U_1$, temperatures
Calculating $R_s$, $R_r$, $R_m$, $X_{s\lambda}$, $X_{r\lambda}$, $P_f$, $P_{st}$
Calculating initial values of $s$, $X_m$
Solving Eq. (9)
Calculating new value for $s$
Calculating new values for $T_s$, $X_m$, $\omega$
$T_{err}$ too large?
YES
NO
$P_{Fes} = \frac{3U_m^2}{R_m}$ $P_{Cus} = 3R_sI_s^2$ $P_{Cur} = 3R_rI_r^2$

*Figure 13. Flow chart for a program that calculates the losses due to the fundamental currents and flux.*

### 3.2.2 Equivalent circuit for harmonics

It is assumed that the influence of the load and the harmonic iron losses can be neglected, an assumption that is commonly made [20]. The effect of harmonic voltages on an induction motor can then be evaluated by the use of equivalent circuits and the principle of superposition [24]. An independent equivalent circuit can be developed for each harmonic frequency, and each harmonic voltage can be applied to its respective equivalent circuit. The total harmonic loss is then equal to the sum of the losses of each equivalent circuit. As a general rule, the order of harmonics from three-phase converter equipment is given by $n = 3k \pm 1$, where + and – signify positive and negative phase sequences, respectively. Assuming balanced supply and symmetrical load, there are no even harmonics, which means $k$=2,4,6,... For small values of the fundamental slip, the harmonic slip is given by

$$s_n = \frac{3k}{3k \pm 1} \tag{14}$$

The harmonic slip is thus close to unity, which makes it possible to neglect $R_\mathrm{m}$ and $X_\mathrm{m}$ in the equivalent circuit for harmonics, shown in Fig. 14.

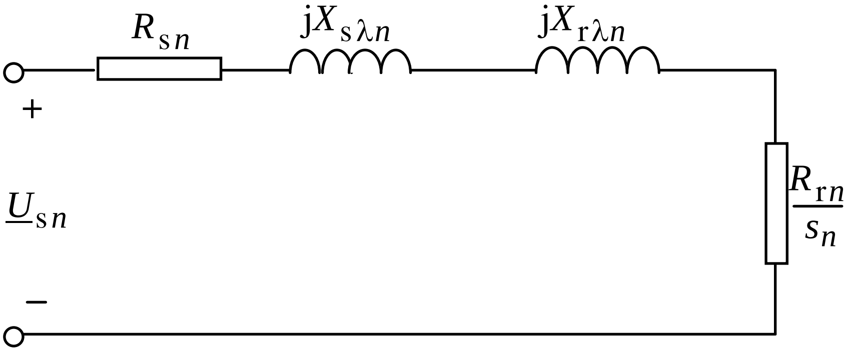
$R_{\mathrm{s}n}$
$\mathrm{j}X_{\mathrm{s}\lambda n}$
$\mathrm{j}X_{\mathrm{r}\lambda n}$
+
$\underline{U}_{\mathrm{s}n}$
–
$\frac{R_{\mathrm{r}n}}{s_n}$

*Figure 14. Equivalent circuit for harmonics.*

**Skin effect factors**

The skin effect is small for random-wound stator windings, but not entirely negligible for harmonics. The skin effect of the end windings can be neglected. A skin effect factor for the slot part of the stator winding resistance, valid for circular conductors in rectangular slots, is given by Schuisky [25].

Skin effect factors of rotor bars are best calculated by the finite element method, but for some slot shapes, e.g. rectangular or circular, simple formulas can be used. If the top of the bar is rectangular or wedge-shaped, it may be possible to neglect the rest of the bar and calculate the skin effect factor as for a rectangular bar. This is possible if the skin depth, given by

$$\delta_{\mathrm{R}} = \sqrt{\frac{\rho_{\mathrm{e}}}{\pi \mu_0 f}} \tag{15}$$

is at least 2–3 times smaller than $h$, the height of the rectangular top-of-bar segment. The skin effect factor for a rectangular bar is according to Schuisky [25]

$$k_{\mathrm{R}} = \xi \frac{\sinh(2\xi) + \sin(2\xi)}{\cosh(2\xi) - \cos(2\xi)} \tag{16}$$

where

$$\xi = \frac{h}{\delta_{\mathrm{R}}} \tag{17}$$

The skin effect of the end rings is according to Schuisky small compared with the skin effect of the bars, and since the resistance of the bars is larger than that of the end rings even at fundamental frequency, the skin effect of the end rings can be neglected.

The rotor slot leakage inductance has a non-linear frequency dependence; it decreases with frequency. A skin effect factor for the rotor slot leakage inductance of a rectangular rotor slot is given by

$$k_{\mathrm{L}} = \frac{3}{2\xi} \frac{\sinh(2\xi) - \sin(2\xi)}{\cosh(2\xi) - \cos(2\xi)} \tag{18}$$

## 3.3 Losses of the test motors

The total losses of the two test machines were measured by subtracting the output power from the input power. The output power was obtained by measuring the shaft torque and the speed, and the input power was measured by a wattmeter.

An attempt to calculate the total electromagnetic losses was made by a time-stepping finite element analysis of the electromagnetic field. The method is an eddy-current model, which takes the rotation of the rotor into account, and is further described by Arkkio [15]. The analysis is based on the assumption of a two-dimensional field. The end region fields are taken into account by the end winding impedances in the circuit equations of the windings. The iron core is modelled as a non-conducting, nonlinear material having a single-valued magnetization curve. This means that the iron losses are neglected in the solution of the magnetic field. The losses in the stator and rotor windings are directly obtained from the solution, and the core losses are indirectly calculated from the field analysis. This is done by computing the Fourier-components for the amplitude of the flux density as a function of the position in the core. The core losses in each volume element are obtained by superposition, using Eq. (6) for each Fourier-component. The limitations of the method are mainly that it does not properly account for skewed rotors and it neglects interbar currents. The end losses and the effects of mechanical working of the rotor surface are also neglected. However, the method is believed to predict the core losses in the stator yoke and teeth with reasonable accuracy, even for skewed rotors.

In order to separate the loss components in the test motors, the resistive losses of the stator windings and the friction and windage losses were first measured. The resistive losses of the rotor winding (due to the fundamental current) were calculated using the flow chart in Fig. 13, and the stator core losses were taken from the finite element analysis. Most of the remaining losses are additional losses and no-load stray losses in the rotor $P_{\mathrm{str}}$, and they are calculated by subtracting all the other loss components from the measured total losses. Since the estimated accuracy of the total loss measurement is 8 %, $P_{\mathrm{str}}$ is a rather uncertain approximation. However, for the 15 kW motor, the value is probably useful, because $P_{\mathrm{str}}$ was then almost 30 % of the total losses, and comparisons with the results of the thermal calculations also indicate that the calculated value is close to the real one.

The losses for rated load and no load at 50 Hz are shown in Figs 15–18. Other load cases are presented in Tables 1 and 2.

| | | | |
|---|---|---|---|
| $P_{\mathrm{Cus}}$ | stator winding losses | $P_{\mathrm{f}}$ | friction and windage losses |
| $P_{\mathrm{t}}$ | stator teeth losses | $P_{\mathrm{y}}$ | stator yoke losses |
| $P_{\mathrm{Cur}}$ | rotor winding losses due to the fundamental rotor current | $P_{\mathrm{str}}$ | no-load stray losses and additional losses in the rotor |

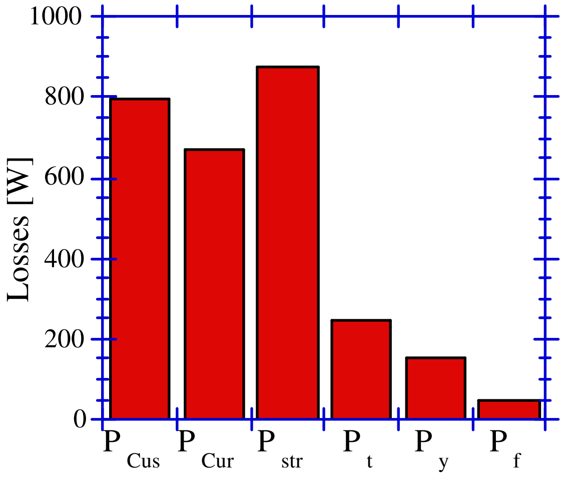

*Figure 15. Losses of the 15 kW motor at rated load.*

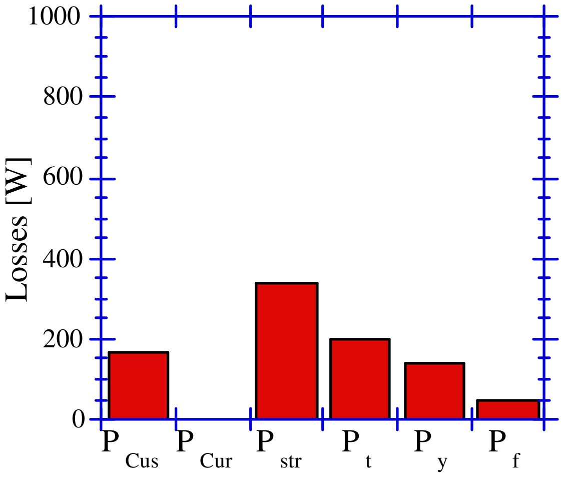

*Figure 16. Losses of the 15 kW motor at no load.*

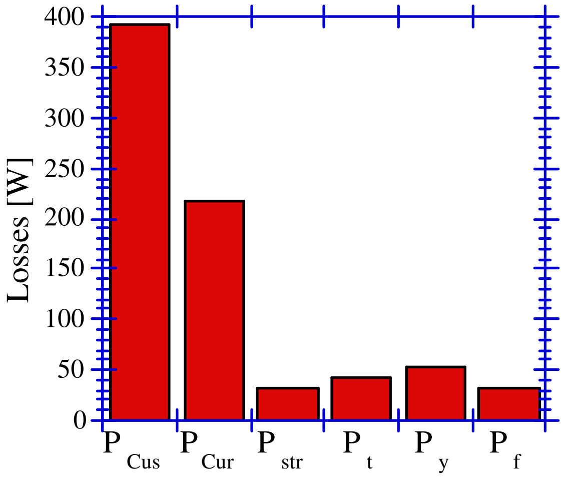

*Figure 17. Losses of the 4 kW motor at rated load.*

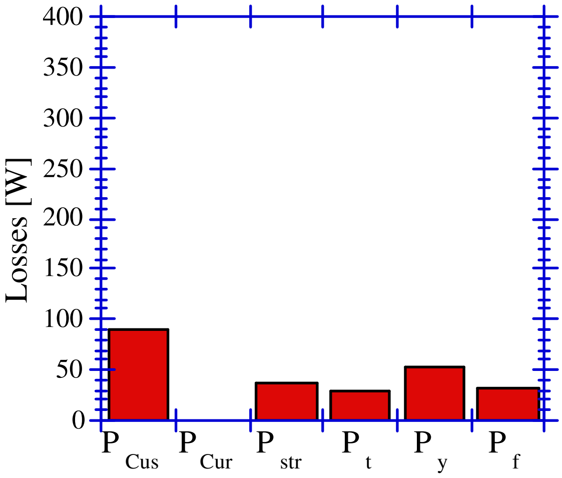

*Figure 18. Losses of the 4 kW motor at no load.*

*Table 1. Losses of the 4 kW motor. Frequency, line voltage and torque were measured. The total losses $P_{\mathrm{tot}}$, the friction and windage losses $P_{\mathrm{f}}$, and the stator winding losses $P_{\mathrm{Cus}}$ were also measured. The stator yoke losses $P_{\mathrm{y}}$, the stator teeth losses $P_{\mathrm{t}}$, and the rotor winding losses due to the fundamental rotor current $P_{\mathrm{Cur}}$ were calculated. The combined no-load stray losses and additional losses in the rotor $P_{\mathrm{str}}$ were calculated as $P_{\mathrm{tot}}–P_{\mathrm{f}}–P_{\mathrm{Cus}}–P_{\mathrm{y}}–P_{\mathrm{t}}–P_{\mathrm{Cur}}$.*

| $f$ [Hz] | $U$ [V] | $T$ [Nm] | $P_{\mathrm{tot}}$ [W] | $P_{\mathrm{f}}$ [W] | $P_{\mathrm{Cus}}$ [W] | $P_{\mathrm{y}}$ [W] | $P_{\mathrm{t}}$ [W] | $P_{\mathrm{Cur}}$ [W] | $P_{\mathrm{str}}$ [W] |
|---|---|---|---|---|---|---|---|---|---|
| 11.1 | 85 | 0.0 | 113 | 4 | 90 | 7 | 3 | 0 | 9 |
| 10.6 | 86 | 17.7 | 318 | 4 | 208 | 9 | 5 | 98 | -6 |
| 30.3 | 231 | 0.0 | 169 | 14 | 91 | 31 | 16 | 0 | 17 |
| 29.6 | 227 | 17.6 | 351 | 14 | 204 | 28 | 16 | 80 | 9 |
| 29.5 | 226 | 26.7 | 722 | 14 | 413 | 25 | 20 | 243 | 7 |
| 50.4 | 287 | 0.0 | 138 | 31 | 32 | 31 | 16 | 0 | 28 |
| 49.0 | 373 | 0.0 | 239 | 31 | 89 | 54 | 29 | 0 | 36 |
| 50.0 | 434 | 0.0 | 398 | 31 | 203 | 75 | 40 | 0 | 49 |
| 49.8 | 376 | 17.9 | 445 | 31 | 209 | 53 | 39 | 84 | 29 |
| 48.8 | 371 | 26.7 | 768 | 31 | 392 | 52 | 43 | 218 | 32 |
| 69.5 | 523 | 0.0 | 338 | 48 | 85 | 84 | 44 | 0 | 77 |
| 69.2 | 520 | 17.6 | 528 | 48 | 207 | 83 | 63 | 81 | 46 |
| 69.9 | 525 | 26.6 | 861 | 48 | 387 | 84 | 80 | 213 | 49 |
| 88.4 | 597 | 0.0 | 367 | 92 | 55 | 92 | 49 | 0 | 79 |
| 89.2 | 591 | 17.6 | 641 | 92 | 207 | 94 | 97 | 106 | 45 |

The measurements were made at thermal equilibrium at the end of each heat run. There is one negative value of $P_{\mathrm{str}}$, which probably is explained by underestimation of $P_{\mathrm{tot}}$ or possibly overestimation of $P_{\mathrm{Cur}}$. Due to limitations of the control system, the frequency could not be regulated to exactly the desired values. The voltage was therefore adjusted in order to maintain the $U/f$ ratio at the rated condition. At 90 Hz, however, the voltage was reduced for safety reasons. The friction and windage losses $P_{\mathrm{f}}$ were measured at no load for 4 different speeds and are not corrected for speed or temperature differences.

*Table 2. Losses of the 15 kW motor. Frequency, line voltage and torque were measured. The total losses* $P_{\mathrm{tot}}$*, the friction and windage losses* $P_{\mathrm{f}}$*, and the stator winding losses* $P_{\mathrm{Cus}}$ *were also measured. The stator yoke losses* $P_{\mathrm{y}}$*, the stator teeth losses* $P_{\mathrm{t}}$*, and the rotor winding losses due to the fundamental rotor current* $P_{\mathrm{Cur}}$ *were calculated. The combined no-load stray losses and additional losses in the rotor* $P_{\mathrm{str}}$ *were calculated as* $P_{\mathrm{tot}}-P_{\mathrm{f}}-P_{\mathrm{Cus}}-P_{\mathrm{y}}-P_{\mathrm{t}}-P_{\mathrm{Cur}}$*. Some of the heat runs were repeated after the first round of tests. The repeated heat runs are shown below the double line .*

| $f$ [Hz] | $U$ [V] | $T$ [Nm] | $P_{\mathrm{tot}}$ [W] | $P_{\mathrm{f}}$ [W] | $P_{\mathrm{Cus}}$ [W] | $P_{\mathrm{y}}$ [W] | $P_{\mathrm{t}}$ [W] | $P_{\mathrm{Cur}}$ [W] | $P_{\mathrm{str}}$ [W] |
|---|---|---|---|---|---|---|---|---|---|
| 10.1 | 75 | 0 | 260 | 4 | 161 | 21 | 21 | 0 | 53 |
| 9.6 | 71 | 97 | 784 | 4 | 419 | 18 | 18 | 277 | 48 |
| 30.1 | 228 | 0 | 550 | 15 | 167 | 75 | 92 | 0 | 201 |
| 30.1 | 229 | 99 | 1099 | 15 | 405 | 72 | 96 | 235 | 276 |
| 28.9 | 216 | 149 | 2245 | 15 | 871 | 63 | 85 | 738 | 473 |
| 49.3 | 375 | 0 | 900 | 50 | 169 | 141 | 201 | 0 | 339 |
| 50.0 | 460 | 0 | 1480 | 50 | 418 | 221 | 306 | 1 | 484 |
| 50.8 | 388 | 99 | 1633 | 50 | 417 | 146 | 227 | 247 | 546 |
| 51.8 | 394 | 148 | 2792 | 50 | 797 | 150 | 247 | 671 | 877 |
| 69.7 | 528 | 0 | 1310 | 100 | 164 | 223 | 353 | 0 | 470 |
| 69.8 | 537 | 99 | 2154 | 100 | 419 | 233 | 399 | 250 | 753 |
| 90.1 | 523 | 0 | 1130 | 200 | 80 | 185 | 313 | 0 | 352 |
| 88.7 | 581 | 94 | 2557 | 200 | 416 | 244 | 486 | 321 | 890 |
| 29.7 | 226 | 147 | 2039 | 15 | 807 | 68 | 92 | 671 | 386 |
| 49.5 | 375 | 0 | 870 | 50 | 172 | 141 | 201 | 0 | 306 |
| 50.8 | 385 | 98 | 1581 | 50 | 411 | 144 | 224 | 242 | 510 |
| 47.9 | 364 | 148 | 2631 | 50 | 810 | 133 | 213 | 672 | 753 |

From the repeated heat runs below the double line in Table 2 it can be seen that $P_{\mathrm{str}}$ has decreased by 10–20 % since the first heat run. This can be explained by oxidation in the interface between the rotor bars and the rotor core, which decreases the losses due to interbar currents.

## 3.4 Treatment of core losses and additional losses

The loss model must be able to calculate and to separate the core losses and the additional losses into stator yoke losses, stator teeth losses and rotor losses. According to the FEM-calculations, the stator yoke losses do not change much with the load. This may be explained by the increasing leakage flux, which counterbalances the decrease in main flux. It is thus suggested that

$$P_y = U_s^2\left(c_1 + \frac{c_2}{f}\right) \tag{19}$$

where $c_1$ and $c_2$ depend on the individual weight between eddy current losses and hysteresis losses. If this weight is known, $c_1$ and $c_2$ can be calculated from the loss data of the electrical steel manufacturer. The loss data should be multiplied by an empirical factor for mechanical working. According to the manufacturer of the test machines, a suitable correction factor is 1.3.

For the stator teeth losses, the load-dependence is not negligible. Figures 19 and 20 show the stator teeth losses of the test motors, calculated by the finite element method, as a function of the rotor current. The three calculated load cases correspond to no load, 2/3 rated torque, and rated torque. The line voltage is different for each case, in order to get the same value of $U_m$.

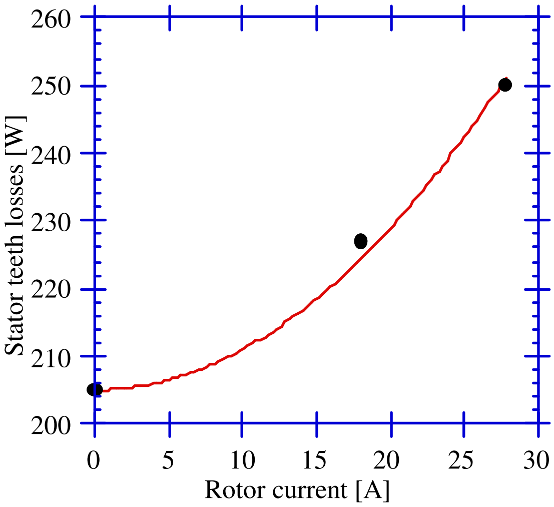

*Figure 19. The calculated stator teeth losses of the 15 kW motor at 50 Hz and with $U_m$=206 V.*

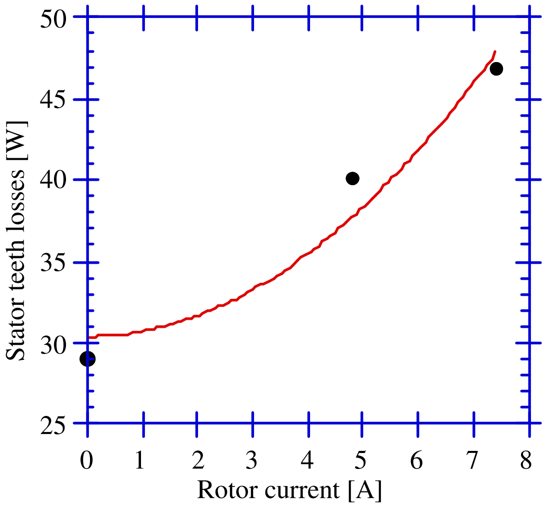

*Figure 20. The calculated stator teeth losses of the 4 kW motor at 50 Hz and with $U_m$=207 V.*

IEC [11] recommends that the total additional losses are assumed to be proportional to the square of the stator current. If instead the additional losses are assumed to be proportional to the square of the rotor current, there is no need to correct for the stator no-load current. It is suggested that the frequency dependence, the voltage dependence and the load dependence can be separated into factors so that the stator teeth losses are

$$P_{\mathrm{t}} = U_{\mathrm{m}}^2 \left(1 + c_3 I_{\mathrm{r}}^2\right)\left(c_4 + \frac{c_5}{f}\right) \tag{20}$$

where $c_3$ depends on the additional losses in the stator teeth and can be approximated from Figs 19 and 20. $c_4$ and $c_5$ depend on the individual weight between eddy current losses and hysteresis losses. The values of $c_3$, $c_4$ and $c_5$ depend very much on the slot geometry, and the best way of calculating them is by comparing results from the finite element analysis for different loads and frequencies.

As mentioned, a finite element method can be used to calculate the losses in the rotor, but the present method can only be assumed to give reliable results for non-skewed rotors. This is a problem, since most smaller induction motors have skewed rotors. According to Oberretl [17], some factors that can make the rotor losses high are skewing, higher number of rotor slots than stator slots, and open stator slots. IEC [11] states a value of the total additional losses at rated load of 0.5 % of the input power. However, for small machines the additional losses are often larger. Alger et al. [12] investigated the additional losses of 24 induction motors with closed rotor slots and varying degree of skew, and found that the total additional losses usually were 1–2 % of the rated output power. It is suggested that the additional rotor losses at rated load are assumed to be 1 % of the rated output power, if the rotor is skewed with closed slots. The combined no-load stray losses and additional losses in the rotor are assumed to follow a relation of the same type as Eq. (20).

Figures 21 and 22 show the measured no-load stray losses of the test rotors. Figure 23 shows the combined no-load stray losses and additional losses of the 15 kW rotor. Examining the no-load stray losses of the 15 kW machine at different frequencies indicated a linear frequency dependence, so that $c_4$ in fact can be neglected. However, this can simply be a coincidence, since the 15 kW machine, with its high losses, is not really representative for this class of machines. It is difficult to draw any conclusions about the frequency dependence of the no-load stray losses of the 4 kW machine. The curve fit in Fig. 23 shows that the additional rotor losses are proportional to the square of $I_r$. If, rather arbitrarily, the no-load stray losses are assumed to be equal to the additional losses at rated load, a value of $c_3$ can be calculated.

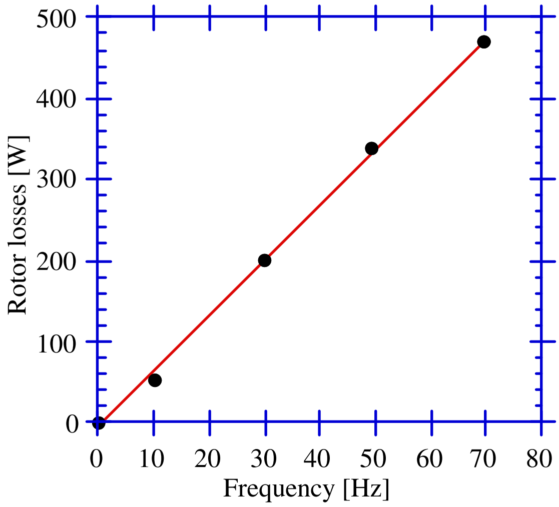

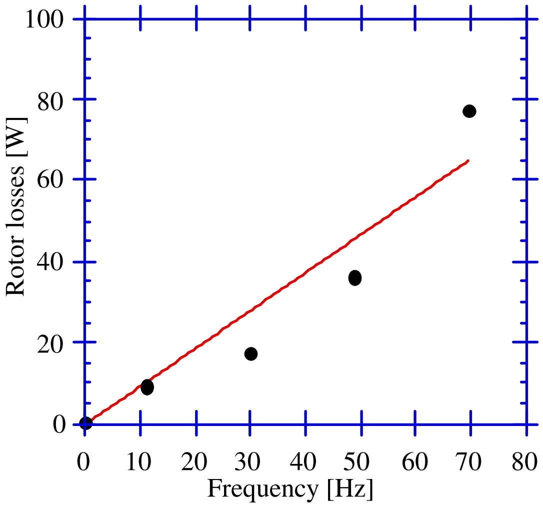

*Figure 21. The no-load stray losses in the rotor as a function of the stator frequency (15 kW motor).*

*Figure 22. The no-load stray losses in the rotor as a function of the stator frequency (4 kW motor).*

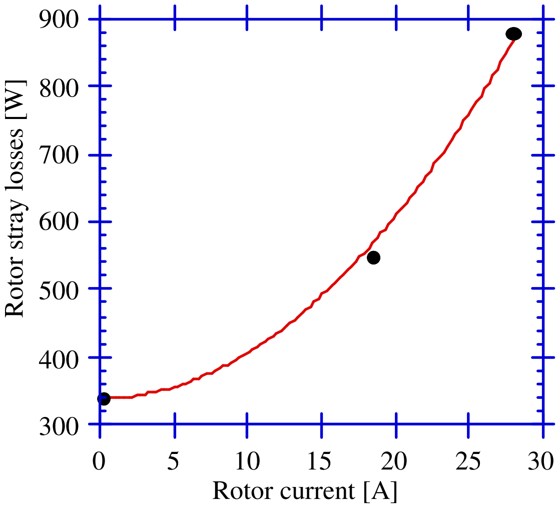

*Figure 23. The combined no-load stray losses and additional losses in the rotor at 50 Hz as a function of the rotor current (15 kW motor).*

The data points in Fig. 23 are not corrected for differences in $U_m$. By assuming a quadratic dependence on $U_m$, $P_{str}$ can be corrected to the no-load case ($U_m$=205 V) by multiplication by 1.03 at $I_r$=18 A and by 1.07 at $I_r$=28 A.

# 4 Thermal networks

## 4.1 Heat transfer basics

The thermal resistances that branch the nodes in a thermal network can be divided into some categories, which are well described in the basic heat transfer literature [26].

### Heat conduction

The general equation for heat conduction is

$$\rho c \frac{\partial T}{\partial t} = \frac{\partial}{\partial x}\left( \lambda_x \frac{\partial T}{\partial x} \right) + \frac{\partial}{\partial y}\left( \lambda_y \frac{\partial T}{\partial y} \right) + \frac{\partial}{\partial z}\left( \lambda_z \frac{\partial T}{\partial z} \right) + Q \tag{21}$$

where $\rho$ is the density, $\lambda$ the thermal conductivity, $T$ the temperature and $Q$ the dissipated power density. In many cases only one-dimensional heat flux needs to be considered. The heat flux is then

$$q = -\lambda \frac{\partial T}{\partial x} \tag{22}$$

and the one-dimensional thermal resistance between two points $x_1$ and $x_2$ is

$$R_{\mathrm{th}} = \frac{x_2 - x_1}{\lambda A} \tag{23}$$

where $A$ is the cross-sectional area. The one-dimensional thermal resistance of a solid body can be assumed to be constant because the thermal conductivity of most solid bodies varies only little with temperature. The same can not be assumed for gases. The temperature dependence of the thermal conductivity of gases, including air, is appreciable. In Appendix B, a table is given with values of thermal conductivities for relevant materials in the test machines.

Thermal contact resistances between two adjacent surfaces are due to a thin isolating layer that can be air or oxide. In some cases, the contact pressure can be used to calculate the thermal contact resistance. In other cases, measurements are necessary to determine the thermal contact resistance. Examples of such layers in an electrical machine are between the stator winding and the stator core, and between lamination sheets in the core.

### Convection

Heat exchange due to convection is described by

$$q = \alpha(T_{\mathrm{w}} - T_{\infty}) \tag{24}$$

where $\alpha$ is the heat transfer coefficient and $T_{\mathrm{w}}$ and $T_{\infty}$ are the temperatures of the surface and the ambient cooling medium, respectively. Generally $\alpha$ depends on many variables, such as the shape and dimensions of the surface, flow characteristics, temperature and material characteristics of the fluid. Numerical values for $\alpha$ are in general determined from empirical relations involving dimensionless numbers such as the Reynolds number

$$Re = \frac{ux}{\nu} \tag{25}$$

where $u$ is the velocity of the coolant flow and $\nu$ is the kinematic viscosity. $x$ is a characteristic length, which sometimes is the diameter, in which case the symbol $Re_d$ is used. Reynolds number can be used as a measure of the regime of flow. Often a well defined value (critical Reynolds number) exists, where a transition from laminar to turbulent flow can be observed. For free convection, the Grashof number

$$Gr = \frac{g\beta\left(T_{\mathrm{w}} - T_{\infty}\right)x^3}{\nu^2} \tag{26}$$

is used instead of the Reynolds number, where $g$ is the acceleration of gravity, $\beta$ is the volume coefficient of expansion and $x$ is a characteristic length. Another dimensionless number is the Prandtl number

$$Pr = \frac{\nu\rho c}{\lambda_{\mathrm{f}}} \tag{27}$$

where $\lambda_{\mathrm{f}}$ is the thermal conductivity of the fluid. $Pr$ is coolant-characteristic. By including $Pr$ in an empirical formula for the heat transfer, the formula can be made valid for many kinds of fluids. The Nusselt number is a dimensionless number which is directly related to the heat transfer coefficient by

$$Nu = \frac{\alpha x}{\lambda_\mathrm{f}} \tag{28}$$

where $x$ is a characteristic length. When this length is a diameter, the symbol $Nu_d$ is used. The Nusselt number can in many flow cases be expressed as a function of the Reynolds number and the Prandtl number. The Nusselt number (and thus $\alpha$) is usually calculated by empirical formulas. Accurate formulas exist only for special cases with well defined geometries and flows. The thermal resistance due to convection is calculated from $\alpha$ by

$$R_\mathrm{th} = \frac{1}{\alpha A} \tag{29}$$

## Radiation

Net radiation that leaves a surface depends on area, material characteristics, temperature, and surroundings. The emissivity and the absorbtivity of a compact body are usually put equal and there is no transmission. Thus the heat exchange depends on radiation angles, emissivity and temperatures of the interacting surfaces. Sometimes the simplification can be made that the surroundings act as a blackbody, i.e. the absorbtivity is 1. The net radiation from a body to the surroundings can then be calculated by

$$q = \sigma\varepsilon\left(T_\mathrm{w}^4 - T_\infty^4\right) \tag{30}$$

where $T_\mathrm{w}$ and $T_\infty$ are the absolute temperatures of the body and the surroundings, respectively, $\sigma$ is Stefan-Boltzmann's constant and $\varepsilon$ is the emissivity of the body. In such a case, the thermal resistance to the surroundings is

$$R_\mathrm{th} = \frac{T_\mathrm{w} - T_\infty}{\sigma\varepsilon A\left(T_\mathrm{w}^4 - T_\infty^4\right)} \tag{31}$$

## 4.2 Thermal network theory

In a thermal network model, the object is divided into basic thermal elements, that are represented by a special node configuration (usually one node and some thermal resistances). The elements are linked together, forming a network of nodes and thermal resistances. The thermal network is similar to an electrical network consisting of current sources and resistances. For small induction motors, the ambient air temperature is usually taken as a thermal reference. The machine elements are represented by the temperature rise (i.e. the temperature difference between the element and the ambient air temperature). Let us assume that there are $n$ nodes, each of them being linked to the others through thermal resistances $R_{i,j}$, where $i$ and $j$ are the indices of the linked nodes. Let $R_{i,i}$ be the thermal resistance between node $i$ and the ambient. Then the steady-state nodal temperature rises are related by

$$P_i = \frac{\theta_i}{R_{i,i}} + \sum_{j=1}^{n} \frac{\theta_i - \theta_j}{R_{i,j}} \qquad i = 1,\ldots,n \tag{32}$$

where $\theta_1$ to $\theta_n$ are the temperature rises of each node and $P_1$ to $P_n$ are the losses of each node. A conductance matrix is usually defined

$$\mathbf{G} = \begin{bmatrix} \sum_{i=1}^{n} \frac{1}{R_{1,i}} & \frac{-1}{R_{1,2}} & \frac{-1}{R_{1,3}} & \cdots & \frac{-1}{R_{1,n}} \\ \frac{-1}{R_{2,1}} & \sum_{i=1}^{n} \frac{1}{R_{2,i}} & \frac{-1}{R_{2,3}} & \cdots & \frac{-1}{R_{2,n}} \\ \frac{-1}{R_{3,1}} & \frac{-1}{R_{3,2}} & \sum_{i=1}^{n} \frac{1}{R_{3,i}} & \cdots & \frac{-1}{R_{3,n}} \\ \cdots & \cdots & \cdots & \cdots & \cdots \\ \frac{-1}{R_{n,1}} & \frac{-1}{R_{n,2}} & \frac{-1}{R_{n,3}} & \cdots & \sum_{i=1}^{n} \frac{1}{R_{n,i}} \end{bmatrix} \tag{33}$$

which makes it possible to express the system of equations in matrix form.

The column vectors **P** and **Θ** are defined

$$\mathbf{P} = \begin{bmatrix} P_1 \\ P_2 \\ P_3 \\ \cdots \\ P_n \end{bmatrix} \tag{34}$$

$$\mathbf{\Theta} = \begin{bmatrix} \theta_1 \\ \theta_2 \\ \theta_3 \\ \cdots \\ \theta_n \end{bmatrix} \tag{35}$$

With these definitions, Eq. (32) becomes

$$\mathbf{P} = \mathbf{G\Theta} \tag{36}$$

$$\mathbf{\Theta} = \mathbf{G}^{-1}\mathbf{P} \tag{37}$$

The stationary solution is obtained directly from Eq. (37). However, some of the parameters in **G** and especially in **P** are temperature-dependent, so an iterative process should be used where the temperature-dependent parameters are updated until the error is sufficiently small.

## 4.3 Node configurations

A *node configuration* should be understood as the way a particular element is modelled by nodes and by thermal resistances to the surroundings. It is important that the node configuration is such that the average temperature of the element is obtained in one node. From this temperature, the maximum temperature can generally be calculated. The simplest node configuration is that for one-dimensional heat flow with no internal sources (Fig. 24). $R_0$ is the total thermal resistance of the element in the direction of the heat flow.

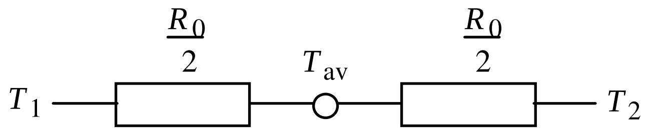

*Figure 24. Node configuration for one-dimensional heat flow without inner sources.*

Now suppose there is a uniform heat generation in the element. It is quite easily shown [5], that the two-node configuration in Fig. 25 then can be used to obtain the average temperature in the element. The internal losses $P_d$ of the element are then injected to the node that obtains the average temperature $T_{av}$.

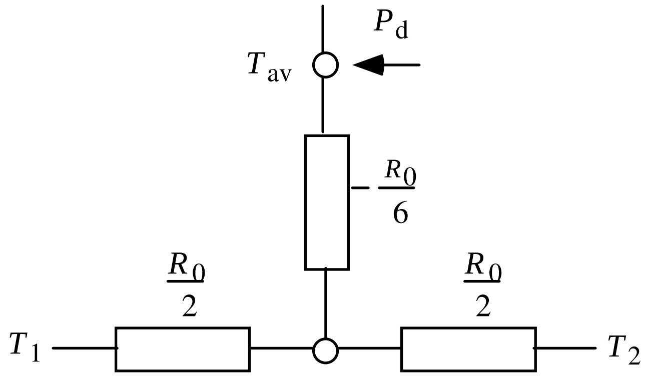

*Figure 25. Node configuration for one-dimensional flow with inner sources.*

If the maximum temperature of the element is not $T_1$ or $T_2$, it is given by

$$T_{max} = 1.5T_{av} - 0.25(T_1 + T_2) + \frac{(T_1 - T_2)^2}{12(2T_{av} - T_1 - T_2)} \tag{38}$$

This node configuration is suitable also when heat is uniformly added or subtracted along the element, e.g. due to convection. However, the element must then be sufficiently long, so that the principal heat flow is still one-dimensional. The disadvantage of this node configuration is that two nodes are needed instead of one.

For two-dimensional heat flow, the exact solution [27] is complex and can not easily be represented by a thermal network. However, as an approximate model, the node configurations of Figs 26 and 27 can be used.

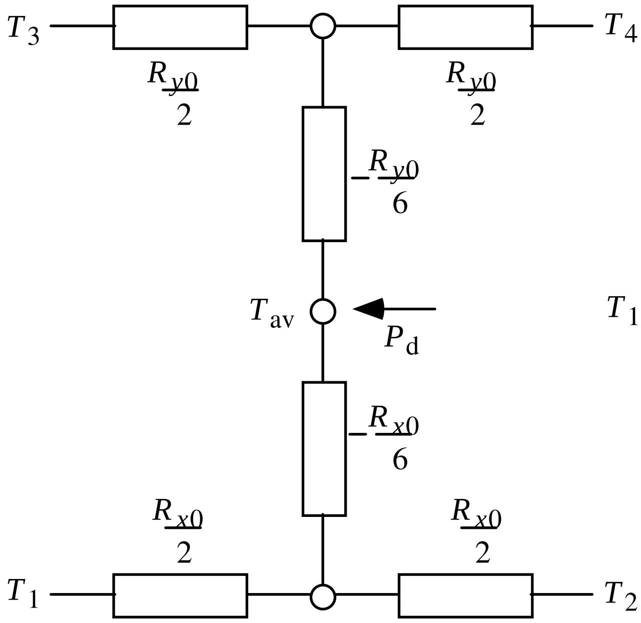

*Figure 26. Node configuration for two-dimensional flow with inner sources.*

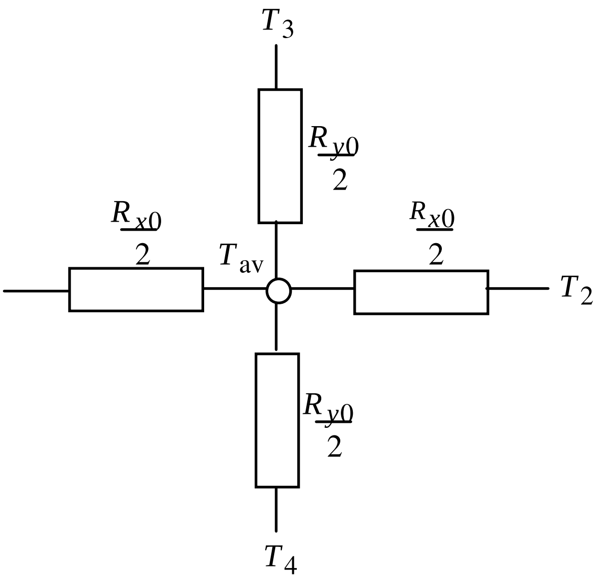

*Figure 27. Node configuration for two-dimensional flow with no inner sources.*

In Figs 26 and 27, $R_{x0}$ and $R_{y0}$ are the thermal resistances for one-dimensional flow in the $x$- and $y$-directions, respectively. The node configuration in Fig. 26 is simply obtained by connecting the node configurations of Fig. 25 in the $x$- and $y$-directions to the node they have in common. The three-dimensional case can be treated in the same way by connecting new branches accounting for the heat flow in the $z$-direction. This would then become a four-node configuration for the case with inner sources and a one-node configuration without inner sources.

## 4.4 A thermal model for TEFC induction motors

The suggested thermal network is primarily intended for design purposes. It is larger than most of the previously suggested models [1,5], which gives more detailed information of temperatures and heat flows. The developed model is shown in Fig. 28. It consists of 107 nodes and 170 thermal resistances. The network is based on experiences from measurements and simulations on the 15 kW enclosed induction motor, but it is suitable for any TEFC induction motor with cage rotor. With minor changes, the model can be used for wound rotors as well.

All peripheral temperature variations are neglected (except the temperature difference between the stator coil sides and the stator teeth). The symmetry makes it possible to divide the machine into elements that are concentric around the shaft. These elements are each divided into axial sections, which makes it possible to model the axial temperature variations within the machine. Thus the shaft, the rotor, the stator yoke and the frame are modelled as cylindrical shells or bodies. Since the stator teeth all are identical, they are treated as a number of parallel heat paths, which means that only one element is needed for each axial section of the stator teeth. The stator windings are treated similarly, with only one element for each axial section. The end shields are represented by one node and the bearings are each represented by three nodes. Furthermore, the internal air between the rotor and the end shields is represented by nodes. In total there are 96 elements (there are 107 nodes because the stator tooth elements are modelled by two-node configurations).

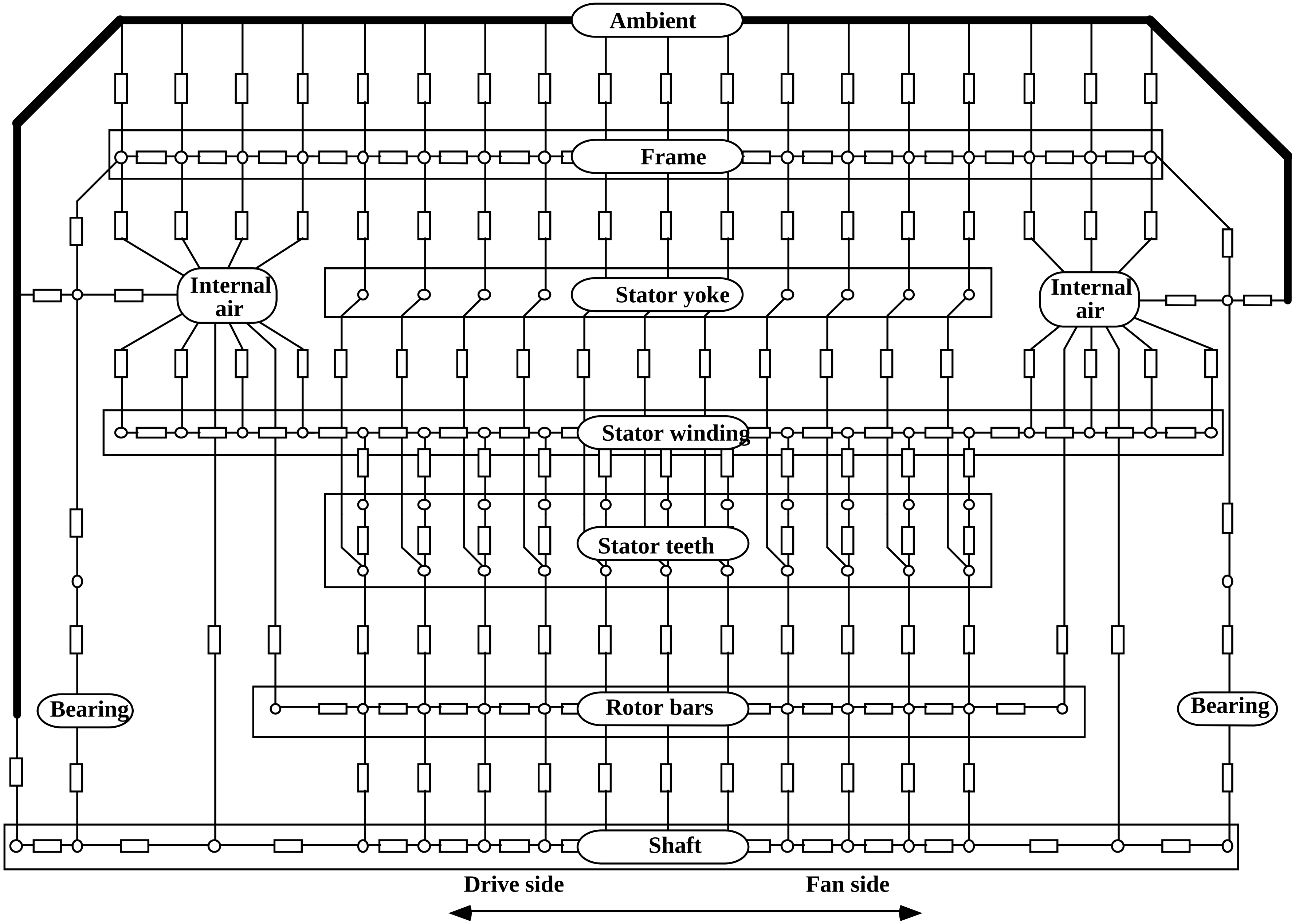
Ambient
Frame
Internal air
Stator yoke
Internal air
Stator winding
Stator teeth
Bearing
Rotor bars
Bearing
Shaft
Drive side
Fan side

*Figure 28. Thermal model with 96 elements.*

## 4.5 Identification of thermal resistances

Because there are thermal resistances that are difficult to calculate analytically, some thermal networks were developed to identify unknown thermal resistances using steady-state temperature and loss measurements. Some of the measured temperatures serve as boundary conditions, $T_j$, which are related to the nodal temperatures $T_k$ by

$$P_k = \sum_{i=1}^{n} \frac{T_k - T_i}{R_{1,i}} + \sum_{j=n+1}^{m} \frac{T_k - T_j}{R_{1,j}} \qquad k = 1 \ldots n \tag{39}$$

The identification process relies on measurements of some key temperatures among $T_k$. The identification is made by adapting the unknown thermal resistances so that the measured and calculated values of $T_k$ are equal. The method works best when only one variable is unknown. The identification models that were used are shown in Figs 31, 61 and 67, and are further described in the appropriate sections. Black dots represent boundary conditions and grey rectangles represent thermal resistances to be identified. Unfilled rectangles represent known thermal resistances.

# 5 Models of the machine parts

## 5.1 Rotor

When modelling aluminium cage rotors, the following assumptions are made: Axial heat flux in the rotor core is neglected. Thermal contact resistance between the rotor bars and the core is also neglected. This assumption is supported by measurements in [28], where it can be seen that the temperature drop between the bars and the core is very small. The rotor bar losses are assumed to be evenly distributed along the rotor. However, the end ring losses must be separately calculated. The rotor yoke is assumed to be lossless.

### 5.1.1 Internal modelling

The low thermal resistance between the bars and the core makes it possible to represent them both with one element. The rotor surface losses are thus added to the bar losses and the thermal capacity of the core to that of the bars. Such an element is in thermal contact with the stator teeth (through the air gap), the shaft and with other rotor elements in the axial direction. The thermal resistance between two rotor elements is:

$$R_{\mathrm{th}} = \frac{\ell}{Q_{\mathrm{r}} A \lambda} \tag{40}$$

where $\ell$ is the distance between adjacent rotor elements, $Q_{\mathrm{r}}$ is the number of bars, $\lambda$ is the heat conductivity of the bar material and $A$ is the cross-sectional area of a bar. The thermal resistance between a rotor element and a shaft element is partly due to the thermal resistance through the rotor core and partly due to a thermal contact resistance at the junction. The thermal resistance through the rotor core is given by:

$$R_{\mathrm{th}} = \frac{\ln r_2 - \ln r_1}{2\pi\lambda\ell} \tag{41}$$

where $r_2$ is the radius to the bottom of the rotor slots, $r_1$ is the shaft radius and $\lambda$ is the thermal conductivity of the core material. It is suggested that the thermal contact resistance is assumed to be of the same order of magnitude as that given by Eq. (41), since comparisons between measured shaft and rotor temperatures seemed to imply this for the 15 kW-motor.

### 5.1.2 Thermal resistance of the air gap

The heat flow in the air gap includes conduction, convection and radiation (radiation being a small part though). The heat flow in the air gap between concentric cylinders has been investigated by Becker and Kaye [29], Gazley [30], and others [31,32]. Only Gazley used real electrical machine parts with a normal air gap, the others used large air gaps and smooth surfaces both of the rotor and the stator. Most smaller TEFC motors have no axial air flow in the air gap. Without axial air flow, the flow is laminar at low speeds, but at a relatively high speed, a transition to turbulent flow begins. In the ideal laminar mode, there is no radial velocity component of the air, so heat can only be transported by conduction and radiation from the rotor to the stator. In the turbulent mode, vortices appear that make convection become an important factor. The mode is characterized by a Taylor number or modified Taylor number. The modified Taylor number used by Becker and Kaye is

$$(Ta)_{\mathrm{m}} = \frac{\omega^2 r_\delta \delta^3}{\nu^2 F_{\mathrm{g}}} \tag{42}$$

where $\omega$ is the angular speed, $r_\delta$ is the average air gap radius and $F_{\mathrm{g}}$ can be put to 1 for all practical cases. Becker and Kaye [29] indicate the critical modified Taylor number to 1740. Their data are shown in Fig. 29. At Taylor numbers higher than 1740, they give the empirical formula

$$Nu = 0.409\,(Ta)_{\mathrm{m}}^{0.241} - 137\,(Ta)_{\mathrm{m}}^{-0.75} \tag{43}$$

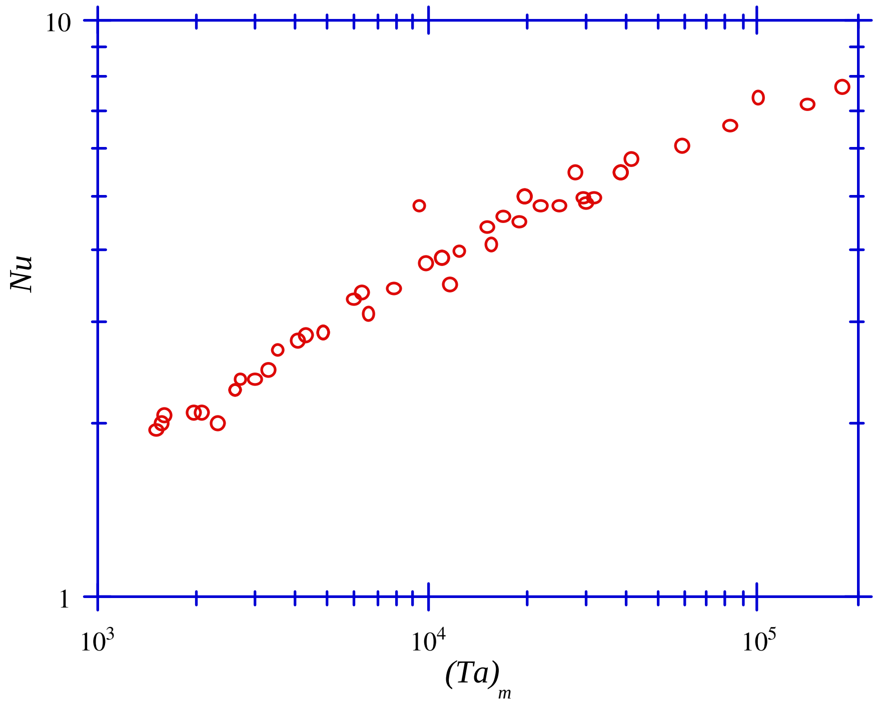

*Figure 29. Becker's and Kaye's data for smooth rotor and stator surfaces*

With no axial air flow, $\alpha$ is usually defined as the heat transfer coefficient between the rotor and the stator rather than between the rotor and the fluid. Since the air gap is the characteristic length, this means that the relation between $\alpha$ and $Nu$ is

$$\alpha = \frac{Nu\,\lambda_\mathrm{f}}{2\delta} \tag{44}$$

$\alpha$ represents in this case both conduction and convection in the air gap. At laminar air flow, i.e. $(Ta)_\mathrm{m}<1740$, $Nu$ has the value 2. This is also the measured value of $Nu$ in [29,31,32]. Gazley's [30] result, however, is higher. His data are never-theless interesting since they are the only ones measured with a realistic air gap and with slots in the stator, as would be expected in a real machine. His data are shown in Fig. 30. If the data for the slotted surfaces are compared with those for the smooth surfaces, it can be seen that the heat conduction decreases because of the slots. However, a convective heat transfer component is also added which increases with the Taylor number. Since Gazley's data have not yet been confirmed by any similar investigation, we have chosen to neglect both these effects of the slotting, since they work against each other. For smooth surfaces, Gazley measured $Nu$=2.5 for laminar flow. In this work however, $Nu$=2 is used as [29,31,32] suggest.

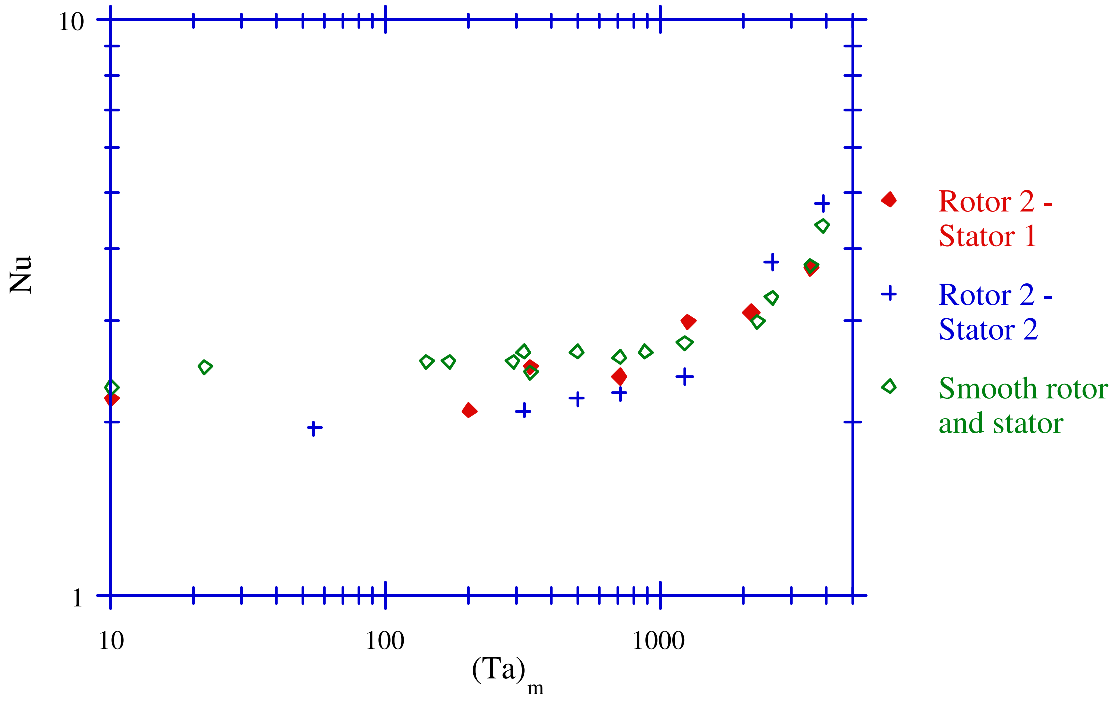

*Figure 30. Gazley's data for slotted rotors and stators. The data have been related to the Taylor number instead of the Reynolds number.*

Since both $\lambda$ and $\nu$ are temperature-dependent, it is suggested that they are evaluated for the average air gap temperature. Furthermore, the thermal expansion of the rotor and the stator makes $\delta$ temperature-dependent. The temperature dependence can be accounted for by

$$\delta = \delta_0 - \kappa_{\mathrm{Fe}} r_\delta \Delta T \tag{45}$$

where $\delta_0$ is the air gap without thermal expansion. When $\alpha$ has been calculated, the thermal resistance due to conductive and convective heat transfer can be determined. The thermal resistance between a rotor element and a stator teeth element is

$$R_{\mathrm{th}\,1} = \frac{1}{2\,\pi r_\delta \ell \alpha} \tag{46}$$

where $\ell$ is the axial length of the elements. Eq. (46) does not include radiation.

The emissivity of the rotor and stator surfaces was measured approximately by heating them to 70 °C and comparing their temperatures with the readings of an infra-red measuring device. The result was that the emissivity of the lacquered stator surface was $\varepsilon_s \approx 0.95$ while the emissivity of the lathed rotor surface was $\varepsilon_r \approx 0.13$. For such a low emissivity, the heat radiation is very small for normal induction motors. The radiation heat flux is given by

$$q = \frac{\sigma(T_r^4 - T_s^4)}{\frac{1}{\varepsilon_r} + \frac{1}{\varepsilon_s} - 1} \tag{47}$$

In Eq. (47), $T$ is the absolute temperature. Indices r and s stand for the rotor and the stator, respectively.

### 5.1.3 Heat transfer from the end rings

The rotor fins provide a heat path from the rotor end rings to the internal air. The amount of heat transferred from the rotor to the internal air can be described by a heat transfer coefficient, that is a function of the rotor peripheral speed and the geometry of the rotor ends. Kotrba [33] suggests that

$$\alpha = k u_r^{0.65} \tag{48}$$

where $k$=16.5 W(s/m)$^{0.65}$/m$^2$K and $u_r$ is the peripheral speed of the rotor. The area associated with the heat transfer coefficient is calculated by

$$A = 2\,bhn + \pi r_\delta^2 \tag{49}$$

where $b$ and $h$ are the length and height of the rotor fins, respectively, and $n$ is the number of fins. This choice of area definition gives larger weight to the latter term than to the actual fin area, which can be criticized since no doubt the heat transfer coefficient of the fins is greater than that of the rings and core ends. In order to check the validity of Eq. (48) for the test motors, an identification model was used to find the values of the heat transfer coefficient.

#### Identification model for the heat transfer from the rotor end rings

The identification model is shown in Fig. 31. There are three values of thermal resistances that can not be easily calculated. These are $R_a$, $R_b$ and $R_c$, which are represented as greyshaded rectangles. $R_a$ is the thermal resistance between a stator end-winding node and internal air. $R_b$ is the thermal resistance between a stator coil side node and a stator teeth node. $R_c$ is the thermal resistance between a rotor end ring and internal air. The other thermal resistances are represented by unfilled rectangles and can be calculated individually. The black dots represent the boundary conditions. In order to identify $R_c$, the rotor surface temperature must be measured, as well as the boundary temperatures. The calculated rotor temperature is insensitive for variations in $R_a$ and $R_b$, so these values can be approximative. There must be a significant temperature difference between the rotor and the stator, so it is best to perform the experiment at rated load.

It is assumed that the total rotor losses, including additional losses, can be either calculated, or else evaluated from measurements. The rotor losses are assumed to be evenly distributed along the rotor, except for the end ring losses, which are calculated according to Eq. (5). $R_c$ is identified as the value that makes measured and calculated rotor temperatures equal. The identification primarily relies on the accuracy of the rotor loss calculation and the accuracy of the value of the thermal resistance of the air gap.

If the end ring losses are small, the axial temperature variation along the rotor tends to be large; in such a case, the measured and calculated rotor temperature *variations* can also be compared as a check on the plausibility of the identified value. This is possible by measuring at least 5 equally spaced rotor temperatures, two of which should be the end ring temperatures.

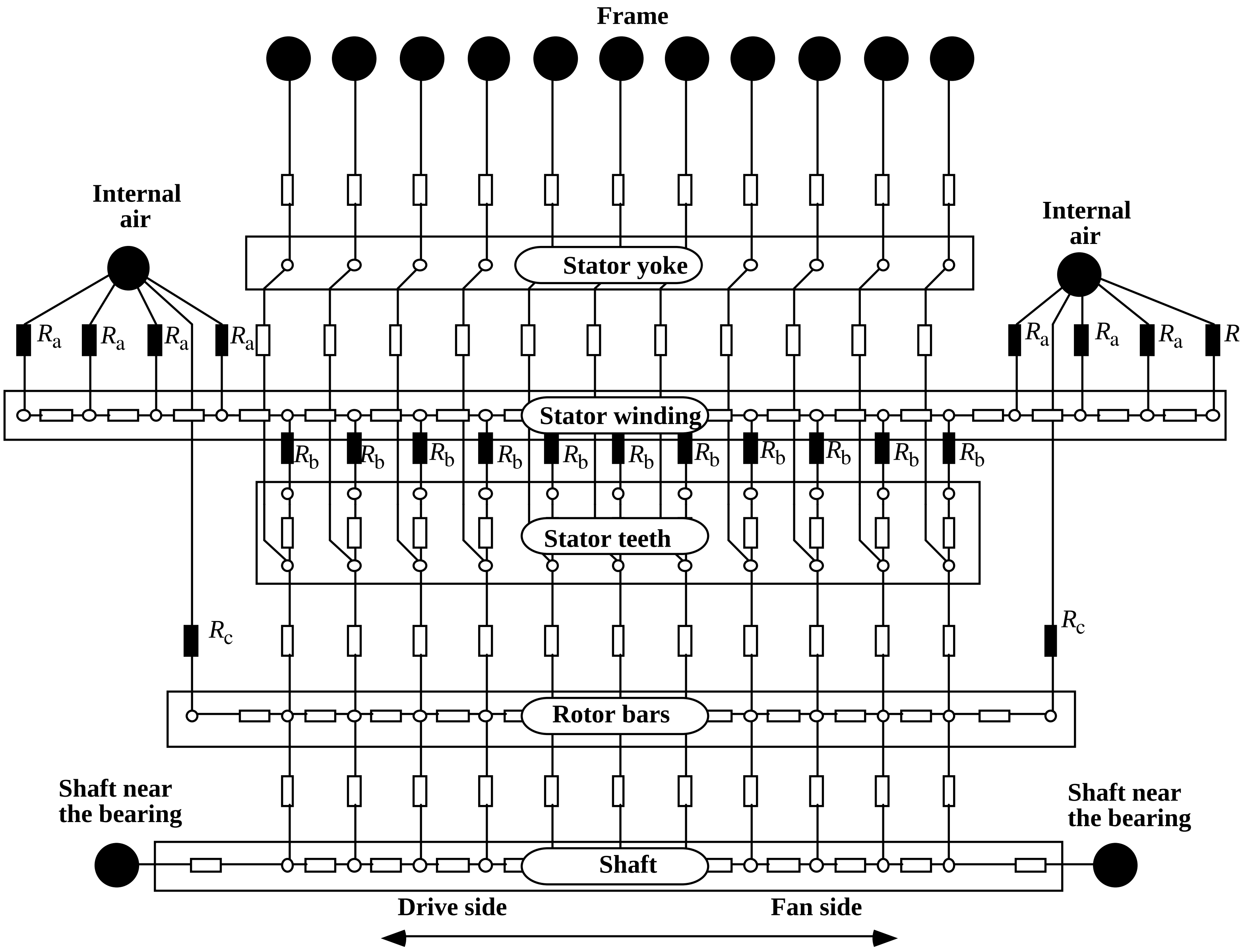
Frame
Internal air
Internal air
Stator yoke
$R_a$
$R_a$
$R_a$
$R_a$
$R_a$
$R_a$
$R_a$
$R_a$
Stator winding
$R_b$
$R_b$
$R_b$
$R_b$
$R_b$
$R_b$
$R_b$
$R_b$
$R_b$
$R_b$
$R_b$
Stator teeth
$R_c$
$R_c$
Rotor bars
Shaft near the bearing
Shaft near the bearing
Shaft
Drive side
Fan side

*Figure 31. Model for identification of the thermal resistances $R_a$, $R_b$ and $R_c$.*

The result of the identification is shown in Fig. 32 together with the relation suggested by Kotrba. Basically, the validity of Eq. (48) seems to be confirmed by the identification results.

The identification result for the 15 kW motor is probably more reliable than that of the 4 kW motor, because the temperature difference between the rotor and the internal air was larger, the percentage of rotor losses was larger and the fins were larger, which made the heat flow from the fins appreciable. A 1 °C temperature measurement error would cause a 5 % error in the identified value and a 5 % error in the rotor losses would cause a 12 % error in the identified value at rated load. A possible explanation of why the identification results for the 4 kW motor are lower than those for the 15 kW motor can also be that the fin area of the 4 kW motor is a smaller percentage of the total area given by Eq. (49).

The axial temperature variation was substantial for the 15 kW motor but very small for the 4 kW motor. In Figs. 33–38, the calculated and measured rotor temperatures of the 15 kW motor are shown for some different speeds. The fact that the calculated temperatures do not exactly match the measured data points can be explained if the rotor losses are not evenly distributed, which would be the case if the losses due to interbar currents are large.

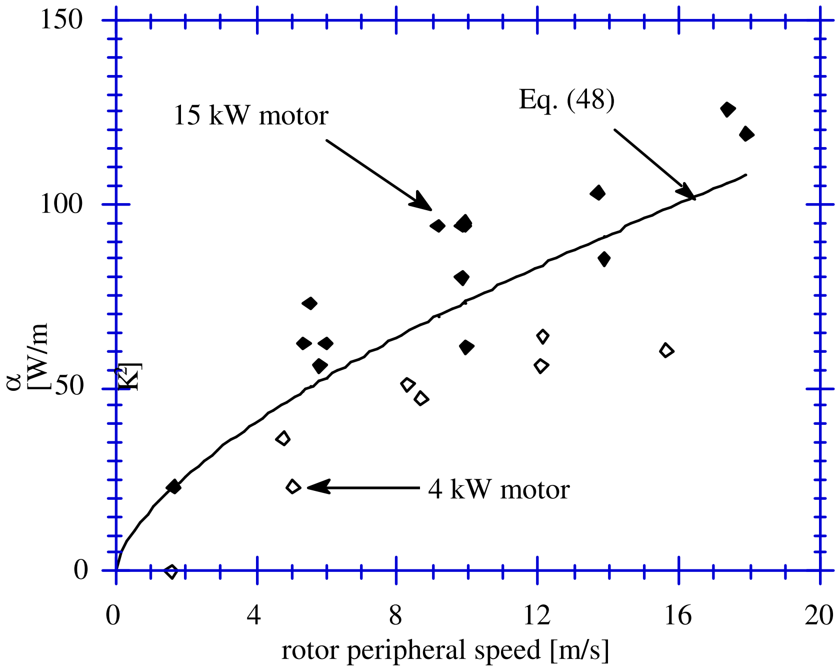

*Figure 32. Identification of the heat transfer coefficient of the rotor end rings.*

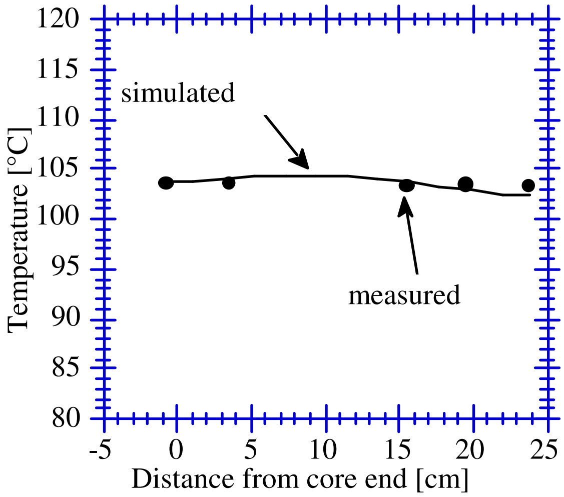

*Figure 33. Rotor temperatures at standstill, locked rotor test.*

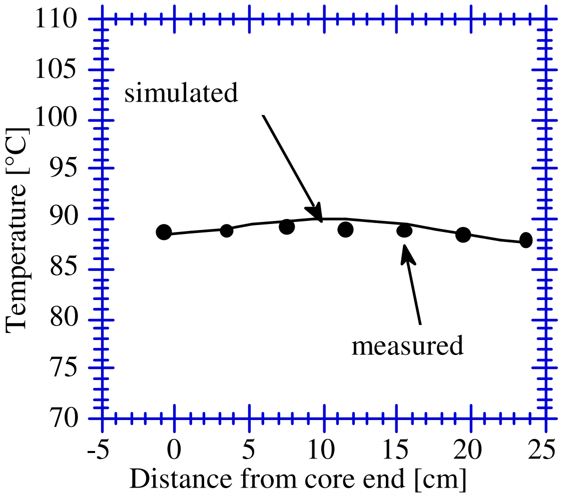

*Figure 34. Rotor temperatures at 167 rpm, 67 % of rated torque.*

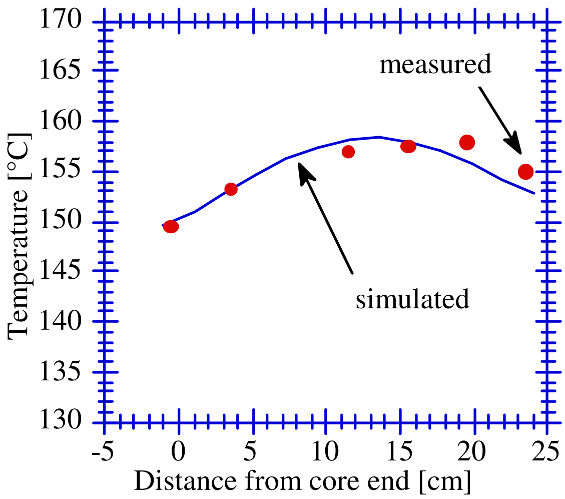

*Figure 35. Rotor temperatures at 530 rpm, rated torque.*

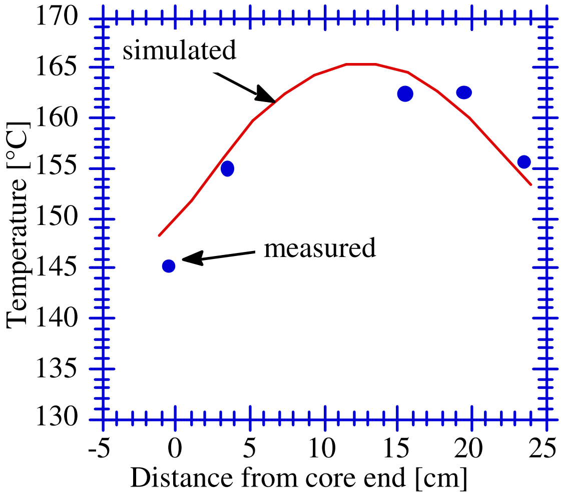

*Figure 36. Rotor temperatures at 998 rpm, rated torque.*

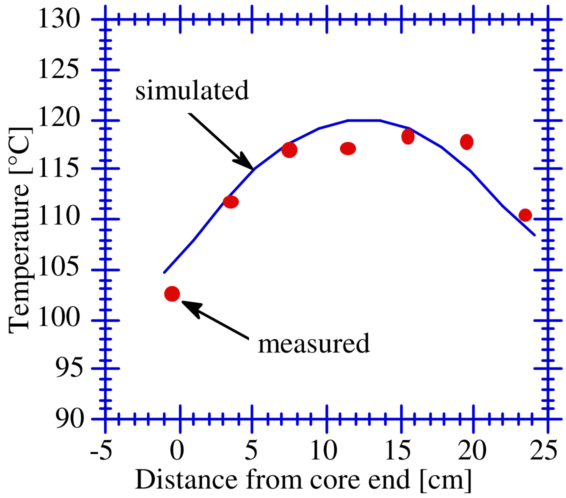

*Figure 37. Rotor temperatures at 1376 rpm, 67 % of rated torque.*

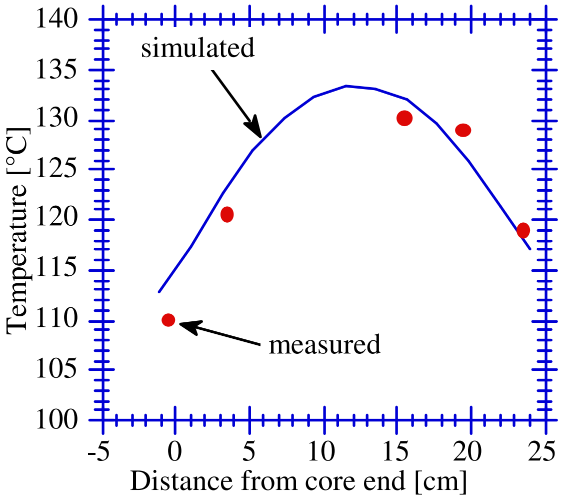

*Figure 38. Rotor temperatures at 1746 rpm, 67 % of rated torque.*

## 5.2 Shaft

The shaft is treated as a cylinder with an isothermal cross-section. The shaft diameter varies along its length: it is smaller on the outside of the machine. The thermal resistance between two shaft elements is:

$$R_{\mathrm{th}} = \frac{\ell}{\pi r^2 \lambda} \tag{50}$$

where $r$ is the shaft radius and $\lambda$ the thermal conductivity of the shaft material. Heat enters the shaft from the rotor and goes to the bearings, to the internal air and to the ambient air. The shaft can be modelled by dividing it into a number of elements that are connected to the rotor: 2 elements that are connected to the internal air (one at each side of the rotor), 2 elements that are connected to the bearings and one element that is connected to the ambient air.

The heat transfer between a rotating cylinder and air has been investigated by Etemad [34], who measured the Nusselt numbers for a range of Reynolds numbers from 0 to 65400. The suggested empirical correlation is

$$Nu_d = 0.076\, Re_d^{0.7} \tag{51}$$

where $Re_d$ is calculated using the diameter and the peripheral velocity of the shaft. It is suggested that Eq. (51) is used to calculate the thermal resistances from the shaft to the internal and external air. Of course, the external part of the shaft is also in thermal contact with a mechanical coupling. The coupling and the load have a certain influence on the drive side bearing temperature and should be treated from case to case.

## 5.3 Stator winding

Since the windings are the machine parts that are most likely to be damaged by excessive heating, their modelling is important. All coils in the machine are assumed to have the same temperature distribution, so that they can be treated as being in parallel with each other. In the axial direction, the windings are modelled by a number of nodes connected in series, each one representing the average temperature of a winding element. In the transverse direction, the coil sides are connected to the stator core and the end windings are connected to the internal air.

### 5.3.1 Coil sides

The thermal resistance between two adjacent winding nodes is obtained by

$$R_{\mathrm{th}} = \frac{\ell}{Q_{\mathrm{s}} A_{\mathrm{Cu}} \lambda} \tag{52}$$

where $Q_{\mathrm{s}}$ is the number of stator slots, $\ell$ the length between nodes and $A_{\mathrm{Cu}}$ the total copper area in one slot. Axial conduction in the insulating material is neglected because of its low value of thermal conductivity.

The transverse heat flow is rather difficult to model. Not only must the average winding temperature be obtained, but also the maximum temperature, since it is the maximum temperature that effects the rate of ageing. In the embedded windings, the generated heat must pass through impregnation material, slot insulation and air pockets before it reaches the stator core. The heat exchange between the slots and the rotor is probably small. Since the exact geometrical configuration of air, copper and insulation material is unknown, some simplifications are introduced: The slot material, consisting of copper wires and impregnation, is considered as a homogeneous body with uniform heat generation. Assuming there are no air pockets inside the slot insulation, the thermal conductivity can be calculated by the finite element method [10]. The thermal conductivity is a function of the percentage of metal in the insulated slot area, see Fig. 39.

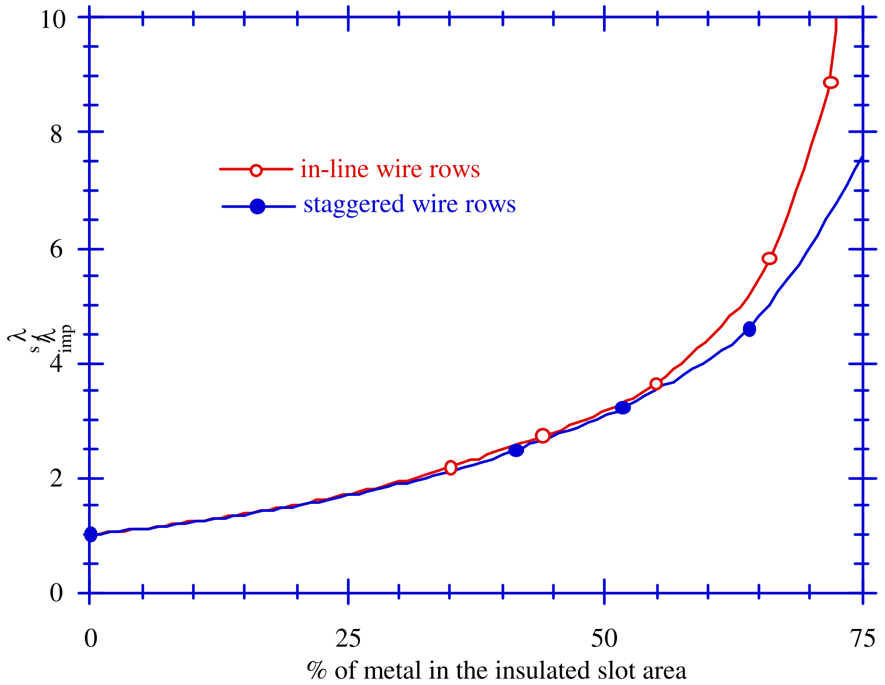

*Figure 39. Thermal conductivity of the slot material,* $\lambda_s$*, expressed as its ratio to the thermal conductivity of the impregnation material,* $\lambda_{imp}$*. The value depends on the percentage of metal area in the slot and the orientation of the wires in the slot.*

The slot insulation and the air pockets are modelled by a layer that surrounds the slot material. The thickness $d$ of this layer should be equal to the sum of the slot insulation thickness $d_i$ and the equivalent air film thickness $d_a$. In fact, the thermal resistance of the slot insulation is much smaller than that of the equivalent air film. The assumption that all air pockets are located outside the slot insulation can be disputed. The penetration of the impregnation resin depends on manufacturing techniques. A visual inspection of the end windings of the 4 kW machine showed a solid penetration at the drive side, but at the fan side the penetration was not complete, probably because the fan side was turned upwards during the hardening process. Better technique, like vacuum impregnation, can reduce air pockets both in the coils and between the slot insulation and the core. Some examples of how air pockets can be formed between the slot insulation and the stator core are shown in Fig. 40.

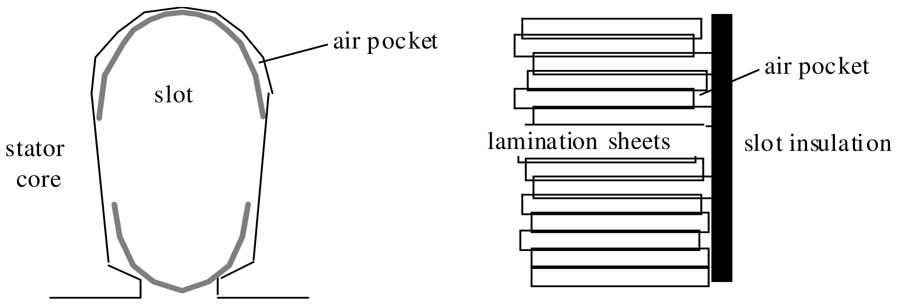
air pocket
slot
stator core
air pocket
lamination sheets
slot insulation

*Figure 40. Air pockets between the stator core and the slot insulation.*

One possibility to obtain values for the average and maximum slot temperatures is to use an equivalent rectangular slot shape. Soderberg [27] derived expressions for the average and maximum temperatures of a rectangular element assuming a constant boundary temperature and a thermal surface resistance. There is an exact solution of this problem, but it has a complex mathematical form and can not easily be represented by a thermal resistive network. Soderbergs expressions are good approximations and can be represented by equivalent thermal resistances. In Fig. 41 the fictive slot shape is shown together with a suggestion of how to transform the original slot shape into the rectangular slot shape.

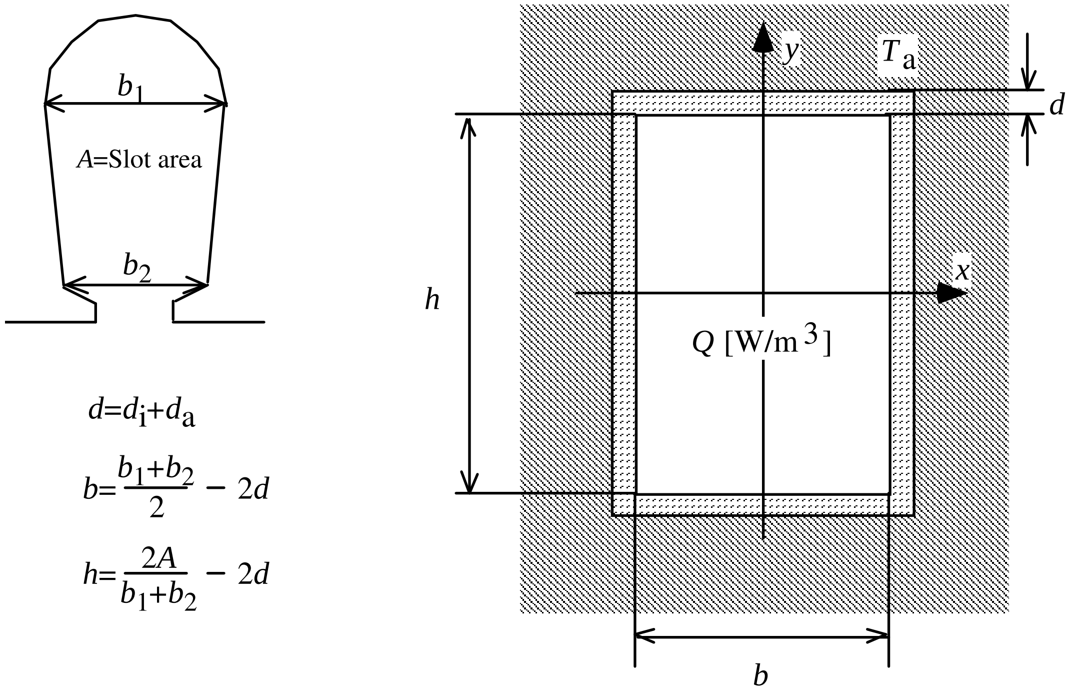
$b_1$
$A$=Slot area
$b_2$
$d=d_i+d_a$
$b=\frac{b_1+b_2}{2}-2d$
$h=\frac{2A}{b_1+b_2}-2d$
$y$
$T_a$
$d$
$h$
$x$
$Q$ [W/m$^3$]
$b$

*Figure 41. Transformation of the original slot shape into a rectangular slot shape. $T_a$, the boundary temperature, is assumed to be uniform and equal to the average stator tooth temperature.*

The one-dimensional thermal resistances of the slot material per unit length are

$$R_{x0} = \frac{b}{h\lambda_\mathrm{s}} \tag{53}$$

$$R_{y0} = \frac{h}{b\lambda_\mathrm{s}} \tag{54}$$

where $\lambda_\mathrm{s}$ is the thermal conductivity of the slot material. The one-dimensional thermal resistances resulting from the slot insulation and the air film per unit length are

$$R_{\mathrm{i}x} = \frac{d_\mathrm{i}}{h\lambda_\mathrm{i}} + \frac{d_\mathrm{a}}{h\lambda_\mathrm{a}} \tag{55}$$

$$R_{\mathrm{i}y} = \frac{d_\mathrm{i}}{b\lambda_\mathrm{i}} + \frac{d_\mathrm{a}}{b\lambda_\mathrm{a}} \tag{56}$$

where $\lambda_\mathrm{i}$ and $\lambda_\mathrm{a}$ are the thermal conductivities of the slot insulation and the air film, respectively. $d_\mathrm{i}$, if not given by the manufacturer, can be measured. By rearranging Soderbergs original expressions the following is obtained

$$T_\mathrm{av} = T_\mathrm{a} + Qbh\,\frac{R_x R_y}{R_x + R_y}\left(1 - \frac{R_{x0}R_{y0}}{720\,R_x R_y}\right) \tag{57}$$

$$T_\mathrm{max} = T_\mathrm{a} + (T_\mathrm{av} - T_\mathrm{a})\frac{(R_{ix} + 0.25R_{x0})(R_{\mathrm{i}y} + 0.25R_{y0})}{4R_x R_y}\left(1 - \frac{R_{x0}R_{y0}}{384\,R_x R_y}\right) \tag{58}$$

where $T_\mathrm{av}$ and $T_\mathrm{max}$ are the average and maximum temperatures, and $R_x$ and $R_y$ are given by

$$R_x = 0.5\left(R_{\mathrm{i}x} + \frac{R_{x0}}{6}\right) \tag{59}$$

$$R_y = 0.5\left(R_{\mathrm{i}y} + \frac{R_{y0}}{6}\right) \tag{60}$$

The above values are all per unit length. Most of the heat flows to the stator teeth, only a minor part flows to the stator yoke, since $R_y >> R_x$ in general. Because of this, $T_a$ corresponds to the average stator tooth temperature. The equivalent thermal resistance between a coil side node and a stator tooth node is

$$R_{\mathrm{th}} = \frac{R_x R_y}{Q_{\mathrm{s}} \ell (R_x + R_y)} \left(1 - \frac{R_{x0} R_{y0}}{720 R_x R_y}\right) \tag{61}$$

where $Q_s$ is the number of slots and $\ell$ the distance between two adjacent coil side nodes. Eq. (61) can be used to calculate the thermal resistance between the stator windings and the stator teeth, but necessitates the knowledge of the thickness $d_a$ of the equivalent air film, which is not directly measurable. Because of this, an identification model has been used to provide some values of $d_a$.

### Identification of the thermal resistance between the coil sides and the stator teeth

The best way of heating the stator windings is by a DC current, because then all other machine parts are lossless, and the stator winding temperature is easily measured by the resistance method. The identification model mentioned earlier (Fig. 31) is used. The heat run must be made at standstill, because then the convective and radiative heat flow from the end windings is quite small, and can be calculated and deducted using the theory presented in Section 5.3.2. Alternatively, the machine can be filled with isolating and reflective material in such a way that no heat can leave the end windings. By doing so, the value $R_a$ in Fig. 31 can be given a very high value. The value of $R_c$ in Fig. 31 can be approximated.

Applying a guessed value of the unknown thermal resistance $R_b$, the average temperature of the stator windings is calculated. This temperature is compared with the measured temperature, obtained by the resistance method, and $R_b$ is changed until the calculated and measured temperatures are equal.

It is probable that the thermal resistance between the stator windings and the stator teeth is slightly temperature-dependent, because of air pockets and thermal expansion. Temperature dependence is not included in the model, but it can be included by using the temperature dependence of $\lambda_a$ in Eqs (55) and (56). By inserting the identified values into Eq. (61), it was found that the equivalent air layer thickness associated with the winding insulation was $d_a$=0.17 mm for the 4 kW machine and $d_a$=0.30 mm for the 15 kW machine using $\lambda_a$=0.03 W/m·K.
Using these values for unknown, but similar machines is somewhat risky, but

probably better than no value at all. Figure 42 shows the results for the 4 kW machine. Each data point corresponds to a different DC current. For the 15 kW machine, only one such test was performed, which resulted in a value of $R_{\mathrm{th}}$ of 0.38 K/W. Figures 43–44 show the simulated and measured stator winding temperature at rated current for the two test machines. The measured end-winding temperatures are also shown, but they are not used for identification purposes since they obviously are lower than the average end-winding temperatures.

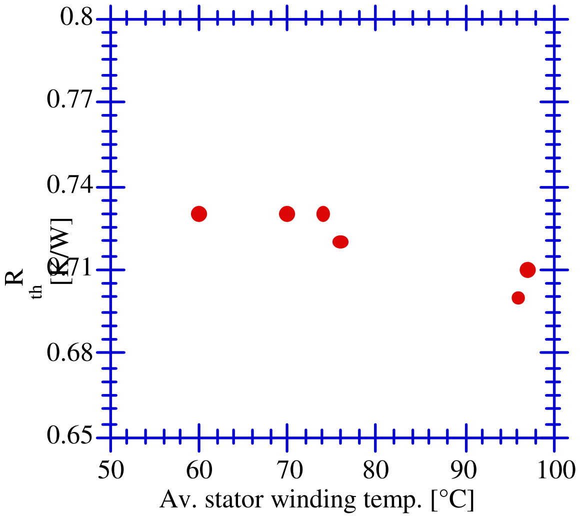

*Figure 42. 4 kW motor: Identified thermal resistances between the stator windings and the stator teeth*

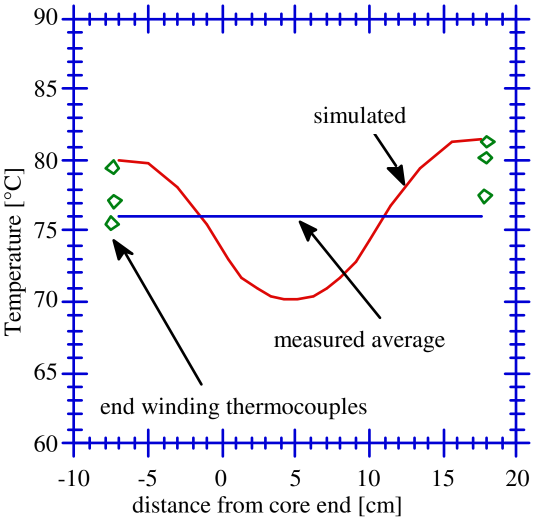

*Figure 43. 4 kW motor: Simulated stator winding temperature with injected DC current at standstill.*

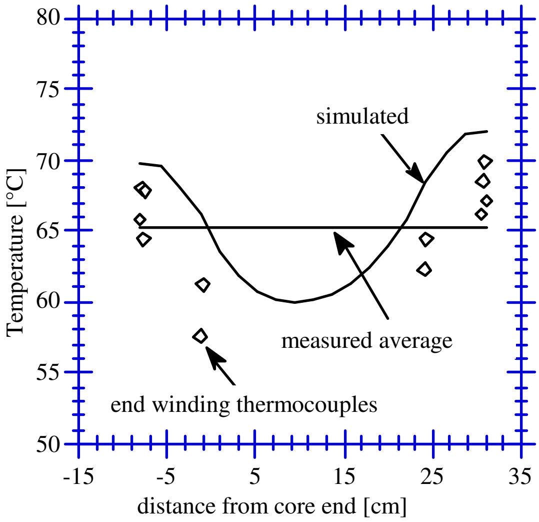

*Figure 44. 15 kW motor: Simulated stator winding temperature with injected DC current at standstill.*

### 5.3.2 End windings

The heat transfer from the end windings is mostly due to convection although some radiation also exists. Figures 45 and 46 show how the air circulates due to free convection at standstill and due to forced convection at normal speed.

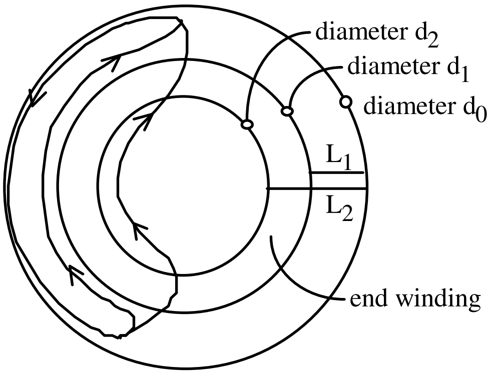

*Figure 45. Air flow at standstill.*

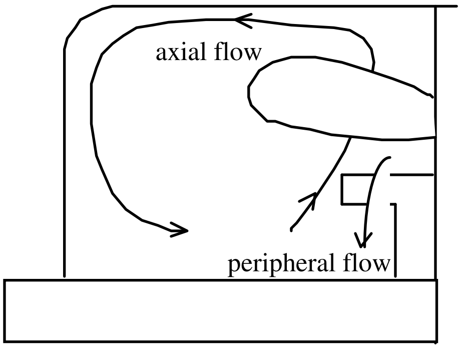

*Figure 46. Air flow for a rotating machine.*

When the machine is running, the air circulates as shown in Fig. 46. The air is accelerated by the rotor fins, passes through the holes in the end winding, and is cooled by the end shield on its way back to the rotor fins. If the passages through the end windings are very small, the axial air flow is obstructed, which can result in poor cooling of the end windings. Unfortunately, there are very few references concerning heat transfer from end windings of enclosed electrical machines. Luke [35] made some measurements of the heat transfer coefficient of a specially built rotor winding. However, his apparatus was not very similar to a modern TEFC motor. Koziej [36] gives some formulas for the external and internal surfaces of the end winding. According to him, the heat transfer coefficient is proportional to the 0.6 power of speed. In order to compare different results, the same definition of the end winding area must be used. Luke defines it as

$$A = \pi \ell_{\mathrm{ov}} \frac{(d_1 + d_2)}{2} \tag{62}$$

where $\ell_{\mathrm{ov}}$ is the average conductor length of the winding overhangs and $d_1$ and $d_2$ are given in Fig. 45. This definition of the area is used hereafter.

At standstill, the heat transfer is quite small and consists of radiation and free convection. The net radiation heat is approximated as

$$P = 0.5 A\sigma\varepsilon\left(T_{\mathrm{w}}^4 - T_{\infty}^4\right) \tag{63}$$

where $T_{\mathrm{w}}$ and $T_{\infty}$ in this case are the absolute temperatures of the end winding and the end shield, respectively. The factor 0.5 accounts for the fact that only the outside of the end winding faces the end shield. Assuming there is a layer of paint or varnish on the end shield, the value $\varepsilon$=0.9 can be used.

The effect of free convection can be determined by using a formula for free convection between concentric cylinders [37]. Assuming that the inner and outer air streams, shown in Fig. 45, follow the same law, the convection heat flow at standstill becomes

$$P = \frac{0.386\, \pi \ell_{\mathrm{ov}} (T_{\mathrm{w}} - T_{\infty}) \lambda_{\mathrm{a}} \sqrt{Pr}}{(0.861 + Pr)^{0.25}} \left( \frac{Gr_{L_1}^{0.25}}{L_1^{0.75} (d_1^{-0.6} + d_0^{-0.6})^{1.25}} + \frac{Gr_{L_2}^{0.25}}{L_2^{0.75} (d_2^{-0.6} + d_0^{-0.6})^{1.25}} \right) \tag{64}$$

where $T_{\mathrm{w}}$ and $T_{\infty}$ in this case are the temperatures of the end winding and the end shield, respectively. $Gr$ is calculated using $T_{\mathrm{w}}$, $T_{\infty}$ and using $L_1$ or $L_2$ as characteristic length. The distances $d_0$, $d_1$, $d_2$, $L_1$ and $L_2$ are given in Fig. 45.

To get some data of the heat transfer coefficient of the end windings, an identification model has been used.

## Identification of the thermal resistance between the stator end windings and the internal air

Before the identification of the thermal resistance between the stator end windings and the internal air, the thermal resistance between the coil sides and the stator teeth must already be known. The identification model mentioned earlier (Fig. 31) is used. The average temperature of the stator windings is measured by the resistance method, and $R_{\mathrm{a}}$ is identified as the value that makes calculated and measured average stator winding temperatures equal. The results of the identification in the form of a heat transfer coefficient are shown together with Luke's data in Figs 47 and 48.

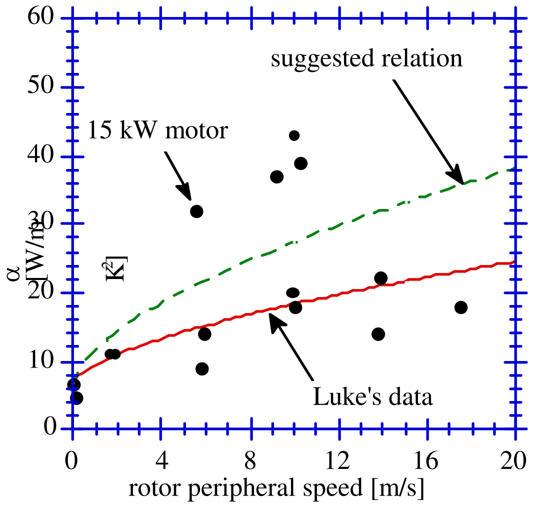

*Figure 47. Heat transfer coefficient between the end windings and the internal air.*

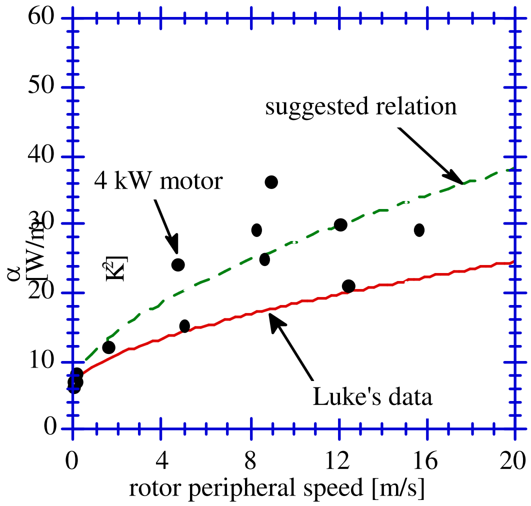

*Figure 48. Heat transfer coefficient between the end windings and the internal air.*

Each data point in Figs 47 and 48 corresponds to a test with a different load and speed. Unfortunately, the identification did not produce equal results for equal speeds; high loads usually resulted in higher $\alpha$. There are some sources of error in the identification that can explain the scatter; A 1 °C measurement error of the frame temperature or of the stator winding temperature can result in a 20 % error, and a 1 °C measurement error of the internal air temperature can result in a 5 % error for a test with rated current. At partial load the errors would be even larger. The temperature dependence of the thermal resistance between the coil sides and the stator teeth, and also the influence of heat entering the stator slots from the rotor, were neglected, and can cause errors. It is suggested that the following formula is used to calculate the heat transfer coefficient of the end windings

$$\alpha = k_1 + k_2 u_r^{0.6} \tag{65}$$

where $k_1$=6.5 W/m$^2$K and $k_2$=5.25 W(s/m)$^{0.6}$/m$^2$K. The effect of radiation is included in the expression for α, and need not be described by an additional thermal resistance from the end winding to the end shield. Equation (65) gives a rather crude value of $\alpha$, but it is believed better to use this value than Luke's data, which can not be trusted in view of the difference between his experimental setup and a real TEFC motor. As a final remark, it is believed that Luke's approach of using dummies with a known heat generation is the best way of measuring the heat transfer coefficient of the end windings. Figs 49–52 show the measured and calculated stator winding temperatures for some of the identification tests.

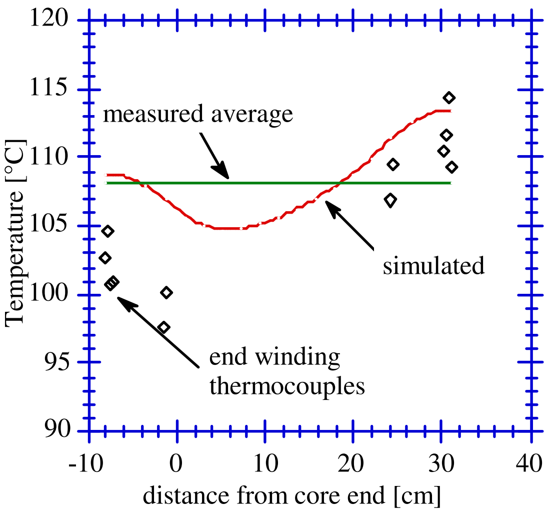

*Figure 49. Simulated and measured stator winding temperatures for the 15 kW-machine at rated load, 50 Hz.*

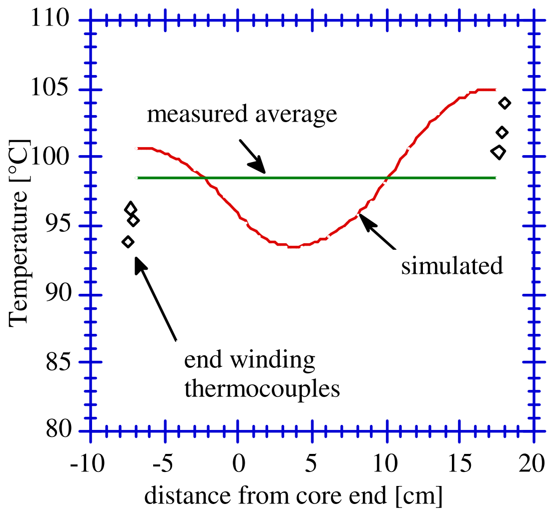

*Figure 50. Simulated and measured stator winding temperatures for the 4 kW-machine at rated load, 50 Hz.*

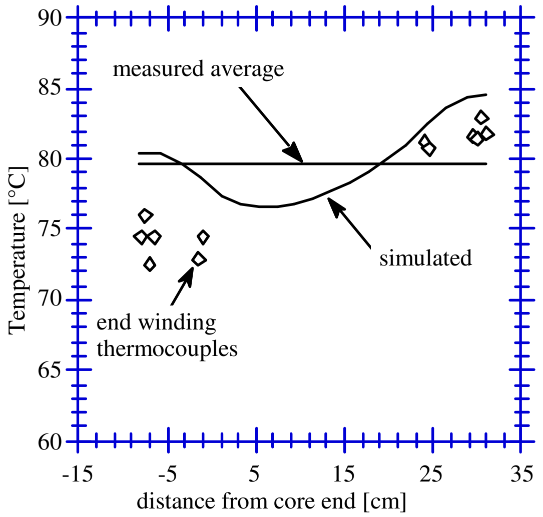

*Figure 51. Stator winding temperatures for the 15 kW-machine at 67 % rated load, 90 Hz.*

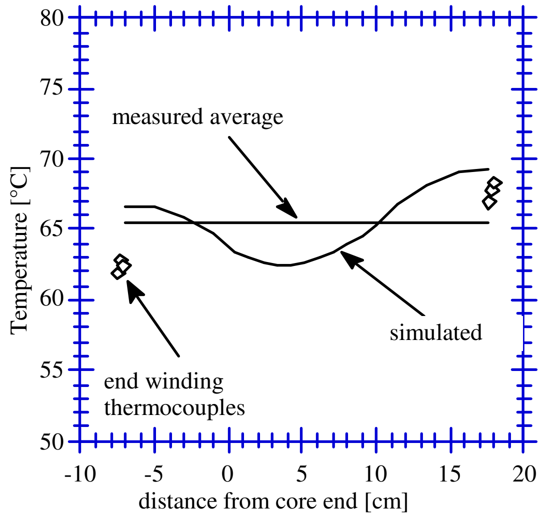

*Figure 52. Stator winding temperatures for the 4 kW-machine at 67 % rated load, 90 Hz.*

## 5.4 Stator core

The stator yoke is modelled with single-node configurations, since the heat flow coming from the stator teeth is usually much larger than the internally generated heat. Peripheral and axial heat flux is neglected. The stator yoke elements are hollow cylinders with a thermal resistance in the radial direction given by

$$R_{\mathrm{th}} = \frac{\ln r_2 - \ln r_1}{2\pi\lambda\ell} \tag{66}$$

where $r_2$ is the outer radius and $r_1$ the radius defined at the top of the slots.

The stator teeth are treated as being in parallel with each other. Peripheral temperature variations are neglected. Heat flow in the direction of the shaft is also neglected due to the thermal contact resistance between individual lamination sheets. Heat enters the teeth from the rotor. Along its way towards the yoke, more heat is added from the stator slots and from internal sources. Assuming that the heat flux entering from the slots is constant along the $y$-axis, the situation is similar to the one-dimensional problem that was discussed in Section 4.3. Consequently, a two-node configuration with equivalent thermal resistances is used as shown in Fig. 53.

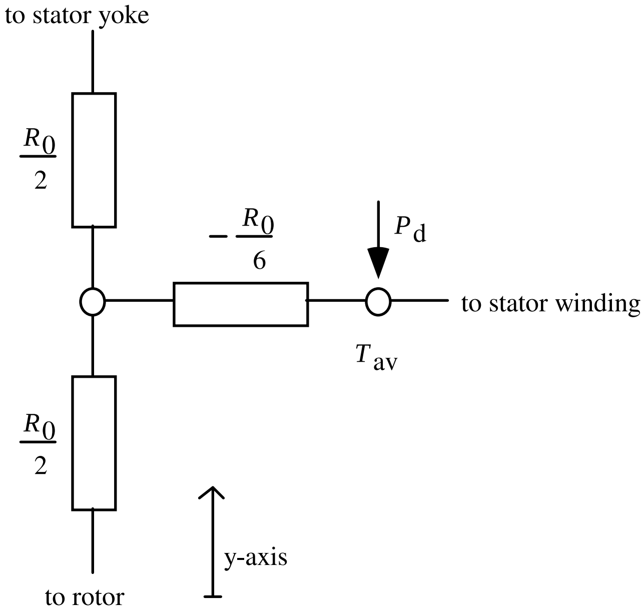

*Figure 53. Stator tooth node configuration.*

The average temperature is obtained in the node to the right in Fig. 53. Due to variations in the tooth-width, an integration should be performed along the $y$-axis to obtain the value of $R_0$. A tooth can usually be divided into four parts, as shown in Fig. 54.

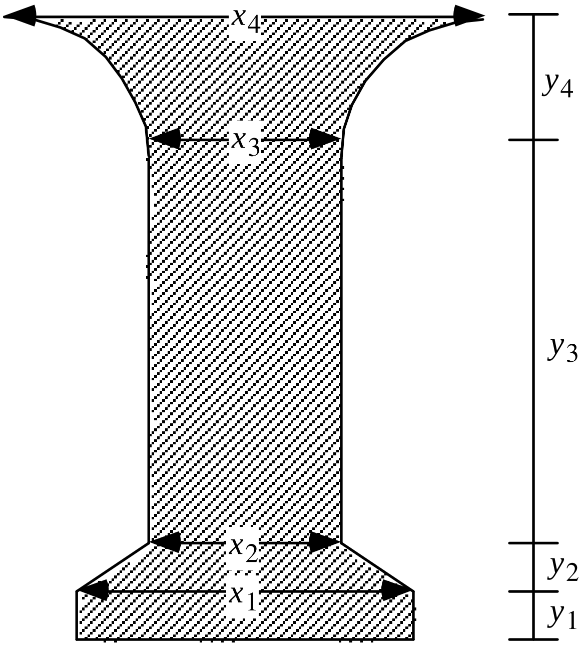

*Figure 54. Tooth geometry.*

The expression for $R_0$ is

$$R_0 = \int_0^{y_{\max}} \frac{1}{\lambda Q_s \ell x(y)} dy \tag{67}$$

where $y_{\max}=y_1+y_2+y_3+y_4$. Eq. (67) can be expressed as

$$R_0 = \frac{1}{\lambda Q_s \ell}\left(\frac{y_1}{x_1}+\frac{y_3}{x_3}+\frac{y_2}{x_1-x_2}\left(\ln\left|\frac{x_1 y_2}{x_1-x_2}\right|-\ln\left|y_2-\frac{x_1 y_2}{x_1-x_2}\right|\right)+\right.$$
$$\left.-\frac{\pi}{4}+\frac{a}{\sqrt{a^2-1}}\arctan\frac{a+1}{\sqrt{a^2-1}}\right) \tag{68}$$

where

$$a = \frac{x_3+2y_4}{2y_4} \tag{69}$$

## 5.5 Frame

### 5.5.1 Thermal resistance in the axial direction

The frame is usually cylindrical with straight fins to increase the cooling surface. The elements that model the frame are not identical, because the frame is thicker at the ends. Furthermore, the thickness of the frame against the core varies, since the core is not completetly circular. Therefore, an average value of the thickness should be used for those parts of the frame that are in contact with the core. The thermal resistance between two frame elements is

$$R_{\mathrm{th}} = \frac{\ell}{\lambda\left(2\pi rb + A_{\mathrm{f}}\right)} \tag{70}$$

where $b$ is the frame thickness, $r$ is the frame radius and $A_{\mathrm{f}}$ the cross-sectional area of the cooling fins.

### 5.5.2 Heat transfer to the ambient

A shaft-mounted fan blows air through cooling channels formed by the fins, as illustrated in Fig. 55. The cooling channels are approximately rectangular with one side open. Since one side is open, the air velocity decreases along the channels. The ratio between length and hydraulic diameter of the cooling channels is such that entrance effects are significant, which causes the heat transfer coefficient to be larger at the fan end than at the drive end.

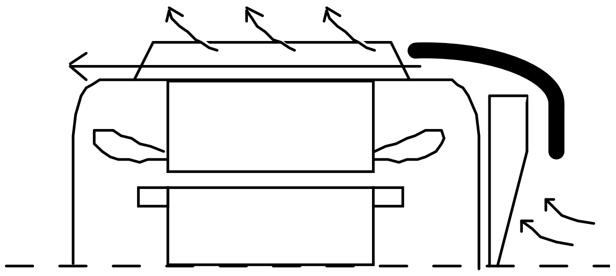

*Figure 55. Cooling air flow of a TEFC-motor.*

The hydraulic diameter is in this case defined

$$d_{\mathrm{h}} = \frac{4bh}{2h + b} \tag{71}$$

where $b$ is the space between fins and $h$ is the average height of the fins. It is assumed that the temperature difference between the fins and the wall is small. The flow mode in the cooling channels is turbulent, except at low speeds. This was verified by measuring the Reynolds number in the channels, which for the rated speed is about 4 times larger than 2300, which is considered as the critical value for closed channels. This makes it possible to use a formula by Nusselt [37], which takes the entrance effects into consideration and is commonly used for turbulent flow in tubes

$$Nu_{d} = 0.036\, Re_{d}^{0.8} Pr^{1/3} \left( \frac{d_{\mathrm{h}}}{\ell} \right)^{0.055} \tag{72}$$

Equation (72) gives a value of the average Nusselt number along the frame. Unfortunately, it is difficult to calculate, or even measure, an accurate value of $Re_{d}$, which limits the value of using Eq. (72). It is more reliable to measure an average value of the heat transfer coefficient using the average temperature rise of the frame and the total losses. Equation (72) tells us that $\alpha$ is proportional to $\omega^{0.8}$, since the air velocity in the cooling channels is proportional to $\omega$ (see Fig. 56).

The air velocity was measured in the centre of each cooling channel by a hot-wire anemometer. The sensor was small but not negligibly small compared to the cooling channels. This may have slightly affected the results. Figure 56 shows the air velocity in one of the cooling channels 1 cm from the fan outlet. The air velocity in this particular cooling channel was 50 % larger than the average velocity of all channels. The difference in air velocity between different cooling channels is explained by machine details that block the entrances of some cooling channels [10]. Figure 57 shows the measured average air velocity along the sides of the test machines at rated speed. $x$ is here the distance from the beginning of the cooling channels near the fan.

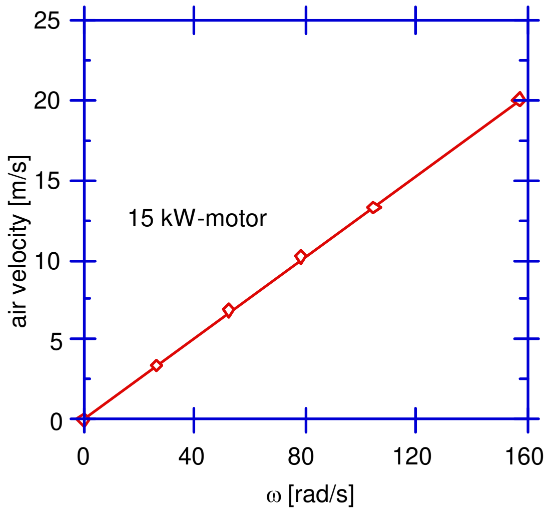

*Figure 56. Measured air velocity in a cooling channel near the fan, plotted against the angular velocity.*

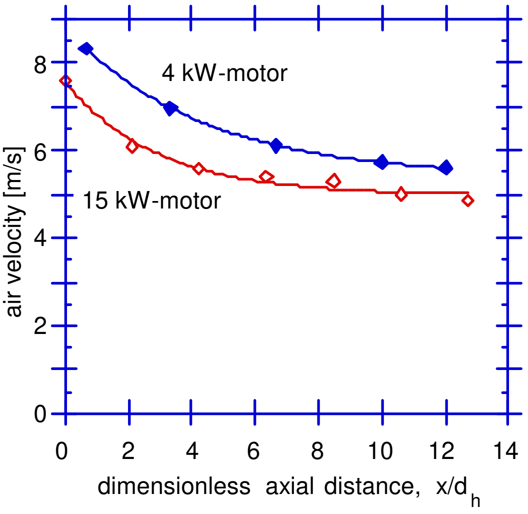

*Figure 57. Air velocity variations along the frame*

Figure 58 shows measured values of $\alpha$ for a range of speeds and loads of the two test machines, and compares them with curves of the type $\alpha = c_1 + c_2\omega^{0.8}$. $\alpha$ was here computed using the total losses, the average temperature rise of the frame and the total external surface of the frame, including the fins and the end shields.

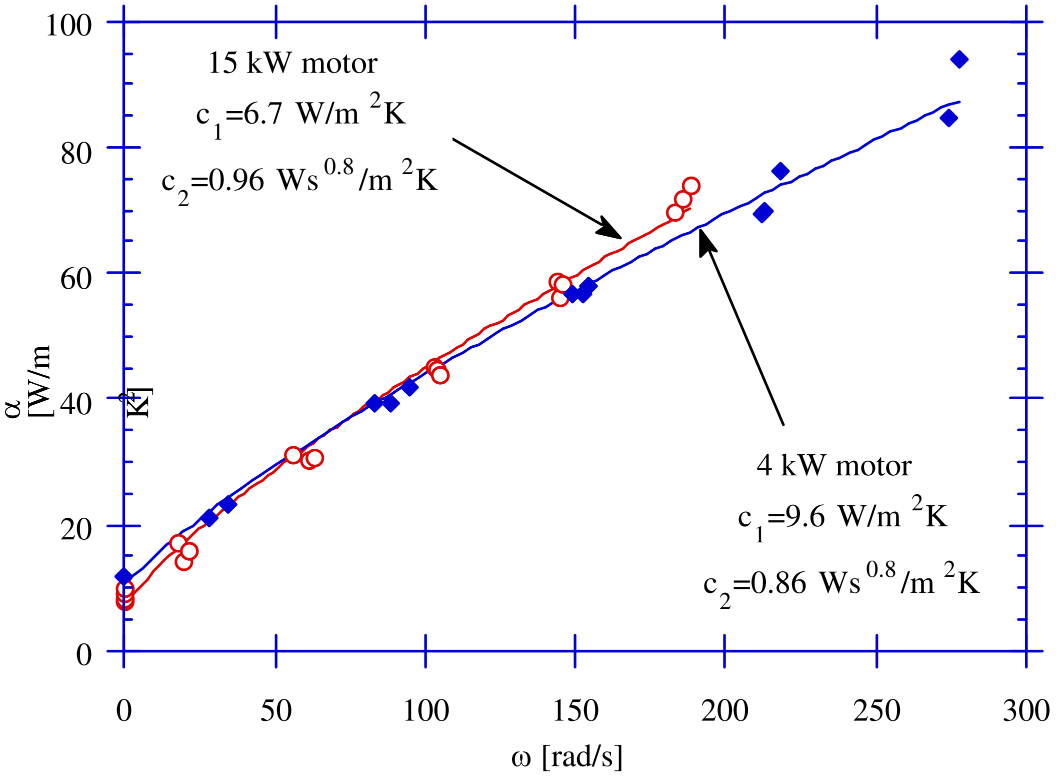

*Figure 58. Measured average heat transfer coefficient of the frame.*

The magnitude of $\alpha$ is almost the same for the two machines, but this may be a coincidence. The three data points for each speed in Fig. 58 are, with some exceptions, for no load, 2/3 of rated torque and rated torque. It can be seen that the temperature dependence of $\alpha$ can be neglected, because the three different load cases give approximately the same value of $\alpha$. The fact that $\alpha$ is not zero at standstill is explained by the effects of natural convection and radiation.

The question still remains how $\alpha$ varies along the frame. As far as the author knows, this has not yet been thoroughly examined. In order to do this, an especially prepared dummy frame would have to be constructed, which unfortunately is beyond the scope of this work. However, the local heat transfer of closed channels, such as tubes, has been well investigated by Mills [38]. The heat transfer in tubes and motor frames is probably comparable, although some nonsimilarities in the air flow patterns exist. Mills investigated several different entrance effects for turbulent flow in tubes with a uniform heat flux boundary condition at the wall. Three curves that possibly are relevant for a TEFC motor frame are shown in Fig. 59. $Nu_x$ is the local Nusselt number and $Nu_\infty$ is the Nusselt number at fully developed flow, i.e. when no entrance effects remain. Figure 60 shows a suggested axial variation of the heat transfer coefficient, normalized to 1 at the drive end.

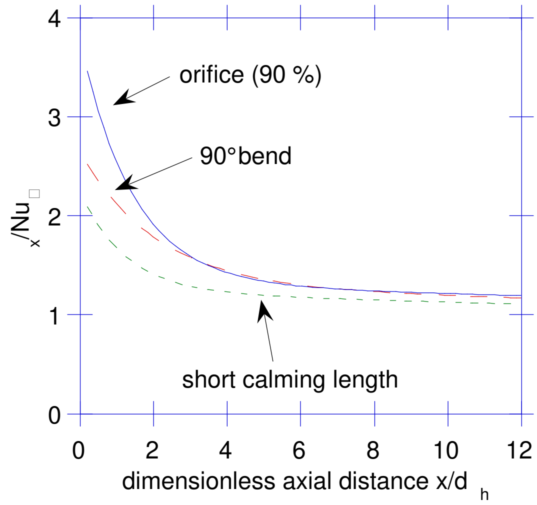

*Figure 59. Entrance effects for turbulent flow in tubes.*

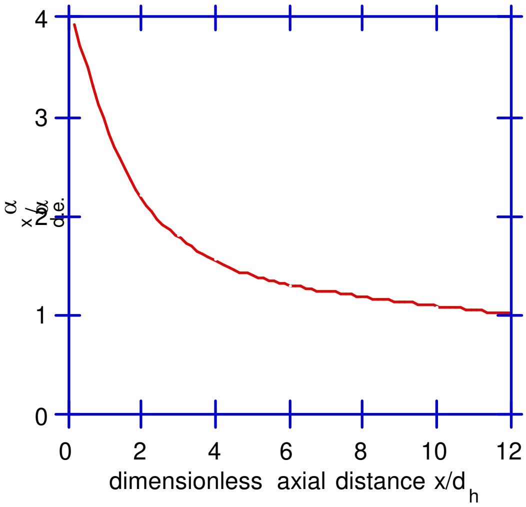

*Figure 60. Suggested axial variation of the heat transfer coefficient, normalized to 1 at* $x/d_h$*=12.*

The curves in Fig. (59) can be described by a constant plus an exponentially decreasing value. However, these curves can not be used as they are; some corrections must first be applied. The first correction is due to the heating of the air along the channels, which is neglected in the thermal model, but was not neglected by Mills. In order to correct for this error, the slope of $Nu_x$ along $x$ must be made steeper than in Fig. 59, for instance by adding a linear term. If the temperature rise of the cooling air is, say 30 % of the temperature rise of the frame at the drive end, then the linear term should compensate for this by a 30 % lower value of $Nu_x$ at the drive end. The second correction is due to the decrease in air velocity along $x$. This correction can be made by multiplying the curve in Fig. 59 by the velocity curve in Fig. 57, raised to the power of 0.8. By using the mean value of the curves in Fig. 59, and applying the suggested corrections, the curve shown in Fig. 60 was constructed. It shows the local value of the heat transfer coefficient, based on the above assumptions, and normalized to 1 at the drive end of the test motors. It can be described by:

$$\mathrm{f}\left(\frac{x}{d_\mathrm{h}}\right) = 1.48 - 0.039\,\frac{x}{d_\mathrm{h}} + 2.8\,\mathrm{e}^{-0.63\frac{x}{d_\mathrm{h}}} \tag{73}$$

The actual values of the local heat transfer coefficient can be obtained by integrating Eq. (73) along the frame, and by scaling the resulting average value according to a measured average heat transfer coefficient. Alternatively, a more accurate method can be used, that models the frame with an identification model.

An identification model for the frame is shown in Fig. 61. The model is not accurate enough to identify each thermal resistance from the frame to the ambient individually; a distribution along $x$ must first be assumed.

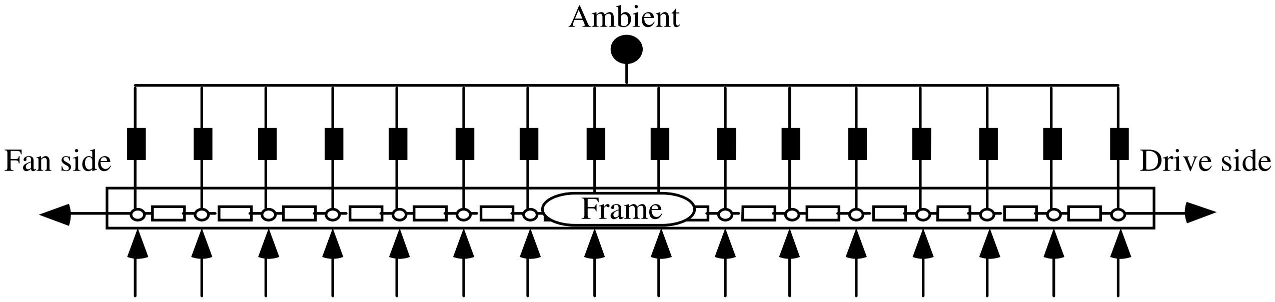

*Figure 61. Model for the identification of the thermal resistances between the frame and the ambient.*

The boundary conditions of the model are the ambient temperature and the heat flux from the interior of the machine and from the end shields. The heat flux from the interior is obtained from an earlier described model (Fig. 31.). The amount of heat that goes from the frame to the end shields must necessarily be a crude approximation, because it can not easily be measured. The temperature gradients at the ends of the frame can be of some help here. At the identification, the thermal resistances between the frame and the ambient are calculated using

$$R_{\mathrm{th}}\left(\frac{x}{d_{\mathrm{h}}},\omega\right)=\frac{1}{k+c\mathrm{f}\left(\frac{x}{d_{\mathrm{h}}}\right)\omega^{0.8}} \tag{74}$$

where $c$ is the constant to be identified. The effect of natural convection and radiation is modelled by the constant $k$, which is determined by a locked rotor test. In principle, the effects of natural and forced convection should not be added in this way, but the alternative is significantly more complicated, and would not greatly influence the result. The identification is performed by comparing the measured and calculated frame temperatures, and adjusting $c$ until a close fit is achieved. Figures 62 and 63 show measured and calculated temperatures for rated operation of the two test machines.

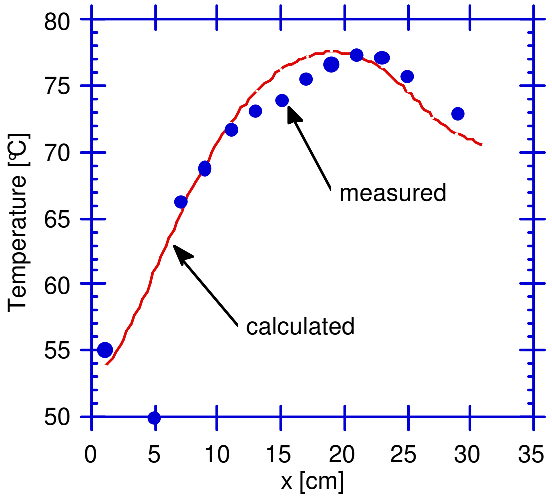

*Figure 62. Measured and calculated frame temperatures of the 15 kW motor. The value c=0.04 $Ws^{0.8}K^{-1}$*

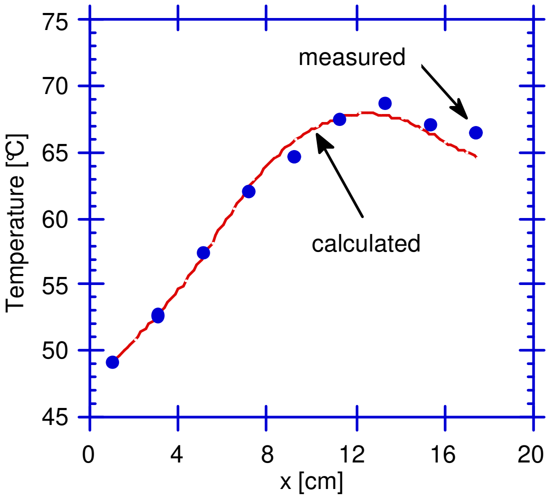

*Figure 63. Measured and calculated frame temperatures of the 4 kW motor. The value c=0.0076 $Ws^{0.8}K^{-1}$*

It can be seen that the chosen function $R_{\mathrm{th}}(x)$ gives a fairly good fit between the calculated and measured frame temperatures. Although this does not prove that $\mathrm{f}(x)$ is the true distribution of $\alpha$ along the frame, it is a good alternative, since the local Nusselt numbers in the cooling channels are difficult to measure directly.

Figures 64–66 are photos taken by an infrared camera, showing the temperature distribution of the 4 kW motor at rated operation. The bright line in Figs 64–66 is an isotherm. The isotherms visualize, among other things, the peripheral temperature variations, and where the hottest spot of the frame is located.

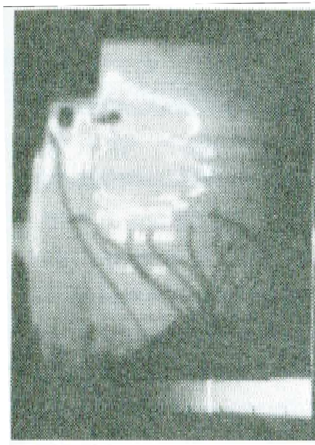

*Figure 64. Isotherm at 68° C.*

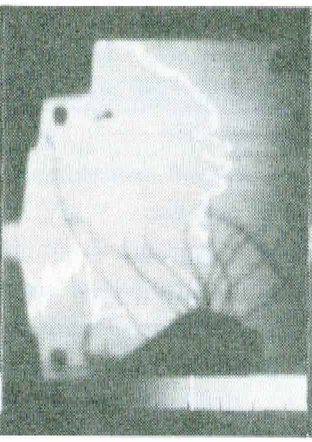

*Figure 65. Isotherm at 65 °C.*

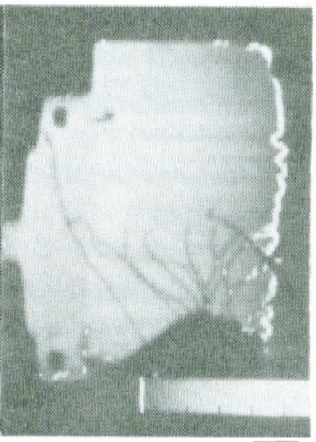

*Figure 66. Isotherm at 50° C.*

### 5.5.3 Thermal contact resistance between the frame and the stator yoke

For shrink-fitted frames there is a thermal contact resistance between the frame and the stator yoke that is not negligible. The temperature drop over this junction may be appreciable. The magnitude of the thermal contact resistance depends on contact pressure, material softness and surface roughness [1]. In order to investigate if the thermal contact resistance is significant also when the frame is cast directly on the core, an identification model was used together with the results from a test where the rotor is first removed. The advantage of removing the rotor is that the heat path to the rotor is eliminated, and the temperature of the inner stator tooth surface can be measured, which eliminates the need for drilling. The left node in the two-node configuration of the stator teeth (see Fig. 53), is now equivalent to the stator tooth surface temperature if the teeth are lossless. By series-connecting the phases and applying a DC voltage, the stator windings are heated by a known power. Because the stator yoke and teeth are lossless, the identification model shown in Fig. 67 can be used.

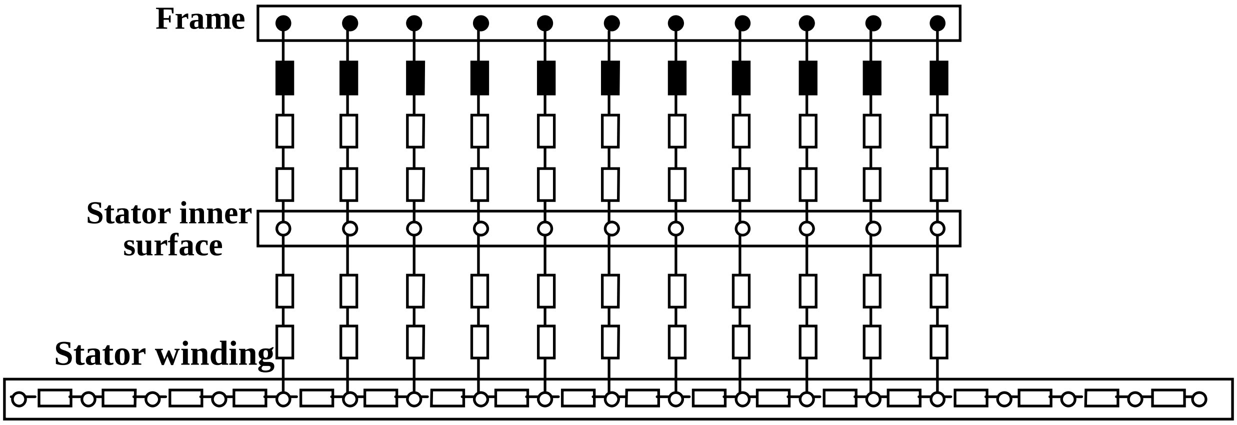

*Figure 67. Model for identifying the thermal contact resistance between the frame and the stator yoke.*

Note that the nodes where normally the stator yoke and teeth losses are injected are omitted here; only the left node in the stator teeth node configuration is represented. The thermal resistances between the stator tooth surface nodes and the stator winding nodes do not need to be known. Nearly all heat must go through the stator core to the frame, only some heat also dissipates from the end windings, but this heat can be calculated and deducted using Eqs (63) and (64). In order not to exceed maximum winding temperature, an external cooling air source can be used.

The steps in the identification procedure are: Calculate the stator surface temperatures for some value of the thermal contact resistance; then compare the calculated temperatures to the measured stator surface temperatures; repeat this until measured and theoretical values are equal. It is important that the frame and stator surface temperature measurements are performed at the same peripheral angle and axial distance.

This test was performed for the 4 kW machine, whose frame is cast directly on the core. The result corresponded to a temperature drop of only 0.5°C over the junction at 70 % of rated losses. The result leads to the conclusion that the thermal contact resistance can be neglected for machines with the frame cast directly on the core.

## 5.6 End shields

The end shields are most efficiently cooled at their outer peripheries. The peripheries of the end shields are assumed to be in good thermal contact with the frame. An end shield node can consequently be connected to the adjacent frame node by some arbitrary, low value of the thermal resistance. The thermal resistance between the end shield and the bearing is calculated from the outer periphery to the bearing housing by an equation of the same type as Eq. (69).

In order to get some values of the internal heat transfer coefficient of the end shields, an identification procedure for the two test motors was performed. The model mentioned earlier (Fig. 31) and Eqs (48) and (65) were used to determine the amount of heat going to the internal air from the rotor and stator windings. This heat must be absorbed by the frame and the end shields. It is assumed that the internal heat transfer coefficients of the frame and the end shield are the same. Since the temperatures and areas were measured, the heat transfer coefficients can be identified. The result is shown in Fig. 68 as a function of the peripheral speed of the rotor. The area was calculated from an idealized smooth shape of the end shields, thus neglecting the fin arrangement at the inside of the end shield.

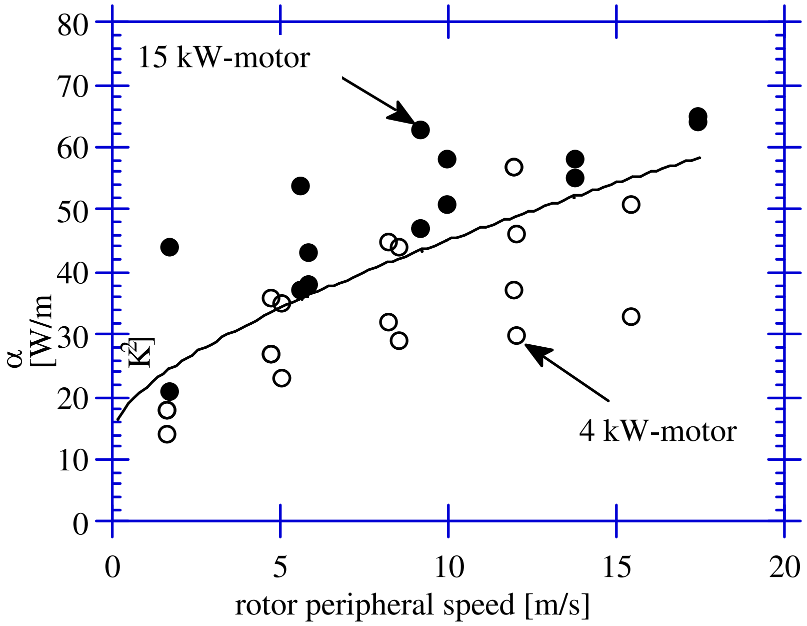

*Figure 68. Internal heat transfer coefficient of the end shields .*

Two data points were obtained from the tests: one for each end shield. The scatter of the data points depends, among other things, on that different values were obtained for each end shield, which was unexpected since they had the same internal geometry. The reason is unclear, although a possible explanation is bad accuracy in the temperature measurement for the end shields or internal air. It is also possible that the heat transfer coefficient of the internal parts of the frame is much higher than that of the end shield, since the heated internal air reaches the frame first. A further comment on the results shown in Fig. 68 is that the 15 kW motor has a larger heat transfer coefficient than the 4 kW motor. However, a general size dependence is not assumed on the basis of these measurements. Instead, the curve fit shown in Fig. 68 is suggested to be used. It was fitted by weighting the data equally for both test machines, and is described by

$$\alpha = k_1 + k_2 u_r^{0.65} \tag{75}$$

where $k_1$=15 W/m$^2$K and $k_2$=6.75 (s/m)$^{0.65}$W/m$^2$K. Equation (75) is similar in magnitude to a formula given by Kotrba in [33].

The external heat transfer coefficients of the end shields are difficult to calculate analytically because the air flow conditions around them are not well known. The total heat that enters the end shields comes from the bearings, the internal air and the frame. The evaluation of the thermal resistances between the end shields and the ambient was done by experimenting with different parameters and assuming the same speed-dependence as that of the frame. The complete thermal model in Fig. 28 was used. The heat transfer coefficients for both the 4 kW motor and the 15 kW motor were fairly well described by

$$\alpha_{fe} = k_3 + k_4 u_r^{0.8} \tag{76}$$
$$\alpha_{de} = k_5 + k_6 u_r^{0.8} \tag{77}$$

where $k_3$=$k_5$=15 W/m$^2$K, $k_4$=10 (s/m)$^{0.8}$W/m$^2$K, and $k_6$=2.5 (s/m)$^{0.8}$W/m$^2$K. $u_f$ is the peripheral speed of the fan and $\alpha_{fe}$ and $\alpha_{de}$ are the heat transfer coefficients at the fan end and the drive end, respectively. Equations (76) and (77) must be regarded as approximative. The area was calculated from an idealized smooth shape of the end shields. The fan cover of the 4 kW machine was in good thermal contact with the end shield, so the internal fan cover area was included in the area calculation for that machine. It is difficult to say whether it is appropriate to use the peripheral fan speed to describe $\alpha_{fe}$ and $\alpha_{de}$. However, the author wanted to compare the results with those of Kotrba [33], who gave them in this form. It then turns out that Eqs (76) and (77) give about twice as large value as the formulas suggested by Kotrba. It might be better to describe $\alpha_{\mathrm{fe}}$ and $\alpha_{\mathrm{de}}$ more generally as a function of the heat transfer coefficient of the frame, since not only the fan speed, but also the fan design affects them. Another, crude, but more general approach is to assume that a certain fraction of the total losses leaves the machine from the end shields. At rated operation, they would be 12 % and 6 % for the 15 kW motor and 19 % and 9 % for the 4 kW motor, where the former percentage for each motor concerns the fan end and the latter the drive end.

## 5.7 Bearings

Grease-lubricated ball bearings are the most common type of bearing for TEFC-motors. The bearing consists of the inner and outer races, the balls and the cage, which keeps the balls in their positions. The inner race is pressed directly on the shaft and the outer race is supported by the end shield. The maximum temperature of the bearing is usually at the inner race, but can sometimes be at the balls (only at very high speeds). The maximum temperature determines what type of grease to be used, and affects the regreasing interval. The temperatures of the inner and outer races are needed to determine which radial slackness should be used. The drive side bearing housing is shown in Fig. 69. The bearing is modelled by the thermal network shown in Fig. 70. The inner race and the shaft directly below it are lumped together as a node with 25 % of the bearing losses. Likewise, the outer race and the inner part of the end shield are lumped together as a node with 25 % of the bearing losses. The balls and the cage are modelled by a node with 50 % of the bearing losses. In addition, the rubber sealing at the drive end causes losses, which are added to the node for the outer race.

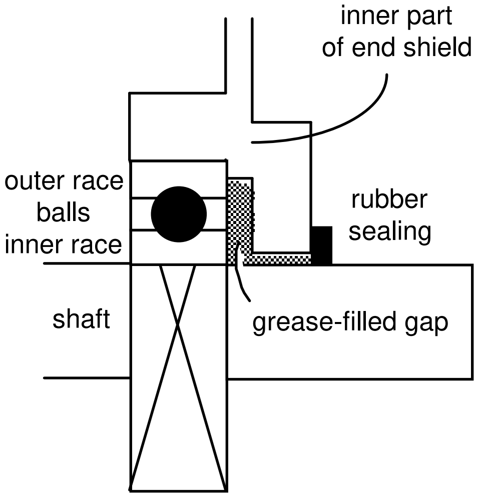
inner part of end shield
outer race
balls
inner race
rubber sealing
shaft
grease-filled gap

*Figure 69. Bearing housing.*

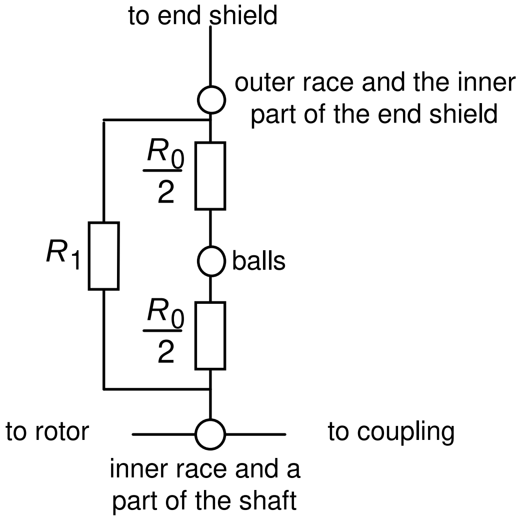
to end shield
outer race and the inner part of the end shield
$\frac{R_0}{2}$
$R_1$
balls
$\frac{R_0}{2}$
to rotor
to coupling
inner race and a part of the shaft

*Figure 70. Bearing thermal model.*

The thermal resistance $R_0$ through the bearing depends among other things on the equivalent contact surface between the balls and the oil film, which is difficult to calculate. There is also a thermal resistance $R_1$ in parallel with the bearing due to the grease-filled gap shown in Fig. 69. It was decided to neglect $R_1$ and to choose $R_0$ so that the calculated temperatures of the bearing inner and outer races became close to the measured ones. This means that the temperature of the balls are underestimated. However, this is of little importance as long as the inner race is the hottest part of the bearing. The adopted values of $R_0$ for the bearings at rated speed were 0.48 K/W for the 15 kW motor (with an average bearing diameter of $d_b$=77.5 mm), and 0.88 K/W for the 4 kW motor (with an average bearing diameter of $d_b$=46 mm).

$R_0$ has a significant negative speed dependence, which is assumed to be a linear function of the velocity of the balls. Furthermore, if it is assumed that the bearing-size dependence of $R_0$ is a linear function of $d_b$, a general formula for $R_0$ can be constructed from the test results of the two test motors

$$R_0 = k_1(0.12 - k_2 d_b)(33 - k_3 \omega d_b) \tag{78}$$

where $k_1$=0.45 K/W, $k_2$=1 $m^{-1}$ and $k_3$=1 s/m. The second factor in Eq. (78) accounts for the size dependence, while the third factor accounts for the speed dependence. The value given by Eq. (78) is an approximate value and can only be used for bearing diameters and speeds that are close to the values that were used to derive the formula, i.e. (46 mm≤$d_b$≤77.5 mm) and ($\omega d_b$≤14.5 m/s).

Temperature measurements close to the drive side bearings of the test machines are presented in Figs 71–72. The only actual bearing temperature that was measured was that of a sealing plate on the bearing of the 15 kW motor.

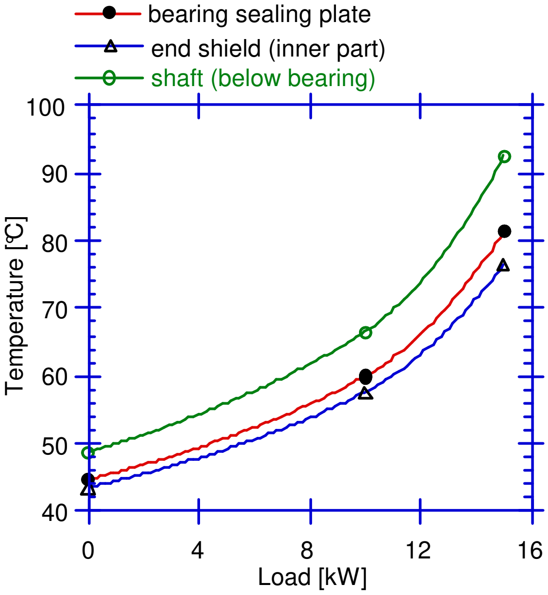

*Figure 71. Measured temperatures close to and at the bearing, 15 kW machine.*

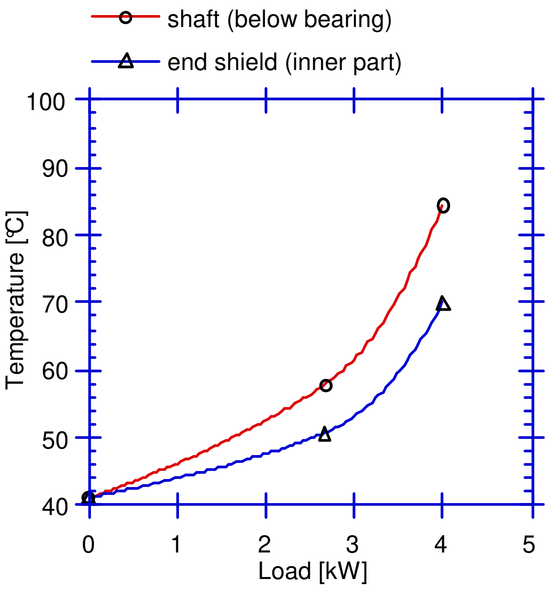

*Figure 72. Measured temperatures close to the bearing, 4 kW machine.*

# 6 Steady-state results

## 6.1 Optimum size of thermal networks

When designing a thermal network for an electrical machine, a decision must be made about the level of discretization and the kind of node configurations that are desired. In [1,5], multiple-node configurations and a low level of discretization (9–10 elements) are proposed. However, a higher level of discretization can be implemented without problems. A higher level of discretization can also make the multiple-node configurations unnecessary, since the errors from using the single-node configuration obviously decrease with increasing number of elements. The natural question then becomes: What number of elements is needed to make errors resulting from the discretization negligible?

To investigate this, a program was constructed in such a way that an arbitrary number of nodes could be used to calculate the steady-state temperature of a certain machine. This model had a constant discretization in the radial direction, but the amount of nodes in the axial direction could be freely chosen. There is no discretization in the peripheral direction, since a general assumption is that there are no peripheral temperature differences (except between the stator teeth and the coil sides). Model parameters for the 4 kW and 15 kW machines were tested. By comparing results for models of different sizes, the axial discretization errors could be identified. Comparisons are shown in Fig. 73. The reason why the discretization in the radial direction was not changed is that the radial discretization is rather self-evident. In short, it can be said that radial discretization is not necessary if the radial temperature gradient is small (as in the frame and in the rotor bars) or if the internal losses are small compared to the external heat input (as in the stator and rotor yokes and the air gap). The stator teeth are an exception. They are represented by two-node configurations to make further radial discretization unnecessary.

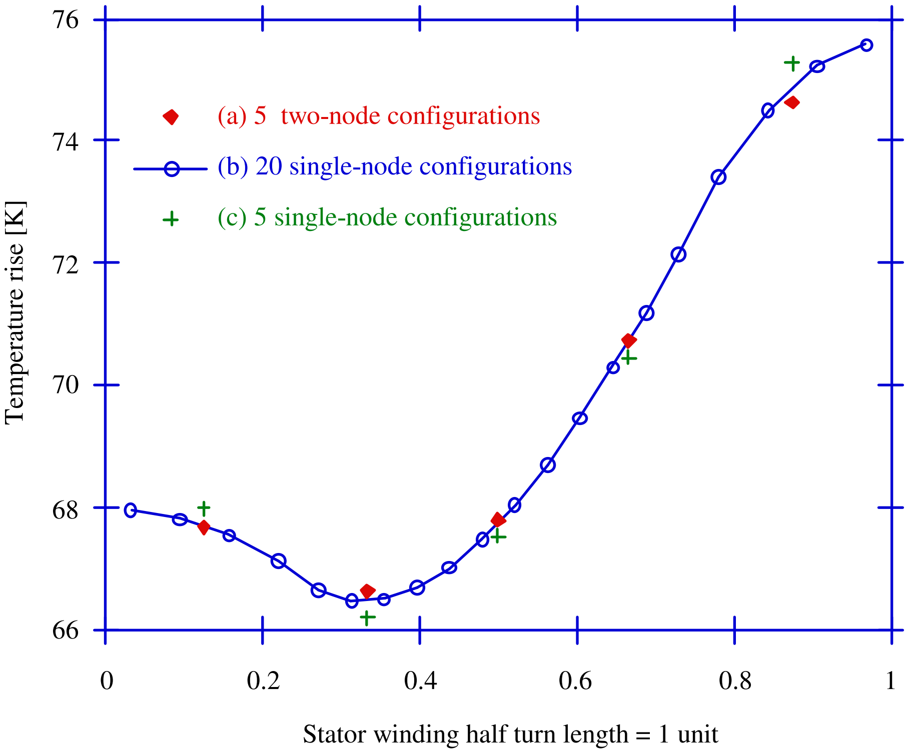

*Figure 73. Stator winding temperature simulation with different levels of discretization in the axial direction.*

In Fig. 73 comparisons are made between

(a) a stator winding model with 5 two-node configurations
(b) a stator winding model with 20 single-node configurations
(c) a stator winding model with 5 single-node configurations

It can be seen that the data points of case (a) are the average values of case (b). The discretization errors of case (a) and (b) are negligible. The data points of case (c) however, have errors up to 0.5 °C. This would be expected as a result of the lower level of discretization. Even so, an error of 0.5° C is quite a small error, so it can be concluded that single-node configurations are sufficient even for a small model. However, if a small model is used, the resolution is poor. In order to obtain more detailed information, a large model similar to case (b) would be needed. Thus the question of the optimum network size is answered by the need for resolution.

## 6.2 Sensitivity analysis

In order to determine how errors in the parameters of the thermal model affect the temperature predictions, a sensitivity analysis was performed. The temperatures of the stator end winding and the bearing at the drive side were calculated before and after some values of thermal resistances had been changed by 20 %. A small resulting change in temperature indicates a low sensitivity to errors in those particular thermal resistances. The sensitivity to erroneous stator winding losses, rotor losses and bearing losses was also investigated. The sensitivity analysis was limited to rated load at 50 Hz and at an ambient temperature of 25° C. The parameters that were changed and the corresponding changes in temperature are given in Table 3.

*Table 3. Results of the sensitivity analysis. The temperature changes of the 15 kW motor are given first and the temperature changes of the 4 kW motor are given within parenthesis. Each parameter was increased by 20 %.*

| Parameter description (parameter was increased by 20 %) | End winding $\Delta T$ [°C] | Bearing $\Delta T$ [°C] |
|---|---|---|
| $R_{\text{th}}$ between stator windings and stator teeth | 3.07 (3.16) | 0.17 (0.14) |
| $R_{\text{th}}$ between frame and ambient | 7.06 (5.24) | 5.88 (4.58) |
| $R_{\text{th}}$ between end shields and ambient | 1.19 (1.52) | 1.54 (1.65) |
| $R_{\text{th}}$ between end windings and internal air | 0.99 (0.77) | -0.10 (-0.06) |
| $R_{\text{th}}$ between rotor end rings and internal air | -0.37 (-0.10) | 0.30 (0.17) |
| $R_{\text{th}}$ between end shields and internal air | 1.74 (1.06) | 0.15 (0.26) |
| $R_{\text{th}}$ between rotor and shaft | 0.02 (0.02) | -0.24 (-0.11) |
| $R_{\text{th}}$ between coupling and ambient | 0.09 (0.13) | 0.90 (0.81) |
| $R_{\text{th}}$ between rotor and stator teeth | 0.29 (-0.03) | 1.65 (1.15) |
| $R_{\text{th}}$ through bearings | 0.05 (0.09) | 0.84 (0.56) |
| $R_{\text{th}}$ between adjacent frame elements | 0.59 (0.76) | -0.06 (0.37) |
| stator winding losses | 9.73 (11.29) | 2.75 (4.16) |
| rotor losses | 7.53 (3.76) | 7.00 (4.56) |
| bearing losses | 0.10 (0.07) | 0.73 (0.33) |

From Table 3 it can be seen that it is very important that the losses are accurately calculated, especially the stator winding losses. It is also very important that the thermal resistances between the frame and the ambient are correct. The thermal resistance between the stator windings and the stator teeth is of course important for the calculation of the stator end winding temperature. Interestingly, the stator end winding temperature is more sensitive to the parameters of the end shields than to those of the end windings. This is probably because the end shields affect the internal air temperature more than the end windings do. The bearing temperature is sensitive to the frame- and rotor-related parameters. The bearing losses, however, are so small for the test machines that a 20 % increase does not change the bearing temperature much. A 20 % increase in the bearing thermal resistance gives a moderate change in the ball temperature, whereas the inner race temperature will be increased twice as much as the ball temperature.

## 6.3 Comparison of calculated and measured data

A comparison of calculated and measured steady-state temperatures was made using the analytical or empirical formulas for the thermal resistances that were suggested in Chapter 5. The losses that were used in the thermal model are the same as previously shown in Tables 1–2. The ambient temperature was different in each test but always between 20 and 25 °C.

### 6.3.1 4 kW motor

The results for the 4 kW motor are shown in Figs 74–79. The calculated temperatures are shown as solid lines and the measured temperatures as point values. The average stator winding temperature, measured by the resistance method, is shown as a dashed line. It can be seen that the agreement between measured and calculated frame and stator winding temperatures is good except at 10.6 Hz where the calculated frame temperature is lower than the measured. The thermocouples on the end windings are cooler than predicted, which can be explained by the influence of the air and their positions at the surface of the end windings. The calculated rotor temperature is slightly lower than the measured one, which probably is explained by underestimated rotor losses or overestimated heat flow from the end rings to the internal air.

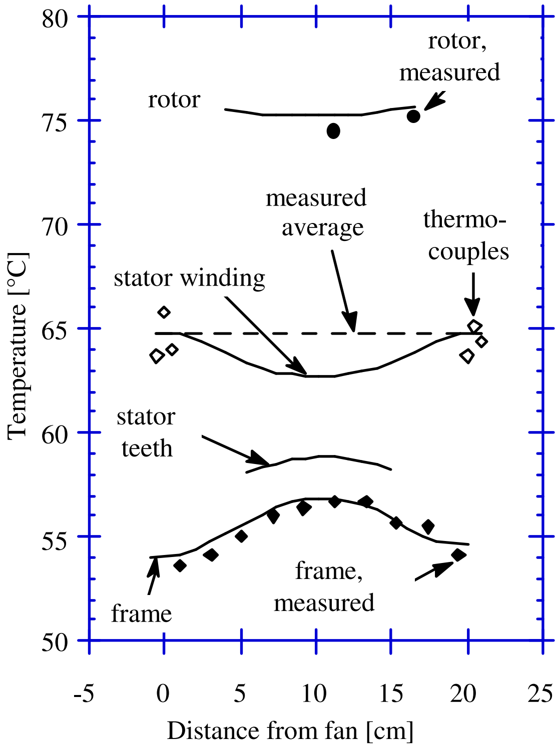

*Figure 74. Temperatures of the 4 kW motor with locked rotor.*

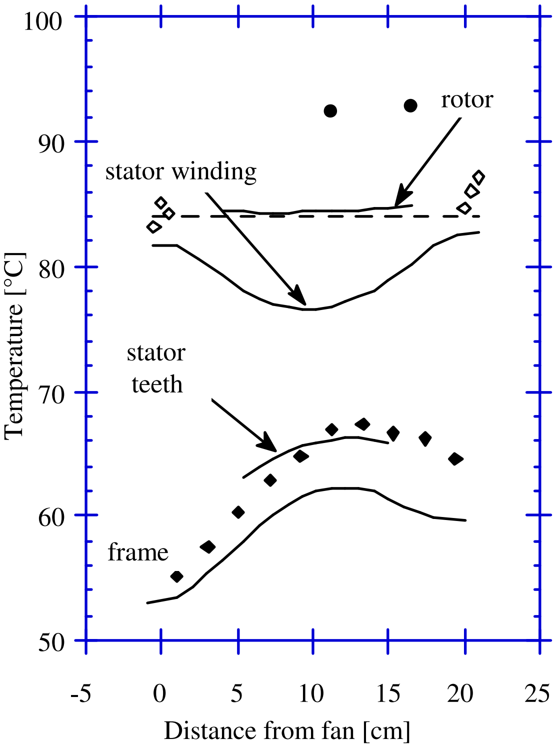

*Figure 75. Temperatures of the 4 kW motor at 10.6 Hz, 17.7 Nm.*

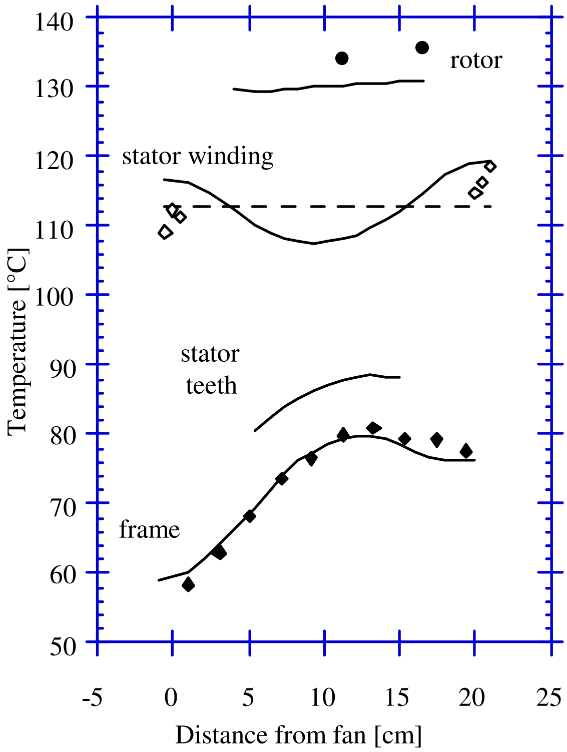

*Figure 76. Temperatures of the 4 kW motor at 29.5 Hz, 26.7 Nm.*

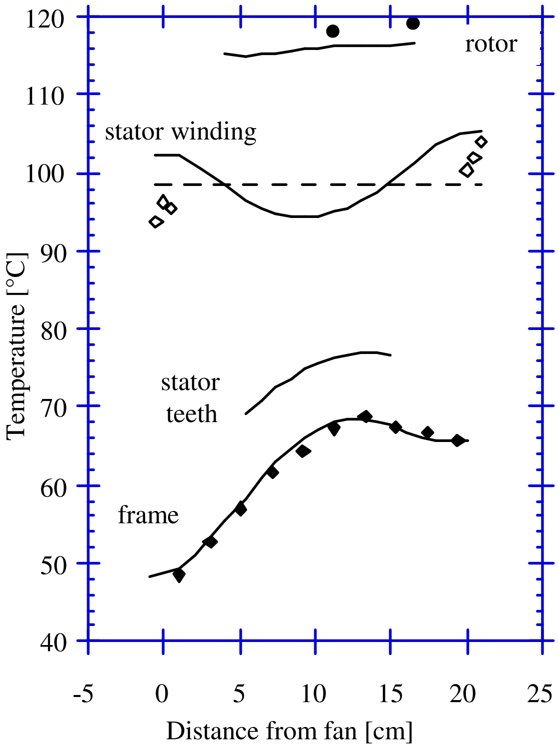

*Figure 77. Temperatures of the 4 kW motor at 48.8 Hz, 26.7 Nm.*

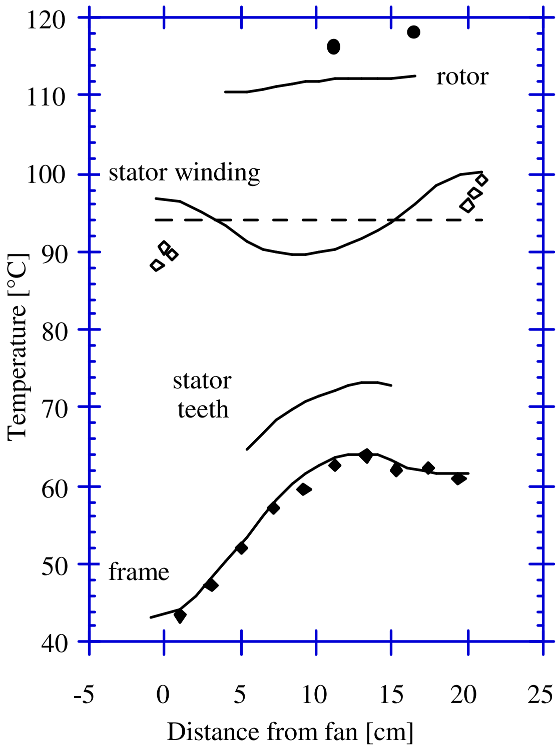

*Figure 78. Temperatures of the 4 kW motor at 69.9 Hz, 26.6 Nm.*

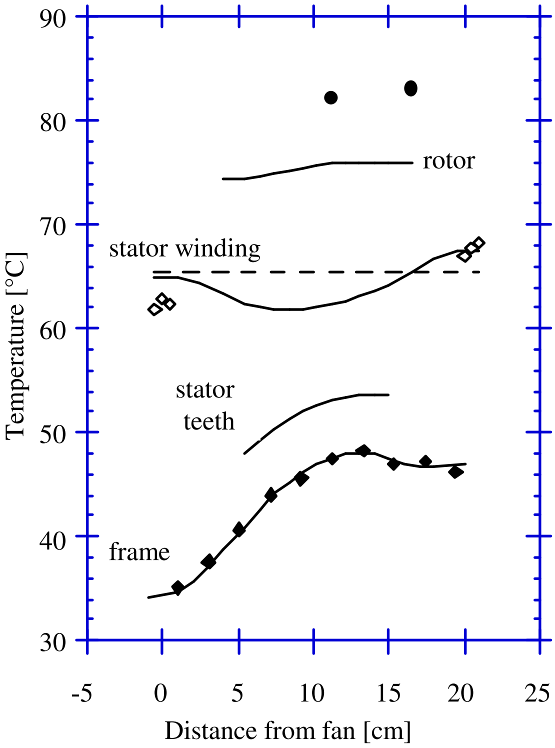

*Figure 79. Temperatures of the 4 kW motor at 89.2 Hz, 17.6 Nm.*

### 6.3.2 15 kW motor

The results for the 15 kW motor are shown in Figs 80–85. It can be seen that the agreement between measured and calculated frame temperatures is good. The calculated stator winding temperatures are somewhat higher than the measured ones for the two tests using rated torque (Figs 82–83). This is partly explained by overestimated internal air temperatures and probably also by temperature dependence of the thermal resistance between the coil sides and the stator teeth, which was neglected. The calculated rotor temperature is slightly higher than the measured ones, which probably is explained by overestimated rotor losses or underestimated heat flow from the end rings to the internal air.

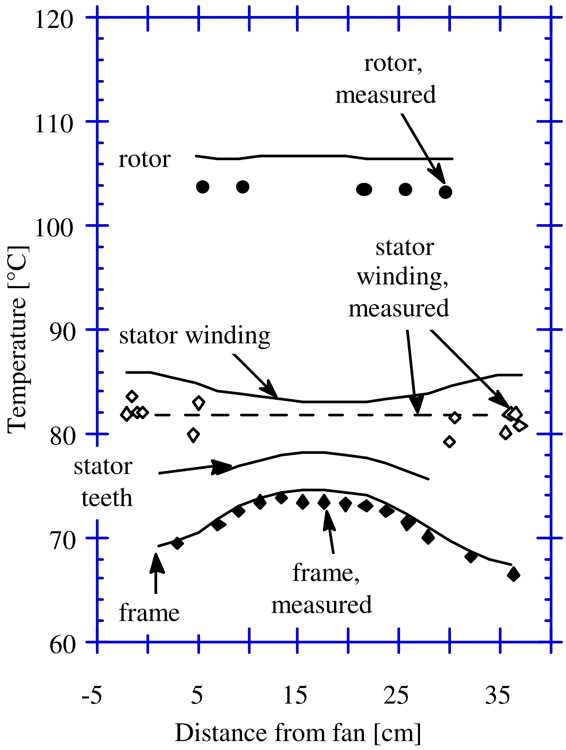

*Figure 80. Temperatures of the 15 kW motor with locked rotor.*

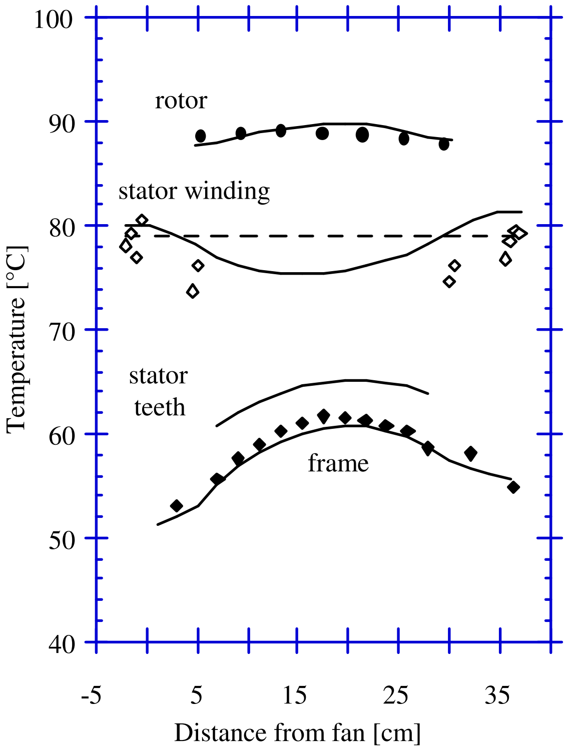

*Figure 81. Temperatures of the 15 kW motor at 9.6 Hz, 97 Nm.*

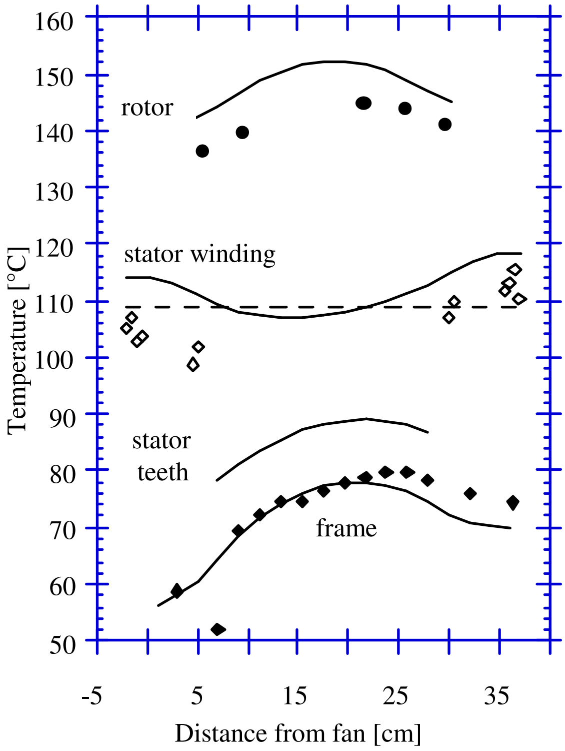

*Figure 82. Temperatures of the 15 kW motor at 29.7 Hz, 147 Nm.*

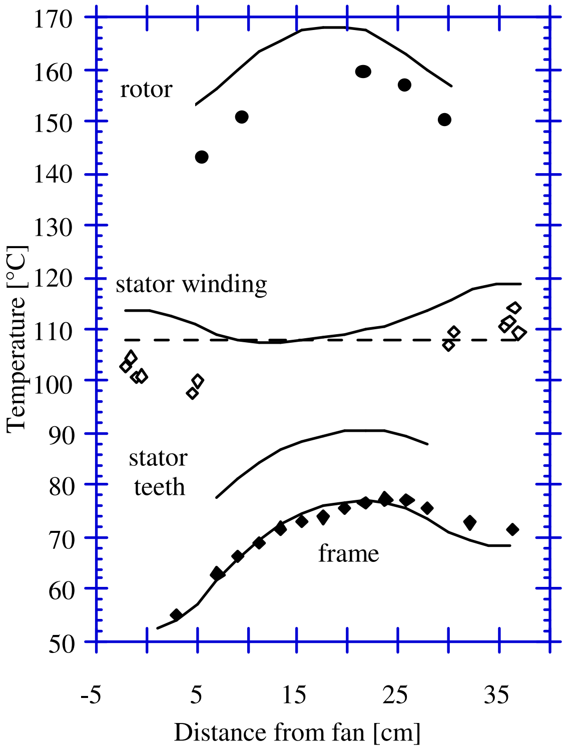

*Figure 83. Temperatures of the 15 kW motor at 47.9 Hz, 148 Nm.*

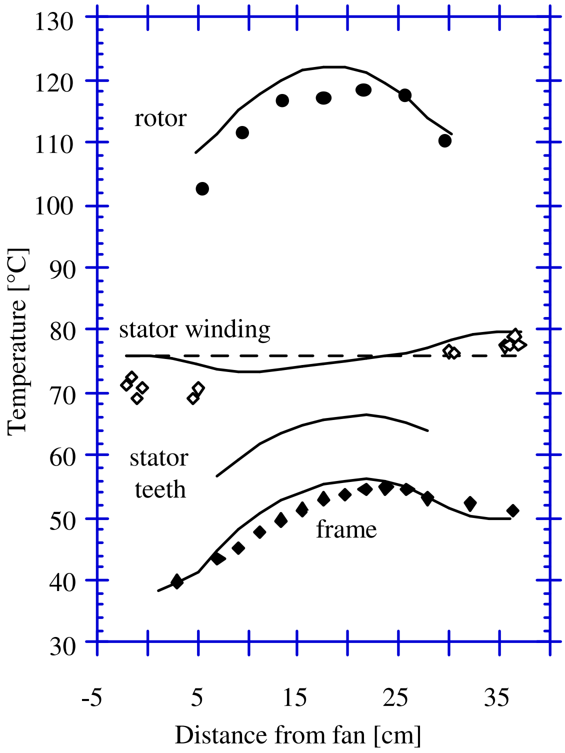

*Figure 84. Temperatures of the 15 kW motor at 69.8 Hz, 99 Nm.*

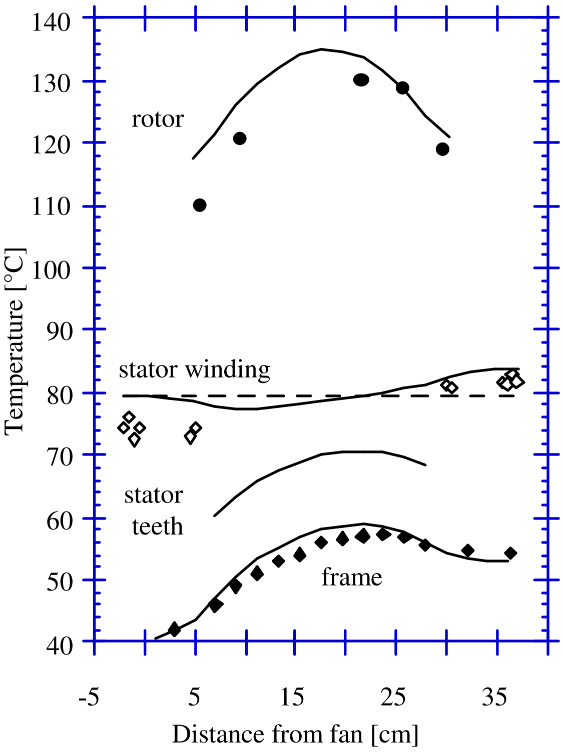

*Figure 85. Temperatures of the 15 kW motor at 88.7 Hz, 94 Nm.*

## 6.4 A small thermal model with simple implementation

The thermal model described so far is the logical choice of model for design purposes. For machine utilizers who want to simulate the temperature with less preparations, a simpler model has been designed, see Fig. 86. This model neglects the variation of the heat transfer coefficient along the frame, so that the machine temperatures will be symmetrical along the axial direction. The asymmetrical temperature distribution that occurs in reality can be taken into consideration by empirical correction factors.

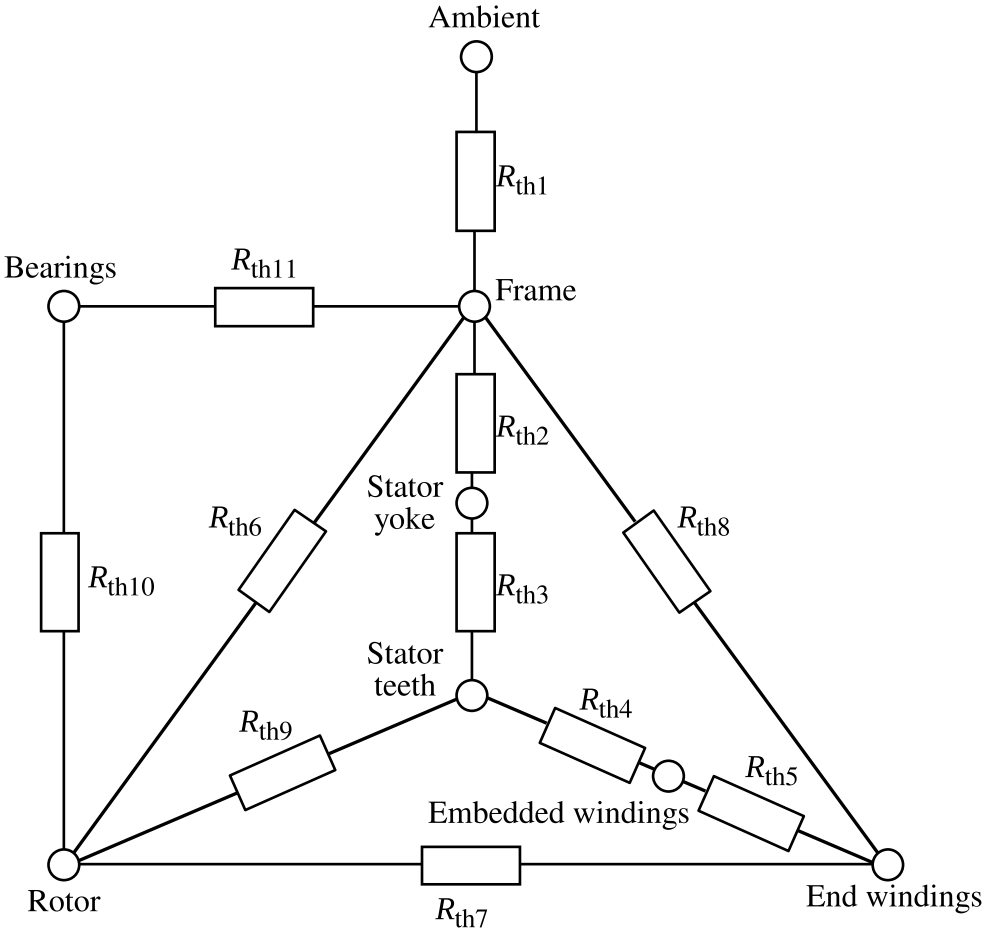
Ambient
$R_{\mathrm{th}1}$
Bearings
$R_{\mathrm{th}11}$
Frame
$R_{\mathrm{th}2}$
Stator yoke
$R_{\mathrm{th}6}$
$R_{\mathrm{th}8}$
$R_{\mathrm{th}10}$
$R_{\mathrm{th}3}$
Stator teeth
$R_{\mathrm{th}4}$
$R_{\mathrm{th}9}$
$R_{\mathrm{th}5}$
Embedded windings
Rotor
$R_{\mathrm{th}7}$
End windings

*Figure 86. A simple thermal model for machines with cage rotors.*

The model is similar to the model proposed by Champenois et al. [39], although they excluded the bearings in their model. It is also similar to the model used by Mellor et al. [1], except that it does not contain two-node configurations. Since the model should be a simple one, it is probably not motivated to use two-node configurations, since the gain in accuracy is rather small. The rotor is lumped into one element, which corresponds to the average rotor surface temperature. The temperature of the shaft is not really interesting to know, so it is only represented as a part of the thermal resistance between the rotor and the bearings. The internal air is not represented, because a Y-Δ transformation can be made that eliminates this node. It is recommended to determine $R_{\mathrm{th1}}$ and $R_{\mathrm{th4}}$ from measurements, and to use the manufacturer's data to calculate all the other thermal resistances. The recommendations are given with some restrictions: The stator windings must be impregnated by the same technique as the test motors (not vacuum-impregnated), and the dimensions must not greatly differ from those of the test motors.

$R_{\mathrm{th1}}$ depends above all on the fan and frame design. It can be calculated from the fan and frame design [33], but the calculations are complex and not necessarily accurate (the fan, for instance, must have a certain geometry for the equations to hold). It is therefore advisable to measure $R_{\mathrm{th1}}$. If this is impossible, it is best to assume a typical rated temperature rise of the frame, e.g. 45 K, and choose $R_{\mathrm{th1}}$ accordingly. If the measured average temperature rise $\theta_{\mathrm{f}}$ of the frame and the total losses $P_{\mathrm{tot}}$ are known, $R_{\mathrm{th1}}$ is given by

$$R_{\mathrm{th\,1}} = \frac{\theta_{\mathrm{f}}}{P_{\mathrm{tot}}} \tag{79}$$

The speed dependence of $R_{\mathrm{th1}}$ is given by

$$R_{\mathrm{th\,1}} = \frac{1}{c_1 + c_2 \omega^{0.8}} \tag{80}$$

where $c_1$ accounts for natural convection and radiation. $c_1$ can be identified by performing a locked rotor test, during which the input power and average frame temperature rise are measured. When $c_1$ is known, $c_2$ can be identified from a no-load test in the same way as explained above.

$R_{\mathrm{th2}}$ is half the value given by Eq. (66) with $\ell=\ell_{\mathrm{Fe}}$, where $\ell_{\mathrm{Fe}}$ is the stator core length. However, if the frame is shrink-fitted, there is a thermal contact resistance between the frame and the stator yoke, which can be identified as explained in detail in Section 5.5.3. The identified value is added to $R_{\mathrm{th2}}$.

$R_{\mathrm{th3}}$ is half the sum of the values given by Eq. (66) and Eq. (68), with $\ell=\ell_{\mathrm{Fe}}$.

$R_{\mathrm{th4}}$ can be calculated using Eq. (61) with $\ell=\ell_{\mathrm{Fe}}$, $d_{\mathrm{a}}$=0.17–0.30 mm (see Section

5.3.1) and $\lambda_a$=0.03. If some of the material data are unknown, the data of the test machines can be used (Appendix B). If the average stator winding temperature can be measured at rated load, it is advisable to modify $R_{th4}$ so that the calculated average stator winding temperature exactly matches the measured one.

$R_{th5}$ is the value given by Eq. (52) with $\ell = \frac{\ell_{av}}{12}$, where $\ell_{av}$ is the average conductor length of half a turn.

$R_{th6}$, $R_{th7}$ and $R_{th8}$ are treated next. In the simplified thermal network, there is no node representing the internal air. This node has been eliminated using a Y-Δ transformation as shown in Fig. 87.

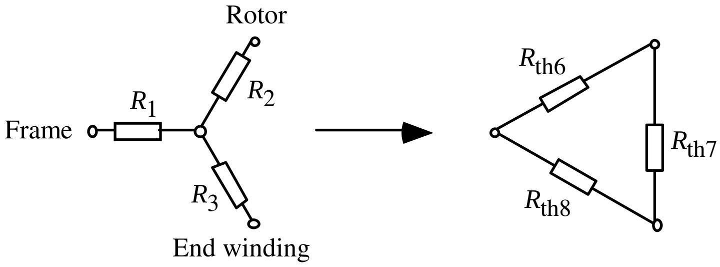

*Figure 87. Y-Δ transformation to eliminate one node*

Some empirical relations for the heat transfer coefficients associated with $R_1$, $R_2$ and $R_3$ have been identified. For $R_1$, Eq. (75) can be used and the area should be the sum of the internal end shield area and the internal frame area. For $R_2$ and $R_3$, see Eqs (48) and (65), respectively. The resulting thermal resistances must be divided by two since the heat paths at the drive side and the fan side are in parallel.

$R_{th9}$ is calculated by using Eqs (44) and (46) with $\ell=\ell_{Fe}$, and adding half the value of the stator teeth thermal resistance given by Eq. (68). For simplicity, radiation can be neglected. $Nu$=2 can be used for $Ta_{(m)}<1740$ and Eq. (43) for $Ta_{(m)}>1740$. Values for $\nu$ and $\lambda_f$ are found in Appendix B.

$R_{th10}$ consists of four parts that should be added together. The first part is the thermal resistance of the rotor yoke. Use Eq. (41) with $\ell=\ell_{Fe}$ to get this value. The second part is the thermal contact resistance between the rotor core and the shaft. Since this value depends on the contact pressure, it may be difficult to evaluate. In that case, use the same value as given by Eq. (41). The third part is the thermal resistance through the shaft. Use half the value given by Eq. (50)

with $\ell$ equal to the distance between the rotor centre and the bearings. The fourth part is equal to $R_{\mathrm{th}11}$.

$R_{\mathrm{th}11}$ is 25 % of the value given by Eq. (78), since one node models both bearings.

Some results from calculations with the simple model are shown in Table 4. Using the loss data of Tables 1–2, $R_{\mathrm{th}1}$ was chosen so that the frame temperature exactly matched the measured average frame temperature of the load cases. $R_{\mathrm{th}4}$ was derived from the already identified values of the large thermal model (see Section 5.3.1). The temperatures can be compared to the corresponding results of the large thermal model in Figs 77 and 83. It can be seen that the coil sides of the 4 kW motor are slightly cooler using the simple model. This is caused by neglecting the axial temperature variations of the frame. On the other hand, the use of single-node configurations for the stator teeth causes a 1–2 °C positive error.

*Table 4. Results for the simple model: (a) Temperatures of the 4 kW motor at 48.8 Hz, 26.7 Nm, (b) Temperatures of the 15 kW motor at 47.9 Hz, 148 Nm.*

| | Frame [°C] | Stator yoke [°C] | Stator teeth [°C] | Coil sides [°C] | End windings [°C] | Rotor [°C] | Bearings [°C] |
|---|---|---|---|---|---|---|---|
| (a): 4 kW motor | 61.6 | 64.3 | 72.6 | 94.2 | 101.4 | 119.0 | 72.2 |
| (b): 15 kW motor | 69.8 | 74.4 | 85.9 | 109.9 | 116.3 | 166.2 | 81.0 |

# 7 Time-dependent problems

The thermal network can be extended to enable transient solutions. A thermal capacity $C_i$ is then added between each node and the ambient. The resulting system of equations is

$$C_i \frac{\partial \theta_i}{\partial t} = P_i - \frac{\theta_i}{R_{i,i}} - \sum_{j=1}^{n} \frac{\theta_i - \theta_j}{R_{i,j}} \qquad i = 1, \ldots, n \tag{81}$$

By defining a thermal capacity matrix

$$\mathbf{C} = \begin{bmatrix} C_1 & 0 & 0 & \cdots & 0 \\ 0 & C_2 & 0 & \cdots & 0 \\ 0 & 0 & C_3 & \cdots & 0 \\ \ldots & \ldots & \ldots & \ldots & \ldots \\ 0 & 0 & 0 & \cdots & C_n \end{bmatrix} \tag{82}$$

the following matrix equation results:

$$\mathbf{C} \frac{\partial \mathbf{\Theta}}{\partial t} = \mathbf{P} - \mathbf{G\Theta} \tag{83}$$

Usually, Eq. (83) is used for transient solutions. In this work, however, the ambient temperature is not assumed to be constant, and Eq. (83) can not be used. There are many cases where the ambient temperature varies in a broad range, for instance outdoor sites. An example is a wind turbine generator where the ambient temperature depends on the outdoor temperature, the air velocity, the solar radiation and the load. To get a transient solution when the ambient temperature varies, a temperature vector

$$\mathbf{T} = \begin{bmatrix} T_1 \\ T_2 \\ T_3 \\ \ldots \\ T_n \end{bmatrix} \tag{84}$$

must be used instead of the temperature-rise vector $\mathbf{\Theta}$. By letting one of the nodes represent the ambient temperature, and by updating this temperature during the simulation, a transient solution is obtained. The resulting system of equations is

$$C_i \frac{\partial T_i}{\partial t} = P_i - \sum_{j=1}^{n} \frac{T_i - T_j}{R_{i,j}} \qquad i = 1,\ldots,n \tag{85}$$

In a matrix form we then have

$$\mathbf{C}\frac{\partial \mathbf{T}}{\partial t} = \mathbf{P} - \mathbf{G}\mathbf{T} \tag{86}$$

Apart from ambient temperature, also frequency, voltage and torque are inputs that are updated during the simulation. Consequently (and also due to their temperature dependence) **G** and **P** must be recalculated at regular intervals.

## 7.1 Thermal capacity

The thermal capacity of an element is calculated by

$$C_{\mathrm{th}} = \sum_{i=1}^{n} m_i c_i \tag{87}$$

where $m$ is the mass, $c$ the heat capacitivity and index $i$ signifies different materials in the element. $C_{\mathrm{th}}$ is generally easy to calculate from the geometry and material data of a machine. However, the calculations of some $C_{\mathrm{th}}$ deserve a comment. $C_{\mathrm{th}}$ for a stator winding element consists of the thermal capacities of both the copper and the insulation. The weight of the impregnation resin can be calculated from the space factor and insulated area of the slots. It is suggested that the end windings are assumed to have the same cross-sectional area as the coil sides.

Furthermore, the treatment of two-node configurations should be as in Fig. 88; The thermal capacity of the element, $C_{\mathrm{th1}}$, belongs to the node that models the average temperature of the element. A negligibly small thermal capacity, $C_{\mathrm{th2}}$, is connected to the other node. The only reason for this is that the transient solution process used demands all nodes to have a thermal capacity. When using the trapezoidal rule as the integration algorithm, it was also noted that $C_{\mathrm{th2}}$ must be significantly smaller than $C_{\mathrm{th1}}$ to avoid stability problems.

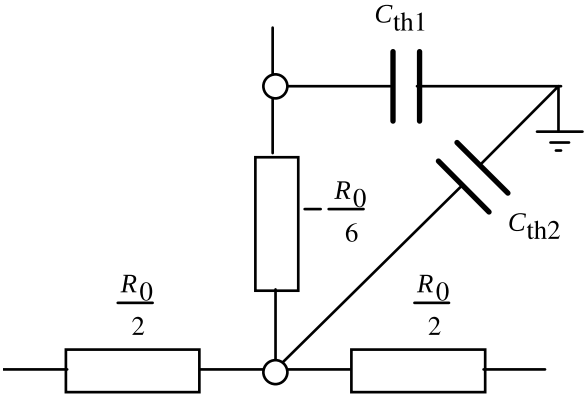

*Figure 88. Thermal capacities in a two-node configuration*

## 7.2 Numerical integration methods

The computer time needed to complete a simulation, and the accuracy of the solution depend on the numerical integration method that is used. Methods reported to have been used before to solve this specific problem include Runge-Kutta methods [6] and variants of implicit methods [7]. The advantage of an implicit method is that it has better stability. This makes it possible to use a time step that equals the updating interval of **P** and **G**. According to tests that were performed for thermal models ranging in size from 10 to 100 nodes, an explicit method like Runge-Kutta is almost always slower than an implicit method mainly because a shorter time step must be used. If there are two-node configurations in the thermal network, an implicit method is strongly recommended. In fact, all of the tested explicit methods failed to converge for two-node configurations because of the negative thermal resistances. Several integration methods were tested for the models and the fastest method was the implicit Adams-Moulton method of 2nd order (also known as the trapezoid rule) which is described by the algorithm

$$\mathbf{T}_{n+1} = \mathbf{T}_n + \frac{h}{2}(\mathrm{f}(t_{n+1}, \mathbf{T}_{n+1}) + \mathrm{f}(t_n, \mathbf{T}_n)) \qquad (88)$$

where $h$ is the time step and f the derivative function $\mathbf{C}^{-1}(\mathbf{P}\text{-}\mathbf{GT})$. The global error was found to be negligible for practical time steps of about 1 minute. Higher order Adams-Moulton methods are not practical, since they are multi-step methods that require **P** and **G** to be constant.

However, in some cases an explicit method might be best, namely when it converges for a time step that equals the chosen indata updating interval. This typically happens for smaller thermal networks or larger machines. In such a case, a 2nd order Runge-Kutta method is a good choice (Euler's forward method is in fact faster but the tests indicate that the error of this method would not be negligible for such a case).

## 7.3 Simulations

Temperature simulations and measurements were made in order to check the validity of the thermal model with 107 nodes. The measurements were performed at 3 points: the frame, the stator end winding and the rotor (the rotor temperature was only measured for the 15 kW motor). The hottest thermocouple on the drive side of the stator end winding was used since that thermocouple probably was closest to the average temperature in a cross-section. The measurements were made by a combined filter/amplifier and a computer with plug-in card. Samples were taken every minute. Three measurements are shown. Figure 89 shows a step response for the 15 kW motor, where the machine is started cold and loaded by rated torque at constant voltage and frequency. Figure 90 shows a similar step response for the 4 kW motor. Figure 91 shows the response of the 15 kW motor to five different load sequences. The voltage/frequency ratio is constant during the first four sequences, but the torque and the frequency are changed as indicated by the figure text. During the last sequence, the machine is switched off and standing still.

The measurements show that the thermal model is capable of calculating the temperatures in the machines with good accuracy for different speeds and loads. However, in the case of the 15 kW motor, a condition for this was that the losses were measured and separated for different operating points. The calculated stator winding temperature is higher than the measured one for the 15 kW motor. This is partly explained by the fact that the empirical equations for some of the thermal resistances were not tailor-made but adapted to fit both the 15 kW and the 4 kW motors. Temperature dependence of the thermal resistance between the stator windings and the stator teeth as well as minor errors in the loss calculations may also have contributed to the error, which is in the order of 4° C. The rotor temperature is also overestimated, but this is probably because the real rotor losses were lower than the calculated ones. The frame temperature of the 4 kW motor appears to be overestimated, but this is rather a result of axial temperature differences; the frame temperature as a whole was in close agreement with the calculated temperatures.

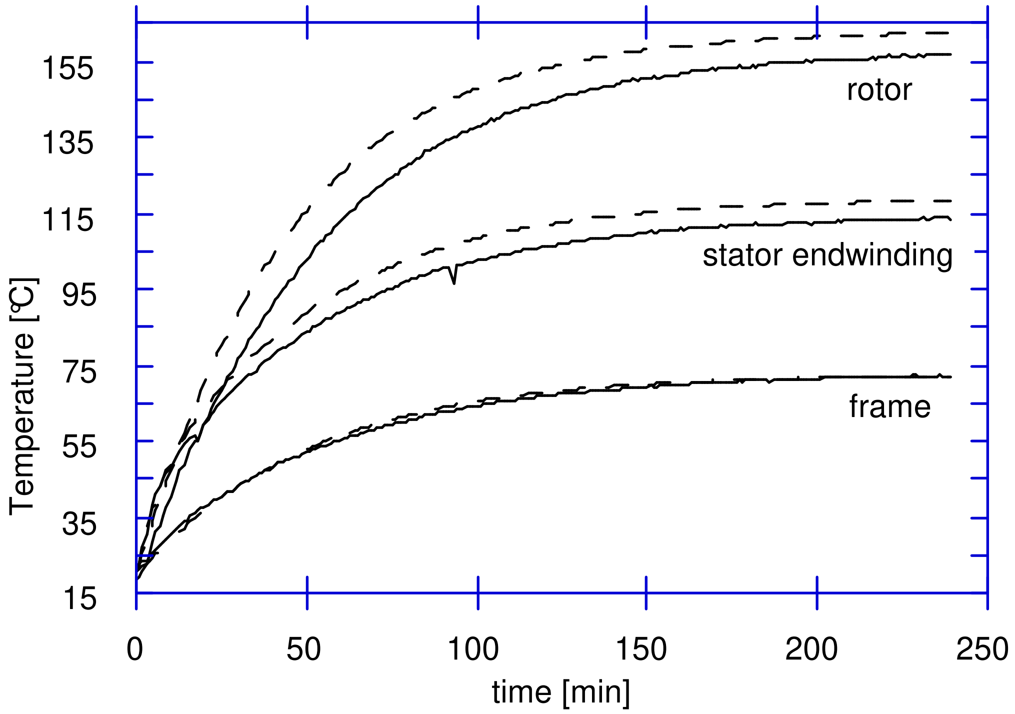

*Figure 89. Measured and simulated temperatures of the 15 kW motor at approximately rated conditions. Solid lines are measured and dashed lines are simulated.*

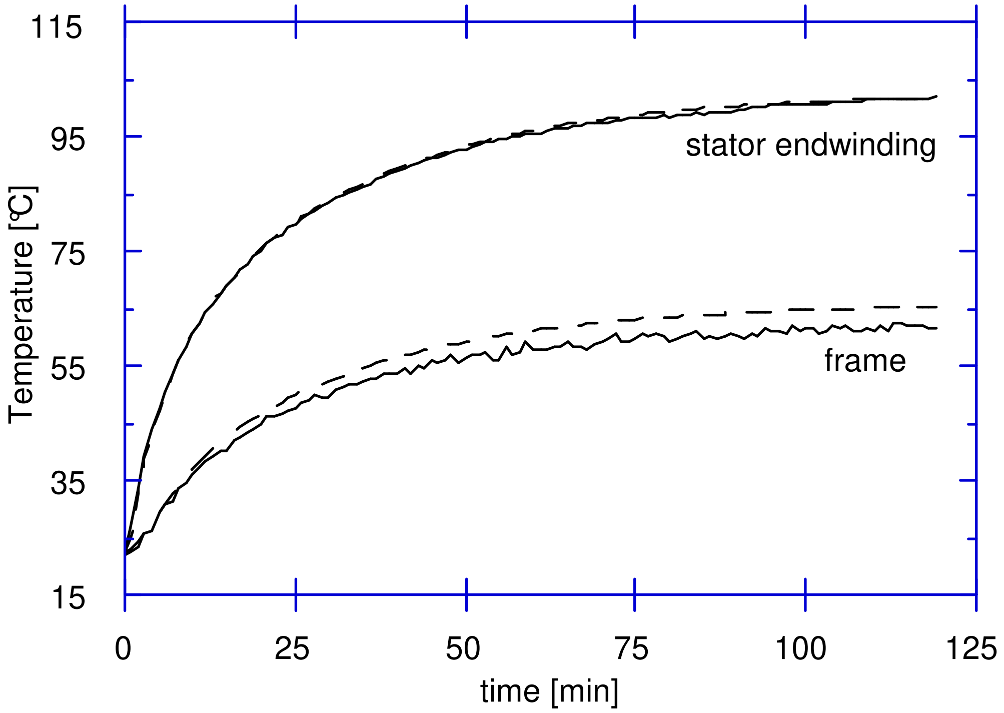

*Figure 90. Measured and simulated temperatures of the 4 kW motor at approximately rated conditions. Solid lines are measured and dashed lines are simulated.*

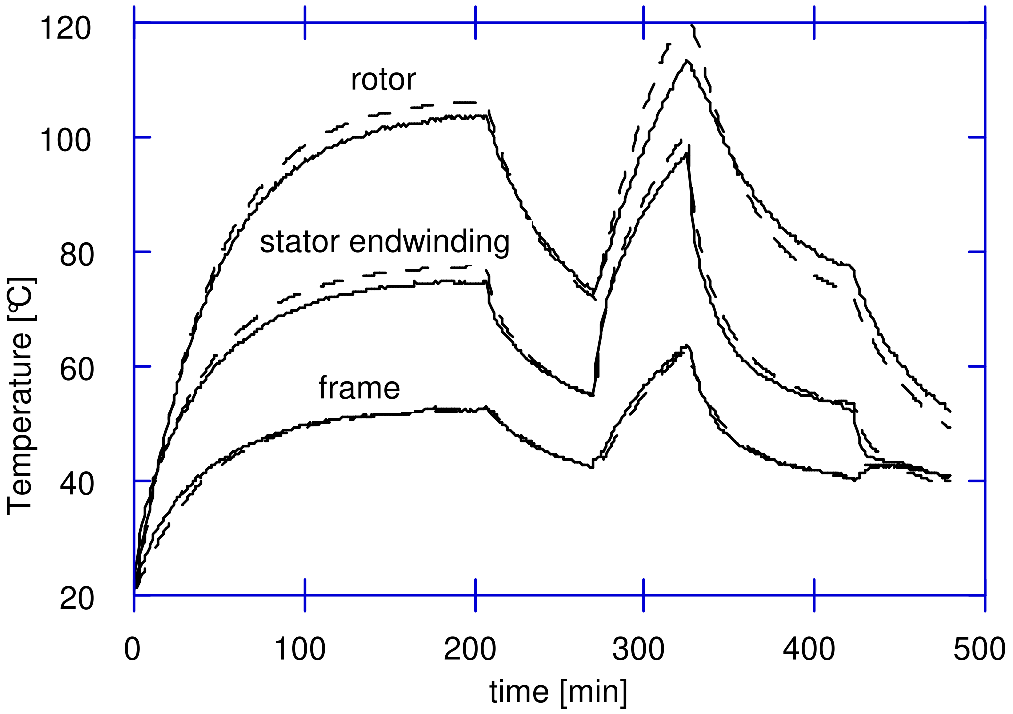

*Figure 91. Measured and simulated temperatures of the 15 kW motor at changing conditions. The operating conditions are approximately: 2/3 rated load at 50 Hz for t=0–205 min; no load at 50 Hz for t=205–270 min.; rated load at 30 Hz for t=270–320 min.; no load at 70 Hz for t=320–420 min.; switched off after t=420 min. Solid lines are measured and dashed lines are simulated.*

## 7.4 Wind energy applications

A possible application of the thermal models is to determine the loadability of wind turbine generators, which usually are TEFC induction machines. Due to the fact that the turbine and the gear-box usually are dimensioned for large overloads, it may be profitable to utilize the generator close to its thermal limit, even if this means exceeding the rated load. Simulations [10] showed that the 15 kW motor can be overloaded by 20 % continuously at room temperature without exceeding the thermal limit of the winding insulation. A thermal model can be used in the process of determining a control algorithm for the wind turbine, by giving information about the response to changes in load, speed and ambient temperature. However, the control system must probably rely on feedback from measured stator winding temperatures, since there are too many error sources in a purely theoretical model. The most important questions are then whether the measured stator winding temperatures are reliable and what the relation is between the measured temperatures and the actual hot-spot temperature of the winding.

From the experiences of the 15 kW motor, it seems like temperature sensors that are attached by a good thermal contact to the surface of the end windings can be expected to be 5–10° C colder than the average temperature in a cross-section of the end winding (see Fig. 49). This difference is likely to be proportional to the temperature rise of the stator windings. It is suggested that the hot-spot temperature in a cross-section of the end windings can be approximately calculated from the average temperature by Eq. (58). It can probably be assumed that the drive side end winding is the hottest part of the winding. However, the axial temperature differences can be more carefully analysed using the thermal network of Fig. 28.

Some other aspects that should be investigated before beginning to overload an electric machine are the bearing temperature and the effect of thermal expansion of the rotor.

# 8 Conclusions

The general goal of the work was to design a suitable thermal model that can be used as a tool for constructing cage induction motors, and to describe the related problems and aspects of implementation. This goal has been achieved by a 107-node thermal network. The related problems, i.e. the loss calculation and the thermal resistance calculation have been subject to a detailed examination. The method of implementation and the results have been presented.

A particular goal was to investigate the method and level of discretization of the machine. Concerning the level of discretization, the conclusion is that it is not necessary to use a large number of nodes for the sake of accuracy, but it is nevertheless better than a small number of nodes because it gives more detailed temperature information. Regarding the method of discretization, i.e. how the machine parts are lumped and what kind of node-configurations should be used, the conclusion is that one-node configurations can be used for all elements except the stator teeth, which should be modelled by two-node configurations. The lumping of the elements are determined by temperature differences and geometry considerations: volumes having small temperature differences are lumped together naturally, because boundaries between volumes of different temperature are geometrically fairly well defined in a machine.

Another important goal was to establish methods to identify unknown thermal resistances, since there does not seem to exist any recommendations on how such measurements should be performed. It would of course be best to make a direct measurement of the unknown thermal resistances, but unfortunately this would necessitate the making of complicated dummies. This goal has instead been achieved by the use of identification models. These models require a fairly high accuracy of the temperature and loss measurements. The results for the two test motors have been used to form some empirical relations that can be used for other machines if they do not differ too much in shape or size.

The thermal resistance between the stator winding and the stator teeth has been identified using an identification model. It can also be calculated using a rectangular slot approximation with a surrounding equivalent air pocket. The winding itself is assumed to be completely free from air pockets. From the identification model, a value of 0.17–0.30 mm of the thickness of the equivalent air pocket has been derived. The thickness is likely to be larger for larger machines and depends on the method of applying the impregnation (vacuum-impregated machines are likely to have smaller air pockets). The thermal resistance between the stator winding and the stator teeth decreases slightly with temperature. The temperature dependence has not been completely analysed, so it is worthwhile to make a follow-up investigation.

The heat transfer coefficients of the end windings and other parts inside the end regions of the machine can be related to the peripheral speed of the rotor. The heat transfer coefficient between the rotor ends and the internal air was identified as a function of the rotor peripheral speed. The heat transfer coefficient between the stator end windings and the internal air could be determined approximately. Although the results are rather scattered, a 0.6 power-of-speed relation is suggested. However, a sensitivity analysis has shown that the stator winding temperature is more sensitive to the heat transfer coefficients of the end shields than that of the end windings, because they determine to a greater extent the temperature of the internal air. Thus, it is important to know the heat transfer coefficients of the end shields. Empirical relations are given for the internal and external heat transfer coefficients of the end shields, that probably are rather crude, but nevertheless better than to neglect their influence.

When it comes to the modelling of the frame, the heat transfer coefficient must be measured; it is not easy to calculate it from geometry data. This measurement should not be a problem for a manufacturer who only uses a few standard frame and fan arrangements. Entrance effects and reduction of cooling air velocity along the frame can be modelled by assuming that the local heat transfer coefficient decreases exponentially towards a constant value along the frame. The speed dependence can be modelled as a constant plus a 0.8 power-of-speed term.

The bearings can be modelled by lumping together the inner and the outer race with parts of the shaft and the end shield, respectively. The balls form a separate node. The thermal resistance of a bearing decreases with increasing speed; an empirical relation is suggested.

A secondary result of the study is the development of a small thermal network, which may be more convenient for users of a specific machine who want to investigate its loadability. It is suggested in detail how its thermal resistances should be calculated or measured.

It is shown that additional losses and no-load stray losses can be important error sources in the thermal calculations. A finite element method can be used to calculate those losses in the stator, but the rotor losses are difficult to calculate accurately, especially if the rotor bars are skewed. The fundamental rotor and stator winding losses can be expected to be sufficiently accurately calculated by using the equivalent circuit of the induction machine. The friction and windage losses are usually too small to have a large influence on the machine temperatures.

# References

1 Mellor, P.H., Roberts, D., Turner, D.R., "Lumped parameter thermal model for electrical machines of TEFC design". *IEE Proceedings-B*, 138 (1991) 5, p. 205-218.

2 Chillet, C.,Hadi, A.W., Perret, R., Isnard, R., "Identification du modèle thermique d'une machine à induction de puissance moyenne". *Revue de Physique Appliquée* 24 (1989) 9, p. 923-931.

3 Armor, A.F., Chari, M.V.K., "Heat flows in the stator core of large turbine-generators by the method of three-dimensional finite elements". *IEEE Transactions on Power Apparatus and Systems* 95 (1976).

4 Armor, A.F., "Transient, three-dimensional, finite element analysis of heat flow in turbine-generators". *IEEE Transactions on Power Apparatus and Systems* 99 (1980) 3, p. 934-946.

5 Perez, I.J., Kassakian J.G., "A stationary thermal model for smooth air gap rotating electrical machines". *Electric Machines and Electromechanics* 3 (1979) 3, p. 285-303.

6 Eltom, A.H., "Motor temperature estimation incorporating dynamic rotor impedance". *IEEE Transactions on Energy Conversion* 6 (1991) 1, p. 107-113.

7 Lutz, K., Thum, E., "Erweiterte Wärmequellennetze zur Berechnung instationärer Vorgänge". *etzArchiv* 9 (1987) 6, p.199-201.

8 Kotnik, R.L., "An equivalent thermal circuit for nonventilated induction motors". *AIEE Transactions Pt 3A,* 73 (1954), p.1604-1609.

9 Bass, J., "Electrical resistivity of pure metals and dilute alloys". In: Landolt-Börnstein New Series, *Metals: Electronic transport phenomena*, vol 15 a. Berlin: Springer-Verlag, 1982, p. 1-7.

10 Kylander, G., "Modellering och mätning av temperatur och förluster i mindre asynkronmaskiner". Göteborg, Sweden: Chalmers University of Technology, Department of Electrical Machines and Power Electronics, Technical Report No 147L, 1993. 106 p.

11 International Electrotechnical Commission, "Methods for determining losses and efficiency of rotating electrical machinery from tests (excluding machines for traction vehicles)", Publication 34-2, 3:rd ed.
Genève: Bureau Central de la Commission Electrotechnique Internationale, 1972.

12 Alger, P.L., Angst, G., Davies, E.J., "Stray load losses in polyphase induction machines". *AIEE Transactions Pt 3A*, 78 (1959), p. 349-357.

13 Alger, P.L., "Induced high-frequency currents in induction machines". *AIEE Transactions Pt 3*, 76 (1958), p. 724-729.

14 Arkkio, A., "Analysis of induction motors based on the numerical solution of the magnetic field and circuit equations". Helsinki, Finland: Helsinki University of Technology, Laboratory of Electromechanics, Acta Polytechnica Scandinavica, Electrical Engineering Series No. 59, 1987.

15 Arkkio, A., Niemenmaa, A., "Estimation of losses in cage induction motors using finite element techniques". *International Conference on Electrical Machines*, Manchester, U.K., 15-17 September 1992.

16 Cristofides, N., "Origins of load losses in induction motors with cast aluminium rotors". *Proceedings of the IEE* 112 (1965) 12, p. 2317-2332.

17 Oberretl, K., "13 Regeln für minimale Zusatzverluste in Induktionsmotoren". *Bulletin Oerlikon* 389/390 (1969) , p. 1-11.

18 Odok, A., "Stray load losses and stray torques in induction machines". *AIEE Transactions Pt 3* 77 (1958), p. 43-53.

19 Cristofides, N., Adkins, B., "Determination of load losses and torques in squirrel cage induction motors". *Proceedings of the IEE Pt B* 113 (1966) 12, p. 1995-2005.

20 Nee, H., "Frekvensstyrda asynkronmotorer med växelriktare för hög kopplingsfrekvens". Stockholm, Sweden: KTH, Department of Electrical Machines and Power Electronics, Trita-EMK 91-01, 1991. 118 p.

21 Richter, R., *Elektrische Maschinen.*, vol. 1, 2:nd ed. Basel: Birkhauser Verlag, 1951.

22 SKF Huvudkatalog, Katalog 2800S, 1970.

23 Rawcliffe, G.H., Menon, A.M., "A simple new test for harmonic- frequency losses in A.C. machines". *Proceedings of the IEE Pt 2* 99 (1952) p. 145-150.

24 Cummings, P.G., "Estimating effect of system harmonics on losses and temperature rise of squirrel-cage motors". *IEEE 32nd Annual Petroleum and Chemical Industry Conference*, Houston, TX, 9-11 September 1985, p. 1751-1755.

25 Schuisky, W., *Induktionsmaschinen*. Wien: Springer Verlag, 1957.

26 Holman, J.P., *Heat transfer*. 7th ed. New York: McGraw-Hill, 1992.

27 Soderberg, C.R., "Steady flow of heat in large turbine-generators". *Transactions of the AIEE* 50 (1931), p. 782-802.

28 Widek, P., "Auxiliary powered induction machines with inverter supply". Göteborg, Sweden: Chalmers University of Technology, Department of Electrical Machines and Power Electronics, Report R-90-08, 1990. 38 p.

29 Becker, K.M., Kaye J., "Measurements of diabatic flow in an annulus with an inner rotating cylinder". *Journal of Heat Transfer* 84 (1962), p. 97- 105.

30 Gazley C., "Heat transfer characteristics of rotational and axial flow between concentric cylinders". *Transactions of the ASME* 80 (1958) 1, p. 79-90.

31 Aoki, H., Nohira, H., Arai, H., "Convective heat transfer in an annulus with an inner rotating cylinder". *Bulletin of JSME* 10 (1967) 39, p. 523-532.

32 Bjorklund, I.S., Kays, W.M., "Heat transfer between concentric rotating cylinders". *Journal of Heat Transfer* 81 (1959), p. 175-186.

33 Kotrba, V., "Cooling and ventilation of an electrical machine". Helsinki, Finland: Helsinki University of Technology, Laboratory of Electromechanics, Lecture Notes, 1993. 70 p.

34 Etemad, G.A., "Free-convection heat transfer from a rotating horisontal cylinder to ambient air with interferometric study of flow". *Transactions of the ASME* 77 (1955), p. 1283-1289.

35 Luke, G.E., "The cooling of electric machines". *Transactions of the AIEE* 42 (1923), p. 636-652.

36 Koziej, E., "Cooling and heating of electrical machines". Helsinki, Finland: Helsinki University of Technology, Laboratory of Electromechanics, Lecture Notes, 1989. 104 p.

37 Incropera, F.P., DeWitt, D.P., *Fundamentals of heat and mass transfer*. 3rd ed. New York: John Wiley and Sons.

38 Mills, A.F., "Experimental investigation of turbulent heat transfer in the entrance region of a cirular conduit". *Journal of Mechanical Engineering and Science* 4 (1962) 1, p. 63-77.

39 Champenois, G., Roye, D., Zhu, D.S.,"Electrical and thermal performance predictions in inverter fed squirrel-cage induction motor drives". *Electric Machines and Power Systems* 22 (1994) 3, p. 355-370.

# Appendix

## A Data of the test motors

The MBT180L is a 6-pole motor with 36 stator slots and 39 rotor slots. The electrical steel used for the rotor and stator cores is 0.5 mm SURA DK70, which contains 1 % Si. The temperature class of the stator winding is F (155° C). The rotor cage winding is skewed one stator slot pitch (herring-bone skew). The MBT112M is a 4-pole motor with 36 stator slots and 28 rotor slots. The electrical steel is 0.65 mm SURA DK70. The temperature class and the skew are the same as for the MBT180L. Geometrical data are given in Tables A.1–A.2 and the parameters of the equivalent circuit are given in Table A.3

*Table A.1. Geometry data.*

| | MBT180L | MBT112M |
|---|---|---|
| stator outer diameter | 291.2 mm | 187.2 mm |
| stator inner diameter | 190.2 mm | 115 mm |
| core length | 230.0 mm | 105 mm |
| air gap | 0.45 mm | 0.35 mm |
| equivalent air gap | 0.61 mm | 0.45 mm |
| rotor inner diameter | 55 mm | 38 mm |
| stator slot area | 185 mm$^2$ | 96 mm$^2$ |
| rotor slot area | 76.2 mm$^2$ | 68.5 mm$^2$ |
| end ring height, length | 24 mm, 18 mm | 17 mm, 9.5 mm |
| rotor fin height, length | 23 mm, 30 mm | 15 mm, 13 mm |
| average frame thickness (adjacent to core) | 4.2 mm | 3.9 mm |
| frame thickness before and after the core | 9 mm | 6 mm |
| length of the frame (excluding end shields) | 370 mm | 175 mm |
| bearing average diameter | 77.5 mm | 46 mm |
| frame area including fins and end shields | 1.35 m$^2$ | 0.37 m$^2$ |
| drive end shield exterior area | 0.12 m$^2$ | 0.04 m$^2$ |
| drive end shield interior area | 0.12 m$^2$ | 0.04 m$^2$ |
| fan end shield exterior area | 0.12 m$^2$ | 0.069 m$^2$ |
| fan end shield interior area | 0.12 m$^2$ | 0.034 m$^2$ |
| fan diameter | 280 mm | 170 mm |

*Table A.2. Stator winding data.*

| | MBT180L | MBT112M |
|---|---|---|
| average length of half a turn | 415 mm | 260 mm |
| average length of the overhangs | 185 mm | 155 mm |
| copper area in a slot | 72.3 $mm^2$ | 38.4 $mm^2$ |
| insulated slot area | 146 $mm^2$ | 71 $mm^2$ |
| slot insulation thickness | about 0.4 mm | about 0.4 mm |

*Table A.3. Parameters of the equivalent circuit for the test machines (at 20° C).*

| | MBT180L | MBT112M |
|---|---|---|
| stator resistance | 0.18 Ω/phase | 1.26 Ω/phase |
| stator leakage reactance | 0.8 Ω/phase | 2.46 Ω/phase |
| rotor resistance | 0.19 Ω/phase | 0.97 Ω/phase |
| rotor leakage reactance | 0.65 Ω/phase | 2.44 Ω/phase |
| magnetizing reactance | 12.6 Ω/phase | 53.2 Ω/phase |

# B Material data

The material data that was used to calculate the thermal resistances of the test machines were taken from Swedish standards and international handbooks. In Table B.1, the properties of the materials in the test motors are given. In those cases where the temperature dependence is not negligible, the temperature coefficient at 0° C is given.

*Table B.1. Material data.*

| Material | Used in | Heat capacitivity [J/kg·K] | Density [kg/m$^3$] | Heat conductivity [W/m·K] |
|---|---|---|---|---|
| Cu 99.90 | stator winding | 385 | 8900 | 395 |
| Al 99.5 | rotor cage | 900 | 2705 | 234 |
| Al - Si 12 | frame | 960 | 2650 | 150 |
| Steel SS1550 | shaft | 460 | 7800 | 51 |
| Unsaturated polyester | stator winding impregnation | 1700 | 1350 | 0.2 |
| SURA DK-70 (1 % Si) | stator and rotor core | 460 | 7800 | 38 |
| air | air gap<br>internal air<br>ambient air | 1010 | 1.23 at 0°C temperature coefficient - 0.00278 K$^{-1}$ | 0.0243 at 0°C temperature coefficient 69.4·10$^{-6}$ K$^{-1}$ |

The kinematic viscosity of air is $\nu = 130.92 \cdot 10^{-7}$ m$^2$/s at 0°C and has the temperature coefficient $1.08 \cdot 10^{-7}$ K$^{-1}$. The Prandtl number of air is Pr=0.71 in the relevant temperature range. The volume coefficient of expansion of air is $\beta = 1/T$, where $T$ is the absolute temperature of the air.